FREE PLAY STUDY USING PETERS UNSTEADY AERODYNAMICS WITH APPLICATIONS TO PROBABILISTIC MODELING

By

JEET PANCHAL

A thesis submitted to the

School of Graduate Studies

Rutgers, The State University of New Jersey

In partial fulfillment of the requirements

For the degree of

Master of Science

Graduate Program in Mechanical and Aerospace Engineering

Written under the direction of

Haym Benaroya

And approved by

_____

_____

_____

New Brunswick, New Jersey

May 2020

ABSTRACT OF THE THESIS

FREE PLAY STUDY USING PETERS UNSTEADY AERODYNAMICS WITH APPLICATIONS TO PROBABILISTIC MODELING

by JEET PANCHAL

Thesis Director:
Haym Benaroya

In the last two decades, there has been an increasing interest in the field of nonlinear aeroelasticity. With substantial improvements in computing capabilities, the control surface free play problem is now being reinvestigated by many researchers with the goal of developing more advanced and accurate analytical models. Despite this field of research being well defined, numerous modeling approaches exist, yielding unique numerical predictions of the aeroelastic dynamical behavior and its associated properties. The literature shows many variabilities in the parameters that define free play, with the majority of the existing models being developed deterministically. In this thesis, different nonlinear aeroelastic systems with finite-state unsteady aerodynamics are investigated in the time domain. The results are then used to create a novel probabilistic framework to predict the likelihood of encountering aeroelastic instabilities.

ACKNOWLEDGEMENTS

I would like to thank my adviser, Professor Haym Benaroya, for his unwavering support to me and my family during my graduate studies. He has provided me with fantastic opportunities to grow and succeed in our time working together. His guidance has been pivotal in my growth both academically and personally, often providing advice that transcends academics and career. As I have gone through the many meanders in the river of life, he has been there to ensure that I have always steered my way back into the fast currents to advance further and not get stuck. For him, I am always grateful and happy to have as a mentor and friend. We still have much more exciting work to accomplish together in our future.

Many thanks to my committee members, Professor Edward Demauro and Professor Haim Baruh. Both were helpful during different moments of my research, providing great insight when I sought out additional help. Additionally, I wish to thank Professors Dewey Hodges, from Georgia Institute of Technology, and Professor David Peters, from Washington University in St. Louis. Both were friendly and supportive in helping me better understand some technical theories in aeroelasticity when I reached out to them with questions.

Among other people, I appreciate my family for giving me the space I needed in life to grow. I am also thankful for all of the friends I have gained in my time at Rutgers thus far. Thank you especially to Qiming Guan for being the best office-mate I can ask for. Lastly, but not least, thanks to my wonderful life partner, Justine Quow, and my cat, Sammie. Justine has been by my side from the beginning of my graduate school journey and continues to motivate me in all aspects of my life. Finally, many thanks to my cat, Sammie, for being a great emotional support as I completed this thesis. She would curl up by my side and fall asleep near my laptop as I spent many late nights and early mornings typing the last chapters of my thesis.

Contents

Chapter 1

Introduction

1.1 Background

Free play in aircraft control surfaces, all-moving wings, and external stores is a structural nonlinearity that is defined by reduced or zero stiffness within certain ranges of motion of the actuating structures. Free play results from degraded parts, such as worn hinges or loose attachments, often due to an aging aircraft. There are various mathematical representations for this phenomena, many of which are explained in detail in Section 2.2. Shown in Figure 1.1 is the idealization of freeplay, which is often represented by a piecewise linear function with zero stiffness in the region of freeplay.

Excessive free play is detrimental to the safety of aircraft. It can lead to catastrophic aeroelastic instabilities such as limit cycle oscillations, which accelerate the accumulation of structural fatigue damage and compromise controllability. Furthermore, it has been well-documented that such instabilities occur below the predicted linear flutter velocities, rendering potentially hazardous flight scenarios such as premature flutter or limit cycle oscillations [1, 2].

The Federal Aviation Administration (FAA) has established guidelines that define allowable free play quantities, limitations, and considerations that would meet

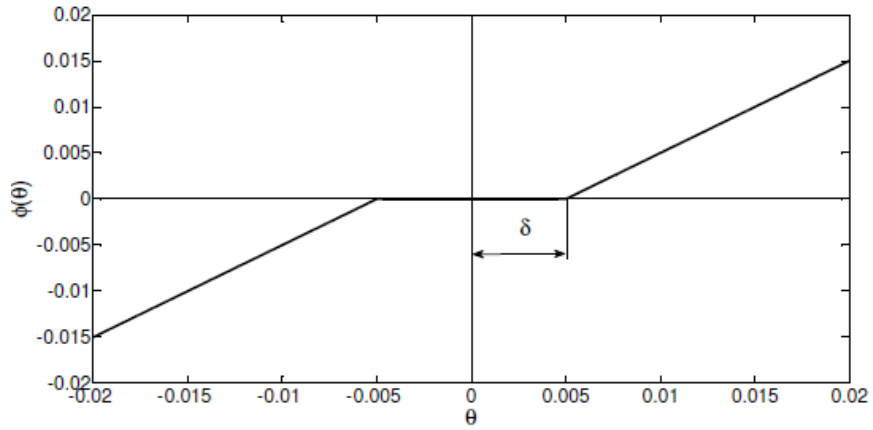

Figure 1.1: The graph shows the degrees of rotation (in radians) of a control surface, denoted in the x-axis, and the corresponding hinge moment necessary to rotate control surface, denoted in the ϕ-axis. The free play region is seen in the center where there is a flat spot in the graph about $\pm\delta$, which is the variable for the amount of rotational free play [3].

regulatory compliance to freedom from flutter in their Advisory Circular (AC) 23.629-1B (normal, utility, and acrobatic category airplanes) and 25.629-1B (transport category airplanes) [4, 5]. The recommendations in these guidelines, however, are in some ways antiquated. For example, the current AC 23.629-1B that governs modern design of non-transport category airplanes gives numerical limitations on free play angle based on data from outdated free play experiments done in the 1950s, directly referencing the 1955 Airframe and Equipment Engineering Report No. 45 where the data were published [4, 6]. Not only are such values of free play angle limitations very stringent and resulting in higher manufacturing and maintenance costs, but they also do not completely guarantee permanent removal of aeroelastic instabilities, regardless of how small or large the free play nonlinearity may be [7, 8]. An approach that involves using only the angles of free play as the sole parameter of consideration for establishing freedom from aeroelastic flutter is not suitable for all types of aircraft, especially aircraft that fly in high subsonic and transonic airspeed. AC 25.629-1B is more up to date with its guidance, taking a qualitative approach to addressing free play and providing explicit guidelines to manufacturers of transport category

airplanes for incorporating the effects of free play in important aeroelastic stability calculations. Regardless of the difficulties with developing proper Advisory Circulars, aeroelasticians are well aware of the problems resulting from free play.

Free play related flight challenges have been well known since the earliest designs of the first airplanes. In the 1930s and 1940s, aeroelasticians correctly documented that free play affected aeroelastic flutter. Theodorsen and Garrick [9, 10] stated, "... any slack in the aileron... may cause a mild type of flutter, which should not be permitted for too long a time." While their focus at the time was to simply understand flutter, they noted that such nonlinearities degraded flight stability. Hence, they tried to develop different ways to avoid flutter resulting from free play by trying to completely eliminate it. Examples of such designs included determining a way to maintain constant pre-load or tension in control mechanisms, such as that shown in Figure 1.2. However, as aircraft technology became more complex, more sources of structural nonlinearities were introduced, and eliminating the issues of free play (or backlash) was not always guaranteed, regardless of design [11].

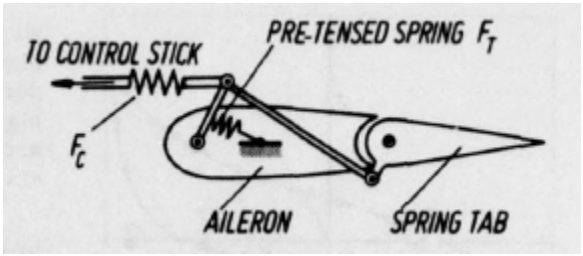

Figure 1.2: Two different springs are used to ensure that the tab has a constant spring tension on it to avoid regions of free play [11].

The earliest work performed to understand and model the effects of free play on the dynamics of aircraft control surfaces was initiated in the 1950s. Around this time, understanding nonlinear aeroelastic behavior became a critical point of interest for the U.S. Air Force. With the emergence of transonic flight, the Air Force's goal was to define margins of acceptable free play in various control surfaces, particularly

examining the effectiveness of tail horizontal stabilizers and elevators where severe aerodynamic reductions were anticipated in the trailing edges [3]. Hoffman and Spielberg [2] carried out some of the first full scale experimental studies in a wind tunnel on unswept all-moving elliptical wing sections with controlled amounts of free play values, over a range of low to high subsonic velocities in free stream air. They tested to find correlations between free play quantities and various characteristics of flutter instabilities. See Figure 1.3. They observed limited amplitude flutter oscillations at speeds below the linear flutter velocities. Supercritical limit cycle oscillation (LCO) behavior was observed, with a gradual increase in amplitude size resulting from proportional increase in free play displacement. These experiments laid the foundation for establishing the free play limits in the Airframe and Equipment Engineering Report No. 45 released by Rosenbaum and Vollmecke [6]. Around the same time in the 1950s, Woolston et al. [12] and Shen [13] initiated some of first analytical studies of the free play problem using analog computers to understand preliminary response of the aeroelastic systems with different types of structural nonlinearities.

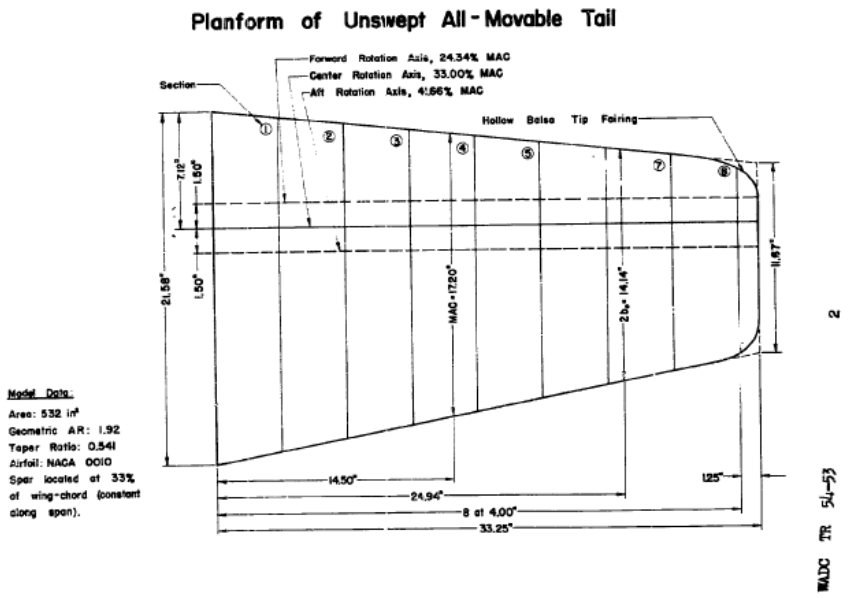

Figure 1.3: The tested wing was split into eight movable sections linked together by a single spar that cuts across the wing perpendicularly, as shown by the dotted lines [2].

These studies laid the foundation for the subsequent research on this topic. Through the late 1980s to the present, research interest in this topic has grown substantially. As more aircraft continue to age and newer more complicated aircraft are designed, concerns with structural nonlinearities have drastically increased. Finding better ways to resolve such issues is important because there is a belief that the current requirements and approaches for monitoring free play and conducting maintenance are very costly [14]. Furthermore, readily accessible large-scale and fast computing capabilities have also led to the rise of research interest in complex domains of nonlinear aeroelasticity within the academic community, as seen by more literature published on free play. While the approach to researching free play is generally well defined, the aviation community has yet to fully understand the global implications of the free play problem. Thus, there is strong motivation for continued research on this topic.

1.2 Thesis Contribution

In this thesis, several of the issues mentioned above will be explored. The goal of this research is to demonstrate the variability in the response of a two degree-of-freedom aeroelastic system with many different nonlinear stiffness models. Our new contributions include using a new finite-state, induced flow unsteady aerodynamics theory for studying free play. We also create a first of its kind 3-D bifurcation diagram that shows how an aeroelastic system's response would evolve with changing free play. Finally, we develop a novel probabilistic framework to help predict the likelihood of encountering aeroelastic instabilities.

In the next chapter, a general literature review of this field of study is provided. Then, the analytical framework is developed in Chapter 3, followed by the results and discussion given in Chapter 4. Lastly, concluding remarks and ideas for future work are given in Chapter 5.

Chapter 2

Literature Review

A majority of the literature on the topic of free play initiate their studies by expanding upon fundamental aeroelastic theories. Dynamical equations of motion are developed for an assumed cross-sectional structural model of a wing or control surface that is subjected to selected aerodynamic loads. Then the free play nonlinearity is introduced into the structural model and various types of engineering analyses are performed to map regions of aeroelastic instability or flutter, and identify parameters of influence and their sensitivities to aeroelastic response. The accuracy of these models is usually assessed by comparing numerical results to data from experimental studies involving similar structural and aerodynamic setups. While many research studies aim to better understand free play related instabilities and their implications for aircraft reliability, some research choose to exploit the instabilities, such as using wing-based piezoelectric systems to harvest energy [15]. Others wish to explore novel means of active control and other suppression techniques to prevent the instabilities resulting from nonlinear aeroservoelastic systems [16, 17]. The field of research is quite large.

2.1 Structural Models

Aeroelastic model formulation for the free play problem starts by initially approximating an aircraft wing in its simplest structural form as a long, thin, and symmetric plate with uniformly distributed mass and structural properties. These models also assume that the plate has uniform transverse and rotational stiffness along its span. The only boundary condition on this plate is that one edge is fixed to a wall, signifying a wing's root attachment to the fuselage body of an aircraft. Due to uniformity and symmetry of such a plate, we are able to completely understand the entire plate's dynamical behavior by only observing a single single cross section known as a "typical wing section" [18, 19]. The 3D problem is reduced to a 2D problem by these structural approximations.

Starting with a typical wing section allows for the use of the well-known thin airfoil theory in aerodynamics. The preliminary assumptions involve having incompressible, inviscid airflow around an airfoil of zero thickness (and infinite span). Further approximations for simplicity are to assume that the airfoil is rigid with no airflow penetration and limited to small amplitude oscillations. Since much research on thin plates and airfoils exists in the fields of structural mechanics and aerodynamics, this is a great starting point for developing more sophisticated models that can begin to best represent a true aircraft wing with real flight conditions. The means by which this is done is through *higher order modeling* [16]. One can add more degrees of freedom, more accurate aerodynamics, better-defined constraints, and appropriate initial and boundary conditions to existing aeroelastic models to better describe the true nature of an aircraft's flight. These improvements obviously come with high computational expense in time and processing capabilities. Higher order modeling also introduces the possibility for more sources of error accumulation that should be accounted for in the final aeroelastic analyses.

2.1.1 Single Degree-of-Freedom

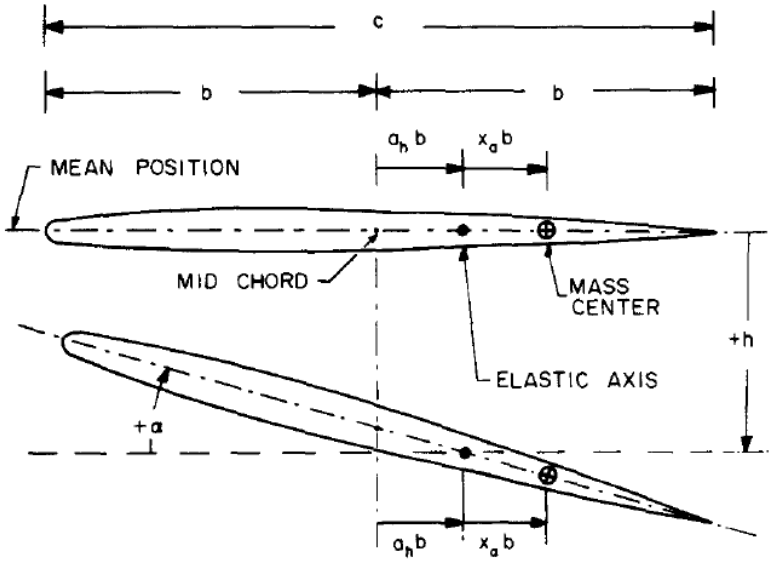

Figure 2.1: The one degree-of-freedom typical section is shown here with the two possible degrees of freedoms in pitch α and plunge h [20].

The simplest structural model to work with is a single degree-of-freedom model. A thin 2D airfoil is capable of two types of motion shown in Figure 2.1: rotation (or pitch) and translation (or plunge). For a single degree-of-freedom model, one of these two types of motion is assumed to be much more important than the other, which is then considered negligible. This determination is made by observing which of the two types of motion is significantly larger than the other for the aircraft and wing of interest. Usually, the rotational degree of freedom is considered more important because, in most cases, a wing or control surface will rotate much more significantly than it will bend when actuated by pilot input. Stabilators, particularly ones that are on fighter jets, demonstrate how great this disparity between rotation and bending of a wing can be as shown in Figure 2.2b. These wings rotate entirely at their roots. Their low aspect ratio prevents any significant longitudinal bending resulting from the lift they generate.

The mathematical modeling of a single degree-of-freedom aeroelastic system

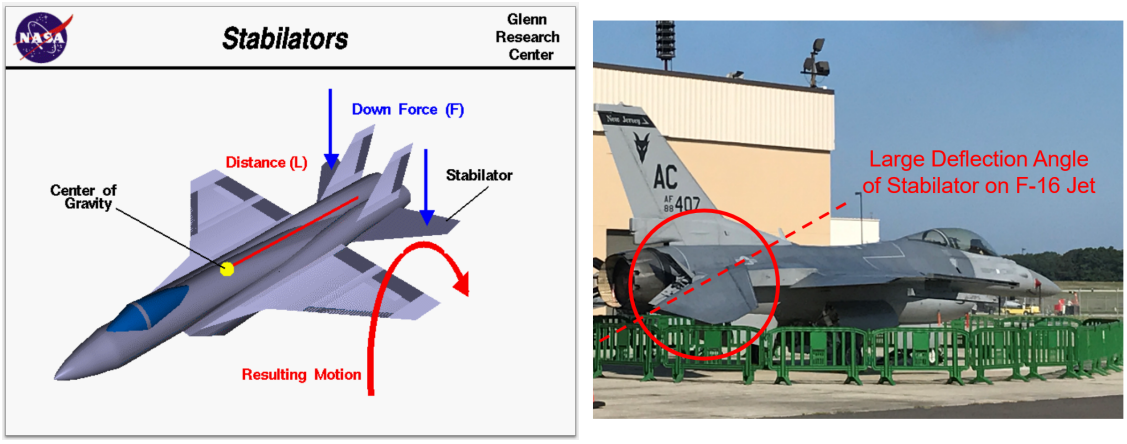

(a) (b)

Figure 2.2: Stabilators control the pitch of an aircraft, shown in (a), by rotating entirely at its root as shown in (b). Stabilators tend to be thin for fighter jets, shown on the left, as opposed to bluff bodied wings found on large commercial jets. Single degree-of-freedom modeling with a thin airfoil approximation is sufficient. Picture on the left obtained from NASA Glenn Research Center online multimedia [21]. Picture on the right taken by Mr. Jeet Panchal at FAA-TC in New Jersey.

only yields one equation of motion, such as Equation 2.1. Guruswamy and Yang [20] used the airfoil model shown in Figure 2.1 to carry out transonic aeroelastic analyses for a thin airfoil using the LTRAN2 code, and compared their results to subsonic theory. The equation of motion that they used for this system with only pitching motion α is

$$I_\alpha \ddot{\alpha} + C_\alpha \dot{\alpha} + K_\alpha \alpha = Q_\alpha. \tag{2.1}$$

In Equation 2.1, I_α is the mass moment of inertia of the thin airfoil, C_α is the damping coefficient in pitching, K_α is the rotational stiffness of the airfoil, and Q_α is the aerodynamic moment on the airfoil. The mathematical function for free play would replace K_α. The above equation can be written in non-dimensional form as

$$\alpha'' + A_1 \alpha' + A_2 \alpha = \frac{Q_\alpha}{I_\alpha \omega}. \tag{2.2}$$

The primes on the rotational angle α indicate differentiation with respect to non-dimensional time $\bar{t} = \omega t$ (where $\omega = \frac{2\pi}{t}$). A_1 and A_2 are non-dimensional constants for

the damping and stiffness, given by $\left(\frac{C_\alpha}{I_\alpha \omega}\right)$ and $\left(\frac{K_\alpha}{I_\alpha \omega^2}\right)$, respectively. Non-dimensional analysis allows important groups of parameters that are of most influence on a model's aeroelastic response to be identified. This type of dimensional analysis enables us to establish correct scaling and similitude that are needed for wind tunnel experiments.

Here, it should be noted that true structural damping is often disregarded across much of the literature due to the complexity it introduces. Structural damping within most aircraft systems is highly nonlinear [22, 23]. Viscous damping approximation is often made due to ease of calculations and analysis. Some researchers completely disregard any type of structural damping. For example, He et al. [24] studied the control surface buzz phenomena using describing functions by assuming no structural damping at the hinge line where the control surface attaches with the wing, as shown in Figure 2.3. Their governing equation of motion was

$$I_\beta \ddot{\beta} + M(\beta) = 2\rho V^2 b^2 c_m. \tag{2.3}$$

In Equation 2.3, β is the degree of freedom in rotation of a control surface, I_β is the control surface moment of inertia, and $M(\beta)$ is the function for the nonlinear hinge moment for the control surface. The structural forces on the left side of the equation are equated to the aerodynamic forces on the right, where ρ is the air density, V is the airspeed, b is the reference half-chord length of the airfoil, and c_m is the aerodynamic pitching moment coefficient about the hinge line. The non-dimensional form of Equation 2.3 is

$$\frac{1}{\omega_\beta^2}\ddot{\beta} + \frac{M(\beta)}{K_\beta} = \frac{2U^2}{\pi \mu {r_b}^2} c_m, \tag{2.4}$$

where ω_β is the frequency of oscillation for the control surface, μ is the mass ratio defined by $\mu = \frac{m}{\pi \rho b^2}$, r_β is the radius of gyration, and U is the reduced (non-dimensional) velocity given by $U = \frac{V}{b\omega_\beta}$.

A single degree-of-freedom model can also focus on the plunge motion h if the longitudinal bending of a wing is significantly greater than its rotation or twisting.

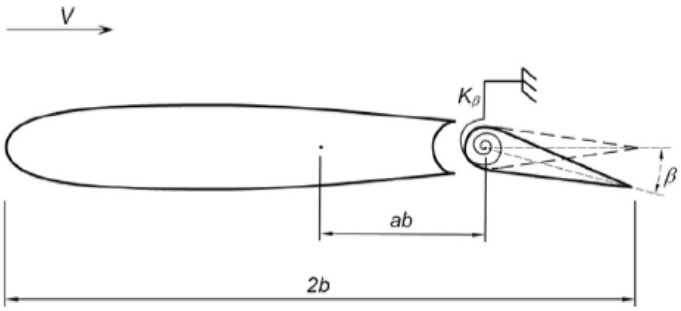

Figure 2.3: Control surface buzz is a single degree-of-freedom flutter instability that occurs in control surfaces during transonic flight due to the presence of shock waves on the wing or the control surface itself. The aeroelastic model used to study this phenomenon can be as simple as the one shown here, given by He et al. [24].

Such behavior is most observed in high aspect ratio wings, such as the main wings of commercial aircraft. These wings are designed to deflect significantly during normal flight to dissipate oscillatory aerodynamic forces. At the same time, the main aircraft wings are designed to undergo little to no twisting deformation during flight to prevent the aeroelastic instability of static divergence. There are several ways to model a single degree-of-freedom system with only plunging motion. Guruswamy and Yang [20] have examined this problem. The equation of motion that they used was

$$m\ddot{h} + C_h\dot{h} + K_h h = Q_h, \tag{2.5}$$

where m is the mass of the airfoil, C_h is the damping coefficient in plunging, K_h is the plunging stiffness of the airfoil that represents that bending stiffness of the wing, and Q_h is the lifting aerodynamic force acting on the airfoil. The mathematical function for free play would replace K_h. Utilizing the same non-dimensional approach as Equation 2.2, the above equation's non-dimensional form is

$$\delta'' + B_1\delta' + B_2\delta = \frac{Q_h}{m\omega^2 c}. \tag{2.6}$$

The δ is the non-dimensional plunge variable, B_1 and B_2 are constants, and c is the non-dimensional chord length of the airfoil.

Single degree-of-freedom systems with plunging free play can also be modeled differently from the classical airfoil approach described above. Li et al. [25] examined longitudinal deflection of a cantilevered plate fixed at one end and attached to a spring with free play on the opposite end, shown in Figure 2.4. The structural model

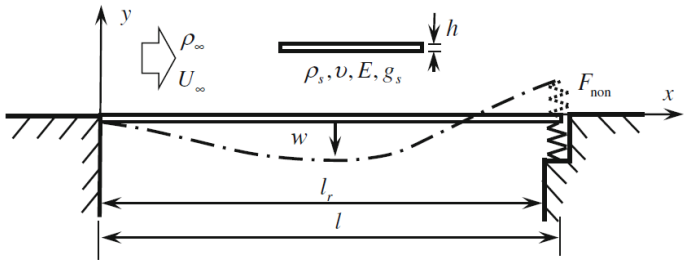

Figure 2.4: This type of cantilevered plate with free play can be used to model the behavior of loose aircraft skin attachments containing manufacturing or installation errors [25].

was subjected to longitudinal subsonic aerodynamic loads. The plunging deflection w of the plate is governed by the equation [25]

$$\begin{aligned}&\rho_s h\ddot{w} + Dw'''' + Dg_s\dot{w}'''' - \kappa(x)\left(\ddot{w} + 2U_\infty\dot{w}' + {U_\infty}^2 w''\right)\\&- \frac{\rho_\infty}{\pi}\left[\ln\left(\frac{x}{l}\right)\left(U_\infty\dot{w} + {U_\infty}^2 w'\right)|_{x=0} - \ln\left(1-\frac{x}{l}\right)\left(U_\infty\dot{w} + {U_\infty}^2 w'\right)|_{x=l}\right]\\&+ F_{non}\cdot\delta(x-l_r) = 0.\end{aligned} \tag{2.7}$$

It is interesting to see how Equation 2.7 takes a much different form than the other equations of motion described before for single degree-of-freedom systems. Details of Equation 2.7 are given in reference [25].

Single degree-of-freedom structural models with free play often have similar equations of motion. The simplicity of working with less variables and equations makes such models useful for initial analyses of complicated nonlinear systems. This simplicity allows researchers to explore the validity of novel analytical techniques before they apply them to systems with more degrees of freedom. For example, Liu et al. [26] were able to show that fractional dynamical systems with free play can be solved by validating their approach with a single degree-of-freedom system. The next steps involve adding an additional degree of freedom for more realistic 2D airfoil

behavior.

2.1.2 Two Degrees of Freedom

A thin airfoil with two degree-of-freedom aeroelastic systems has both pitching and plunging. There are many different ways that these airfoils can be diagrammed, as shown in Figure 2.5. All sketches include a torsional spring for rotational stiffness and a translational spring for plunging stiffness. The differences in these diagrams are in the relative locations of important airfoil and wing parameters such as center of gravity, elastic axis, pitching angle, and plunging displacement. All the sketches are valid for any aeroelastic analysis as long as the notation is kept consistent.

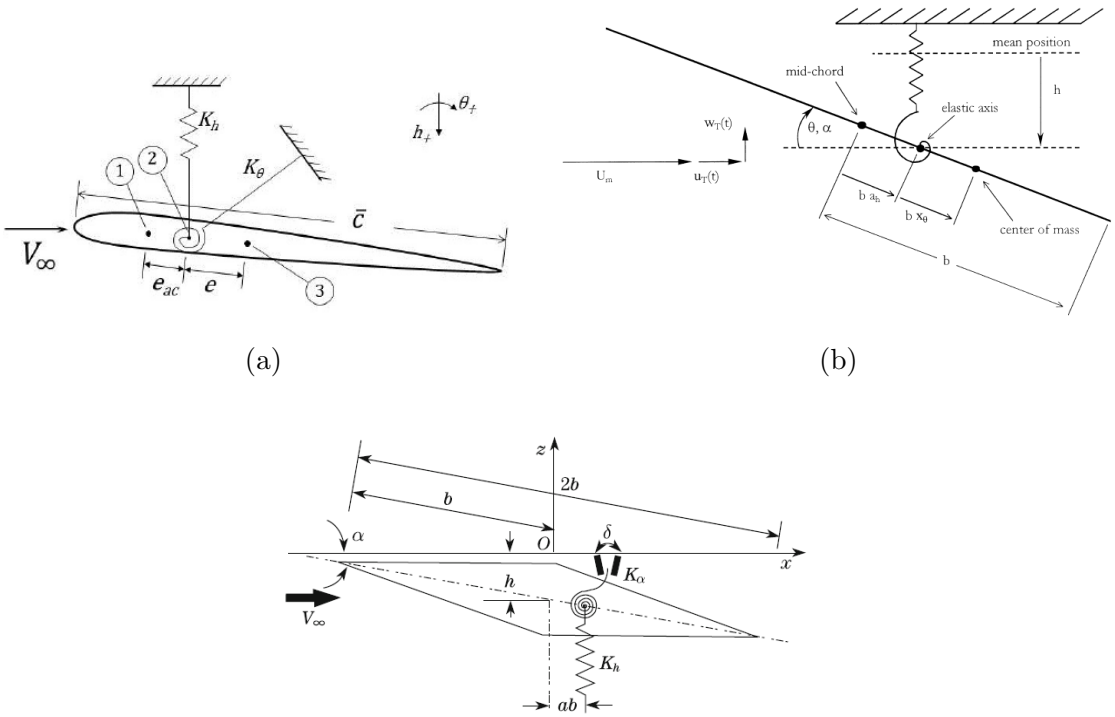

Figure 2.5: The slender plate and flat airfoils in subfigures (a) and (b), respectively, are typically used with subsonic aerodynamics [3, 27]. The double-wedge airfoil in subfigure (c) is commonly used with supersonic aerodynamics [28].

Two governing equations of motion are required to fully describe the dynamics

of two degree-of-freedom systems. As observed with one degree-of-freedom systems, the equations of motion for any two degree-of-freedom system will take identical forms. The standard equations of motion are

$$m\ddot{h} + S\ddot{\alpha} + C_h\dot{h} + \bar{G}(\alpha) = p(t) \tag{2.8a}$$

$$S\ddot{h} + I_\alpha\ddot{\alpha} + C_\alpha\dot{\alpha} + \bar{M}(\alpha) = r(t), \tag{2.8b}$$

where m is the mass, S is the airfoil static moment $\left(= \int_c x\rho_s dx\right)$, C_h and C_α are the damping coefficients in plunge and pitch, respectively, $\bar{G}(\alpha)$ and $\bar{M}(\alpha)$ are the plunge and pitch stiffness functions, respectively, and $p(t)$ and $r(t)$ are forces and moments acting on the airfoil, respectively [29]. $\bar{G}(\alpha)$ and $\bar{M}(\alpha)$ are functions of K_h and K_α, respectively. A matrix representation of Equation 2.8 is derived in Chapter 3.

The non-dimensional form of Equations 2.8 is [29]

$$\xi'' + x_\alpha\alpha'' + 2\zeta_\xi\frac{\bar{\omega}}{U^*}\xi' + \frac{\bar{\omega}}{U^*}^2 G(\xi) = -\frac{1}{\pi\mu}C_L(\tau) + \frac{P(\tau)b}{mU^2} \tag{2.9a}$$

$$\frac{x_\alpha}{{r_\alpha}^2}\xi'' + \alpha'' + 2\frac{\zeta_\xi}{U^*}\alpha' + \frac{1}{U^{*2}}M(\alpha) = \frac{2}{\pi\mu{r_\alpha}^2}C_M(\tau) + \frac{Q(\tau)b}{mU^2{r_\alpha}^2}, \tag{2.9b}$$

where the non-dimensional parameters are

$$\xi = \frac{h}{b},\ K_\xi = K_h,\ x_\alpha = \frac{S}{bm},\ \tau = \frac{Ut}{b},\ U^* = \frac{U}{b\omega_\alpha},$$

$$G(\xi) = \frac{\bar{G}(h)}{K_\xi},\ M(\alpha) = \frac{\bar{M}(\alpha)}{K_\alpha},\ \omega_\xi = \sqrt{\frac{K_\xi}{m}},\ \omega_\alpha = \sqrt{\frac{K_\alpha}{I_\alpha}},\ r_\alpha = \sqrt{\frac{I_b}{mb^2}},$$

$$\zeta_\xi = \frac{C_h}{2\sqrt{mK_h}},\ \zeta_\alpha = \frac{C_\alpha}{2\sqrt{I_\alpha K_\alpha}},\ \bar{\omega} = \frac{\omega_\xi}{\omega_\alpha},\ \mu = \frac{\pi\rho b^2}{m}.$$

Some new terms are introduced above. The terms ω_α and ω_ξ are the uncoupled plunging and pitching natural frequencies, μ is the airfoil to air mass ratio, r_α is the reduced radius of gyration about the elastic axis, x_α is the distance from elastic axis to the center of mass of the airfoil. The right hand sides of Equations 2.9 include the coefficients of lift and moment, defined as $C_L(\tau)$ and $C_M(\tau)$, and externally applied forces and moments, $P(\tau)$ and $Q(\tau)$. Since $P(\tau)$ and $Q(\tau)$ are not necessarily aerodynamic

contributions, they may be zero [29]. The aerodynamic contributions are accounted for through the $C_L(\tau)$ and $C_M(\tau)$, explained in Section 2.3.

The two degree-of-freedom structural model has been used for a variety of free play studies. The majority of the literature utilizes either two or three degree-of-freedom models for most types of aeroelastic analyses. Several novel analytical approaches have been tested with such structural models. Chung et al. [30] used a perturbation-incremental method in their aeroelastic analysis to calculate both stable and unable limit cycle oscillations and detect unique nonlinear periodic motions and bifurcations. De-Min and Qi-Chang [31] performed bifurcation and chaos analysis of a double wedge airfoil in supersonic and hypersonic flow using Poincaré mapping. Emory and Patil [32] used nonlinear normal modes to predict limit cycle oscillations for a two degree-of-freedom airfoil with a cubic nonlinearity. Several probabilistic analyses on two degree-of-freedom airfoils with structural nonlinearity in pitch have also been performed [27, 33].

A comparison of different numerical approaches have been done using this structural model. A reduction approach was used to simplify a typical pitch-plunge airfoil's aeroelastic model from eight ordinary differential equations in state space form to six ordinary differential equations for quicker simulation run time [34]. Dai et al. [35] also compare classical fourth order Runge-Kutta time integration numerical methods with Hénon's method for different representations of free play, verifying the work of Connor et al. [36] for a three degree-of-freedom system.

Similar to the single degree-of-freedom model, the two degree-of-freedom model provides a good platform on which to apply new analytical and numerical approaches to obtaining solutions for the free play problem. However, the additional degree of freedom allows researchers to study more complex nonlinear behavior that cannot be seen with a single degree of freedom model, while avoiding simulation issues that are often limiting factors in analyses with more degrees of freedom.

2.1.3 Three Degrees of Freedom and Higher

A variety of three degree-of-freedom and higher order models exist in the literature. Once again, these involve utilizing a "typical wing section" that is an airfoil modeled with more moving parts. The majority of the literature in the field of free play analysis uses two degree-of-freedom or three degree-of-freedom airfoils for their studies. The most common type of airfoil used in three degree-of-freedom models involves adding a control surface to the existing two degree-of-freedom airfoil from the previous section. This adds an extra pitching displacement variable β corresponding to the rotation of the added control surface. See diagrams in Figure 2.6.

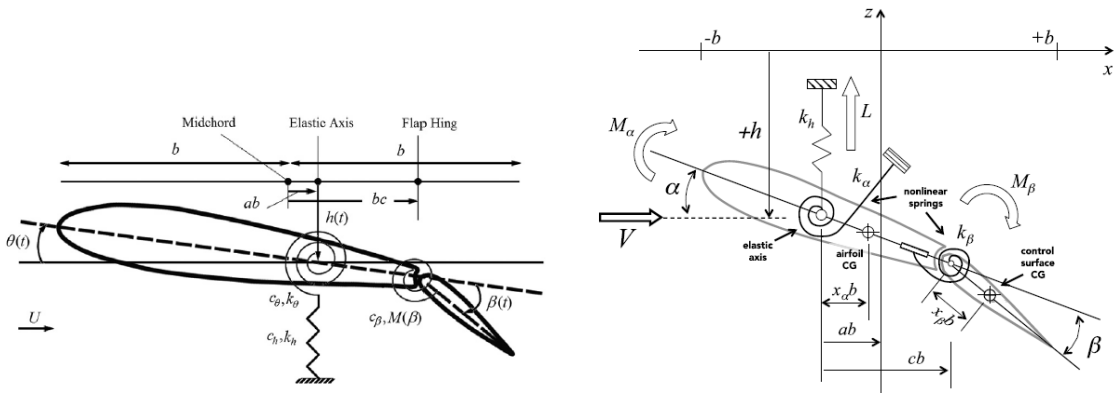

(a) (b)

Figure 2.6: Three degree-of-freedom models with airfoil and flap are generally alike in representation, with few differences such as the location of the coordinate systems that denote distances between important parameters of the airfoil, flap, and wing [37, 38].

Three governing equations of motion are required to fully describe the system. Consider the structural system in Figure 2.6a. The equations of motion for this system are [37],

$$m\ddot{h} + S_\theta\ddot{\theta} + S_\beta\ddot{\beta} + c_h\dot{h} + k_h h = L \tag{2.10a}$$

$$S_\theta\ddot{h} + I_\theta\ddot{\theta} + \left(I_\beta + b\left(c-a\right)S_\beta\right)\ddot{\beta} + c_\theta\dot{\theta} + k_\theta\theta = M_\theta \tag{2.10b}$$

$$S_\beta\ddot{h} + \left(I_\beta + b\left(c-a\right)S_\beta\right)\ddot{\theta} + I_\beta\ddot{\beta} + c_\beta\dot{\beta} + M\left(\beta\right) = M_\beta, \tag{2.10c}$$

where S_θ and S_β are the static moments of the airfoil and flap, k_h and k_θ are the plunge and pitch stiffnesses of the airfoil, c_θ and c_β are the rotational damping constants of the airfoil and flap, I_θ and I_β are the moments of inertia for the airfoil and flap, $M(\beta)$ is the pitch stiffness of the flap (where the free play nonlinearity is found), L is the aerodynamic lift on the airfoil, and M_θ and M_β are the moments on the airfoil and the flap. These equations can also be represented in the following non-dimensional form [39],

$$\xi'' + x_\alpha \alpha'' + x_\beta \beta'' + \frac{\Omega_1^2}{U^2}\xi = p \tag{2.11a}$$

$$\frac{x_\alpha}{r_\alpha^2}\xi'' + \alpha'' + \left[r_\beta^2 + (b_h - a_h)\, x_\beta\right]\frac{1}{r_\beta^2}\beta'' + \frac{1}{U^2}M_\alpha(\alpha) \;= r \tag{2.11b}$$

$$\frac{x_\beta}{r_\beta^2}\xi'' + \left[1 + (b_h - a_h)\,\frac{x_\beta}{r_\beta^2}\right] + \beta'' + \frac{\Omega_2^2}{U^2}M_\beta(\beta) = s. \tag{2.11c}$$

The non-dimensional relations necessary for the transformation to Equations 2.11 are [39]

$$\tau = \frac{Vt}{b},\ \xi = \frac{h}{b},\ r_\alpha = \sqrt{\frac{J_\alpha}{mb^2}}, r_\beta = \sqrt{\frac{J_\beta}{mb^2}}, \Omega_1 = \frac{\omega_\xi}{\omega_\alpha},\ \Omega_2 = \frac{\omega_\beta}{\omega_\alpha},\ U = \frac{V}{b\omega_\alpha},$$

where, p, r, and s are non-dimensional lift and moment contributions. Further explanations for the aerodynamics is provided in Section 2.3. These above equations can be given in matrix form as well. Using the structural model in Figure 2.6b, the matrix form of the equations of motion is [38],

$$[M]\{\ddot{q}\} + [C]\{\dot{q}\} + [K]\{q\} = \{F\}, \tag{2.12}$$

where,

$$[M] = \begin{bmatrix} \left(\frac{m_T}{m_w}\right) & x_\alpha & x_\beta \\ x_\alpha & r_\alpha^2 & \left[r_\beta^2 + (c-a)\, x_\beta\right] \\ x_\beta & \left[r_\beta^2 + (c-a)\, x_\beta\right] & r_\beta^2 \end{bmatrix}$$

$$[C] = \begin{bmatrix} d_{1,1} & d_{1,2} & d_{1,3} \\ d_{2,1} & d_{2,2} & d_{2,3} \\ d_{3,1} & d_{3,2} & d_{3,3} \end{bmatrix}$$

$$[K] = \begin{bmatrix} \omega_h^2 & 0 & 0 \\ 0 & \frac{r_\alpha^2 \omega_\alpha^2 F(\alpha)}{\alpha(t)} & 0 \\ 0 & 0 & \frac{r_\beta^2 \omega_\beta^2 F(\beta)}{\beta(t)} \end{bmatrix}$$

$$\{q\} = \begin{Bmatrix} \xi(t) \\ \alpha(t) \\ \beta(t) \end{Bmatrix}, \ \{F\} = \left(\frac{1}{b^2 m_w}\right) \begin{Bmatrix} -bL(t) \\ M_\alpha(t) \\ M_\beta(t) \end{Bmatrix}.$$

The values of the elements in matrix $[C]$ are given in [38]. The use of this type of structural model is widespread in the literature. Numerous free play studies have been conducted using this model. References [36, 40, 41, 42, 43] thoroughly cover three degree-of-freedom nonlinear aeroelastic systems.

Other three degree-of-freedom systems used for free play analysis include an airfoil with an external store attachment. Chen and Liu [44] explores an undamped, coupled airfoil model containing an attached store element free to pitch in the β direction, shown in Figure 2.7. This model contains free play in the airfoil pitch stiffness. The "precise-integration-method" is used to map out limit cycle oscillations and chaotic attractors, which are found to exist together. The governing equations of motion are

$$(m + m_\beta)\ddot{h} + (S_\alpha + S_\beta - m_\beta L)\ddot{\alpha} + S_\beta \ddot{\beta} + 2m\omega_h \zeta_h + K_h h = Q_h \tag{2.13a}$$

$$\begin{aligned}(S_\alpha + S_\beta - m_\beta L)\ddot{h} + \left(I_\alpha + I_\theta + m_\beta L^2 - 2S_\beta L\right)\ddot{\alpha} + 2I_\alpha \omega_\alpha \zeta_\alpha \\ + (I_\beta - S_\beta L)\ddot{\beta} + K_\alpha M(\alpha) = Q_\alpha\end{aligned} \tag{2.13b}$$

$$S_\alpha \ddot{h} + (I_\beta - S_\beta L)\ddot{\alpha} + I_\beta \ddot{\beta} + K_\beta \beta = 0. \tag{2.13c}$$

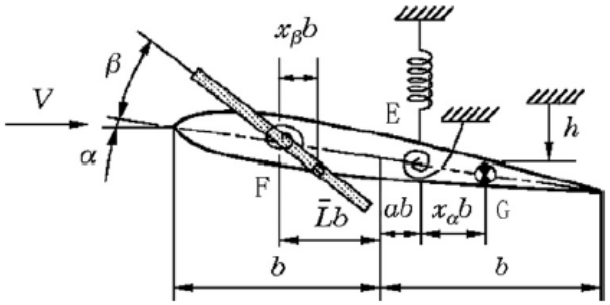

Figure 2.7: The external store element can be visualized as a rigid structure joined at a wing's tip [44].

Typically, researchers have dealt with the store attachment problem in different ways than Chen and Liu. The free play nonlinearity is usually explored with the store attachment, not the airfoil itself. This is because such a problem is experienced with jet aircraft that carry external fuel stores or missiles and weaponry. This type of free play results in low frequency vibrations of the external stores, causing aircraft cabin discomfort and potential structural fatigue [45, 46]. There is tremendous difficulty in establishing an adequate way of modeling this behavior. As opposed to a control surface that is constrained to rotational movement about its hinge line, an external store on a wing body can have free play in pitch, yaw, or roll, depending on how the attachments and its constraints are configured. There are challenges to modelling store free play problems. Limiting the motion and nonlinearity to a single degree of freedom leads to inaccuracies. References [45, 46, 47] detail the challenges in establishing reliable models with store free play.

Higher order 2D airfoil models exist but are not as commonly used for free play analysis due to the higher computational complexity and cost. A fourth degree of freedom γ was added to the airfoil-flap model with the addition of a trim tab [48]. See Figure 2.8 for diagram. This was explored by Al-Mashhadani et al. [48], who introduced a free play nonlinearity at the trim tab. The governing equations of

motion for such a system is given by

$$r_\alpha \ddot{\alpha} + \left[r_\beta^2 + (c-a)\, x_\beta\right] \ddot{\beta} + \left[r_\gamma^2 + (d-a)\, x_\gamma\right] \ddot{\gamma} + C_\alpha \dot{\alpha} + x_\alpha \ddot{h} + r_\alpha^2 \omega_\alpha^2 \alpha = \frac{M_\alpha}{mb^2} \quad (2.14a)$$

$$\left[r_\beta^2 + (c-a)\, x_\beta\right] \ddot{\alpha} + r_\beta^2 \ddot{\beta} + \left[r_\gamma^2 + (d-c)\, x_\gamma\right] \ddot{\gamma} + C_\beta \dot{\beta} + x_\beta \ddot{h} + r_\beta^2 \omega_\beta^2 \beta = \frac{M_\beta}{mb^2} \quad (2.14b)$$

$$\left[r_\gamma^2 + (d-a)\, x_\gamma\right] \ddot{\alpha} + \left[r_\gamma^2 + (d-c)\, x_\gamma\right] \ddot{\beta} + I_\gamma \ddot{\gamma} + C_\gamma \dot{\gamma} + x_\gamma \ddot{h} + r_\gamma^2 \omega_\gamma^2 \gamma = \frac{M_\gamma}{mb^2} \quad (2.14c)$$

$$x_\alpha \ddot{\alpha} + x_\beta \ddot{\beta} + x_\gamma \ddot{\gamma} + C_h \dot{h} + \frac{M}{h} \ddot{h} + \omega_h^2 h = \frac{L}{mb}, \quad (2.14d)$$

where

$$h = \frac{h_o}{b},\ x_a = \frac{S_\alpha}{mb},\ x_\beta = \frac{S_\beta}{mb},\ x_\gamma = \frac{S_\gamma}{mb},\ r_\alpha = \frac{I_\alpha}{mb^2}.$$

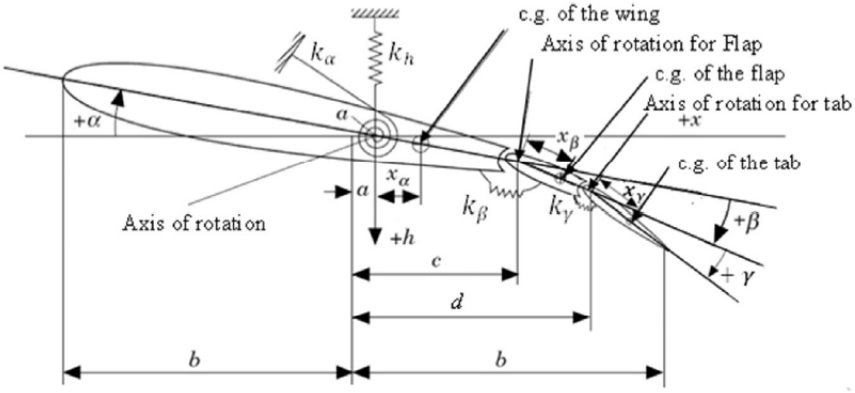

Figure 2.8: Most modern aircraft tend to have many control surfaces that can operate independently on a wing. This four degree-of-freedom model better represents modern wing structures than the models without a trim tab [48, 49].

Al-Mashhadani et al. [48] performed vibration and wind tunnel tests for a wing section corresponding to the model shown in Figure 2.8. While the experimental results matched well with the linear theory for the case of no free play, a comparison of the nonlinear theory developed in the paper and the experimental findings did not match too well. Kim and Lee [50] examined a flexible airfoil, shown in Figure 2.9, containing additional degrees of freedom in pitch and plunge about its elastic axis. The free play nonlinearity was introduced in the pitch. The equations of motion and the details of their research is beyond the scope of this paper. Interested readers can

see reference [50]. No experimental tests were conducted to verify the flexible airfoil model. While similarities were found between the dynamics of the nonlinear flexible airfoil and rigid airfoil responses, the work remains very theoretical in nature [50].

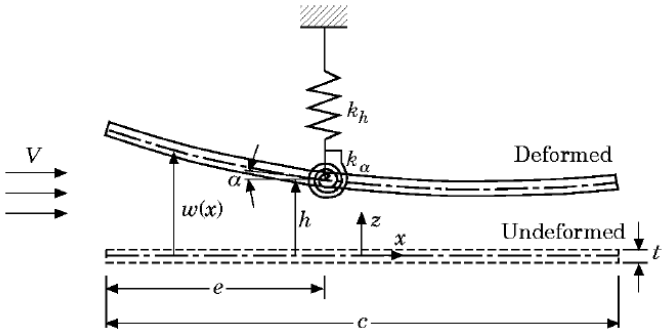

Figure 2.9: Flexible airfoils are popular in the research of micro-aviation. Their potential use is being examined for larger scale flight [50, 51].

It should be noted that 3D models are not covered in this review. However, one should be aware of the general type of 3D structural modeling that is available in the literature, should such a model be studied for the free play problem. Suppose a wing is modeled as shown in Figure 2.10. Using generalized coordinates $q_i(t)$ in the Cartesian coordinate system, 3D wing displacement can be expressed by [29],

$$z(x, y, t) = \sum_{i=1}^{N} \phi_i(x, y) q_i(t). \tag{2.15}$$

The function $\phi_i(x, y)$ is the mode shape for the i^{th} normal mode of the wing. N is the number of modes that will be used to best capture majority of the wing's dynamic aeroelastic response. Currently, the literature shows analyses including up to at least the fourth mode shape of a wing [14, 52, 53, 54]. The equation of motion is given for the generalized coordinate corresponding to the i^{th} mode is

$$M_i \ddot{q}_i + C_i \dot{q}_i + K_i q_i = F_i, \tag{2.16}$$

where M_i, C_i, and K_i are the generalized mass, damping, and stiffness given by

$$M_i = \int_A m \phi_i^2 dA$$

$$K_i = \int_S EI \left\{ \frac{d^2\phi_i}{dx^2} \right\} dx$$

$$C_i = \int_A p_{di}\,(x, y)\,\phi_i^2 dA.$$

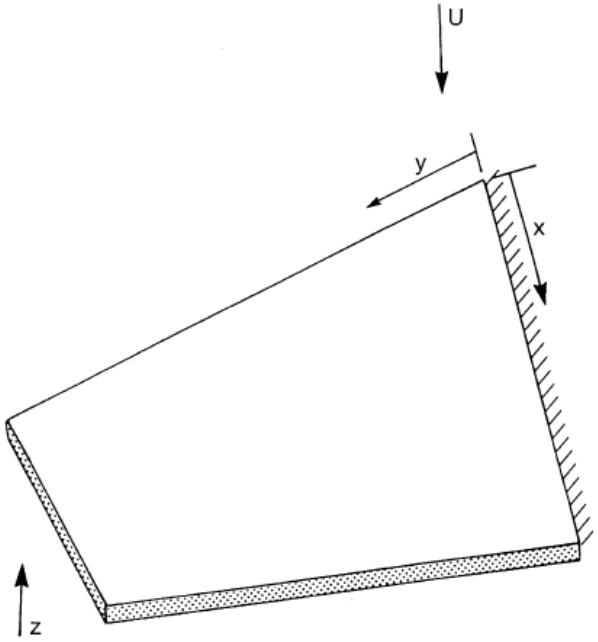

Figure 2.10: The coordinate system for a typical 3D wing typically originates at the connection point of the root and the leading edge of the wing [29].

To evaluate M_i, the integral is taken over the surface area of the wing. The integral for K_i is taken on the wing span, where EI is the flexural stiffness term. In the damping integral, p_{di} is local viscous damping pressure. The force is found by integrating the pressure over the wing area,

$$F_i = \int_A p\,(x, y, t)\,\phi_i dA.$$

This establishes the general framework needed to utilize a 3D structural model. Several schemes [8, 45, 55, 56] have been developed that can be used to solve Equation 2.16 when coupled with appropriate aerodynamics to obtain a variety of dynamic aeroelastic responses.

2.2 Free Play

Free play, sometimes referred to as backlash or a dead band, is a concentrated nonlinearity in the actuation of a wing or its control surface mechanism. It is a potential characteristic of moving parts that may be due to the looseness and tolerances in bolts, hinges, and actuators [57]. In the range of rotational values corresponding to free play, there will be free motion of the wing or control surface without resistance. In theory, a pure free play in a control surface hinge appears as a bilinear, piecewise function with a flat spot in a hinge moment versus deflection graph, as shown in Figure 1.1. However, free play can be simultaneously present with several other structural nonlinearities, such as friction and damping within moving parts, resulting in unique mappings on the moment-deflection graph [11].

The industry standard for measuring free play is based on static testing that involves applying a load to a control surface and measuring the linear or angular deflection. This can be done using a measurement device such as a Rotation Variable Differential Transformer (RVDT), shown in Figure 2.11.According Kiiskila et al. [57], free play testing is very laborious and time intensive, requiring complicated assembly for setting up test mechanisms. These ground tests may be performed at tall heights for rudder and stabilator measurements on larger aircraft. Although rudimentary, these tests must be conducted regularly throughout the service life of an aircraft to ensure compliance with regulatory standards of allowable amount of free play. Relatively new to the field of free play is a method for dynamically testing free play that was proposed by Kiiskila et al. [57]. Specific low and high frequency modes of vibration can be distinguished and have been shown to correspond to control surface motion inside and outside of the free play zones.

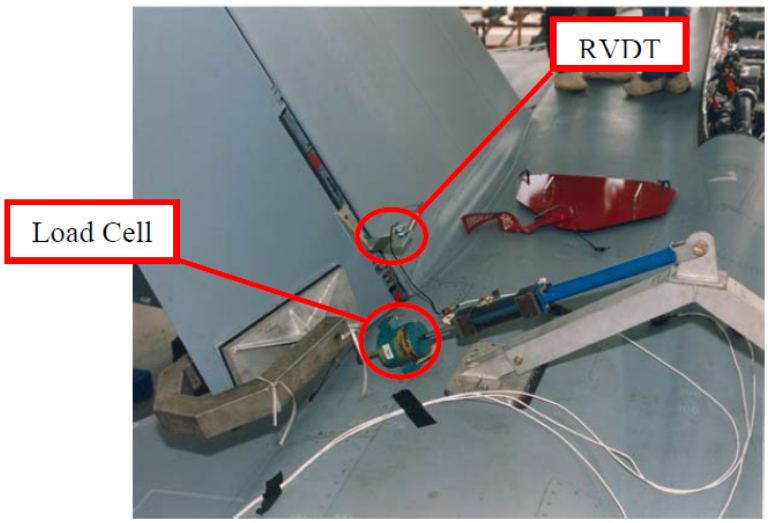

Figure 2.11: An RVDT measures the rotation between the rudder and the tail, with displacement and force measurements recorded by a hydraulic actuator and load cell [57].

2.2.1 Mathematical Representations

Curve fitting is used to generate moment functions that best represent typical moment-deflection curves obtained from static free play tests. Assuming that the free play nonlinearity graphs map identically to Figure 1.1, the moment equation for the control surface becomes [37]

$$M(\beta) = \begin{cases} k_\beta(\beta - \delta) & \text{for } \beta \geq \delta \\ 0 & \text{for } -\delta \leq \beta \leq \delta \\ k_\beta(\beta + \delta) & \text{for } \beta \leq \delta, \end{cases} \tag{2.17}$$

where, k_β is the rotational stiffness coefficient, β (arbitrarily chosen variable) is the rotational angle of deflection, and δ is the free play angle amount referenced from the neutral position of the control surface. The moment Equation 2.17 is inserted into the structural models where the nonlinearity appears, replacing the linear terms in the governing equations of motion. For example, if free play appears in the flap hinge for a three degree-of-freedom model, then $M_\beta(\beta)$ in Equation 2.11c would be replaced by Equation 2.17.

Due to the piecewise nature of Equation 2.17, several attempts have been made to reformulate the equation as a smooth function using approximation methods. One such method is the rational polynomial approach. This results in a moment equation that is the ratio of two polynomials [38],

$$M(\alpha) = \frac{a_0 + a_1\alpha + a_2\alpha^2 + a_3\alpha^3}{b_0 + b_1\alpha + b_2\alpha^2}, \tag{2.18}$$

where $a_i \ \ (i = 0, 1, 2, 3)$ and $b_i \ \ (i = 0, 1, 2)$ are constants that allow for the selection of the best fit curve. Usually, these constants are obtained from experimental data. Another approach to approximating Equation 2.17 is by using a tangent hyperbolic function, represented as [38],

$$M(\alpha) = \frac{1}{2}\left[1 - \tanh\left(\epsilon\left(\alpha + \delta\right)\right)\right](\alpha + \delta) + \frac{1}{2}\left[1 + \tanh\left(\epsilon\left(\alpha - \delta\right)\right)\right](\alpha - \delta). \tag{2.19}$$

In Equation 2.19, ϵ is the smoothness variable. As $\epsilon \rightarrow \infty$, Equation 2.19 converges to the piecewise form free play in Equation 2.17. Asjes et al. [3] represented the hyperbolic model differently, but required similar limiting conditions to match the hyperbolic function with the piecewise function. While these representations are useful, not all free plays map a flat spot in the moment-deflection graph.

Free play can also be characterized by a reduced stiffness in the actuation of a control surface. This can look like Figures 2.12. In both cases shown in Figures 2.12a and 2.12b, a third order polynomial can give good approximations of the moment-deflection graphs, with the moment equation for free play given by [29, 59]

$$M(\beta) = a_0 + a_1\beta + a_2\beta^2 + a_3\beta^3, \tag{2.20}$$

where $a_i \ \ (i = 0, 1, 2, 3)$ are constants. This cubic behavior at the nonlinearity is often associated with the hardening or softening of the stiffness as the control surface passes through the free play region. Although rare, spring softening is an important consideration because this phenomenon can occur when stiffness decreases as displacement is increased, such as in the case of buckling or kinetic heating at high Mach numbers

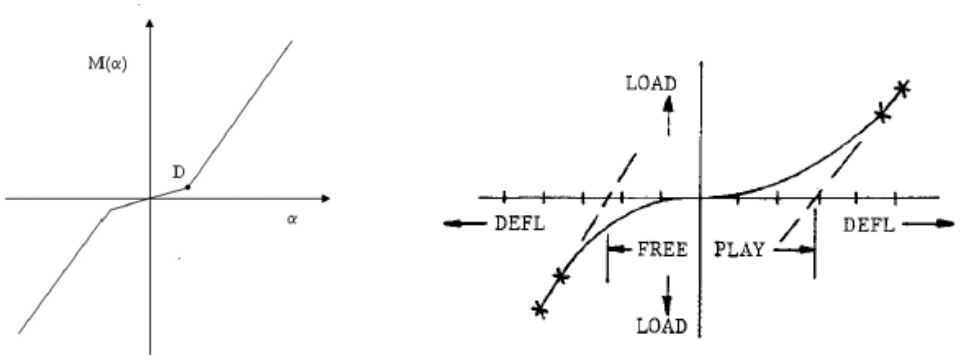

(a) (b)

Figure 2.12: The free play region can have sharp, linear changes in stiffness, as seen in subfigure (a), or have gradually changing stiffness that is nearly flat at the center and linear outside of the free play zone, as seen in subfigure (b) [4, 58].

[29].

Hysteretic effects can also be found with free play. This involves path dependent jump phenomena occurring between two linearly behaving sections on a moment-deflection graph that is offset by the value of the free play. Hysteresis, shown in Figure 2.13, can be the result of friction within moving parts. The moment equation, using the variables denoted in Figure 2.13, is [29]

$$M(\alpha) = \begin{cases} \alpha - \alpha_f + M_0 & \text{for } \alpha < \alpha_f; \alpha \text{ increasing} \\ \alpha + \alpha_f - M_0 & \text{for } \alpha > -\alpha_f; \alpha \text{ decreasing} \\ M_0 & \text{for } \alpha_f \leq \alpha \leq \alpha_f + \delta; \alpha \text{ increasing} \\ -M_0 & \text{for } -\alpha_f \leq \alpha \leq -\alpha_f - \delta; \alpha \text{ decreasing} \\ \alpha - \alpha_f - \delta + M_0 & \text{for } \alpha > \alpha_f + \delta; \alpha \text{ increasing} \\ \alpha + \alpha_f + \delta - M_0 & \text{for } \alpha < -\alpha_f - \delta; \alpha \text{ decreasing.} \end{cases} \tag{2.21}$$

In Equation 2.21, the slope of the lines extending beyond the hysteresis box is assumed to be 1 for sake of simplicity.

Up to this point, the major assumption in the moment equations containing free play has been that the free play nonlinearity lies only at the origin where the deflection is zero. This corresponds to the supposed neutral position of the control

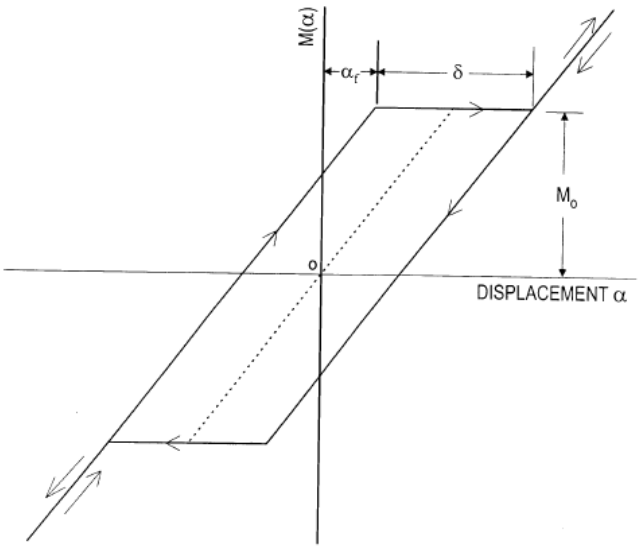

Figure 2.13: Static friction in a hinge or linkage may result in the measurements for a control surface free play that exhibits such a hysteresis phenomenon [12, 29].

surface. Control surfaces with preload tension can exhibit free play behavior translated away from the origin, as shown in Figure 2.14. The bilinear free play moment function associated with Figure 2.14 is [29],

$$M(\alpha) = \begin{cases} M_0 + \alpha - \alpha_f & \text{for } \alpha < \alpha_f \\ M_0 + M_f(\alpha - \alpha_f) & \text{for } \alpha_f \leq \alpha \leq \alpha_f + \delta \\ M_0 + \alpha - \alpha_f + \delta(M_f - 1) & \text{for } \alpha_f + \delta < \alpha. \end{cases} \tag{2.22}$$

In the equation above, M_f is the slope of the section where the free play is located.

Another lesser considered, but important, nonlinearity is solid friction. This is often present simultaneously with free play and significantly complicates the moment-deflection mapping of a control surface. Instead of a flat spot, friction maps a vertical spot in the force versus velocity graph as shown in Figure 2.15. More discussion on other similar concentrated nonlinearities can be found in reference [11].

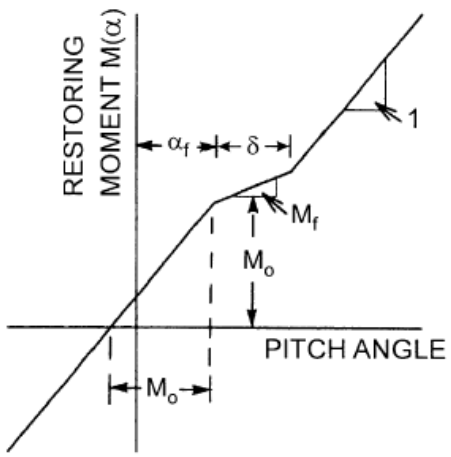

Figure 2.14: Free play does not always present itself when a control surface is at a neutral position. Sometimes the freeplay can resemble the graph shown here [29].

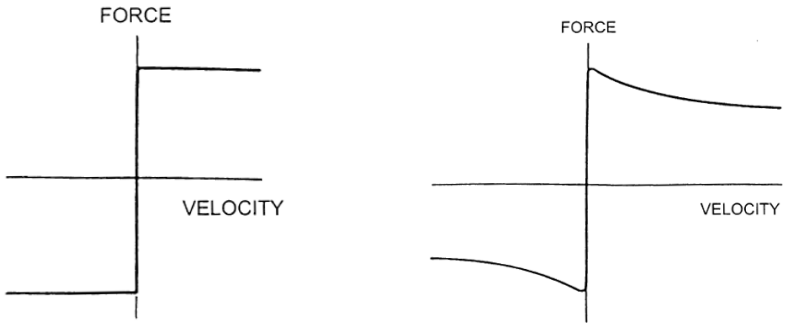

(a) (b)

Figure 2.15: An ideal static friction mapping on a force-velocity graph would like subfigure (a). In reality, the behavior more closely resembles subfigure (b) [29].

2.2.2 Applications in Literature

The literature on free play shows that predicted aeroelastic response can vary depending on the free play model that is used in the structural model. The piecewise form of free play, which is most commonly observed in the literature, yields some results and behavior that can only be predicted when the structural nonlinearity is described in this specific form. For example, if this type of free play is present at the root of an all

moving wing, then aeroelastic analyses show a reduction of critical flutter speed [60]. For very large free play angles, the dynamic instability of flutter turns into the static instability of divergence. Additionally, limit cycle oscillation (LCO) is exhibited over large range of velocities with dependence on initial condition, including free play gap size and angle of attack [61]. Using the piecewise form of free play does not, however, indicate any dependence between starting velocity of dynamic instability and the free play size [16].

Another important characteristic of the piecewise model of free play is that it is the only model that permits solutions that have chaotic behavior, often yielding complex periodic solutions that can settle into different attractors [36, 58]. Bifurcation analyses have also yielded interesting behavior such as subcritical bifurcations, grazing bifurcations, and period doubling that was specifically observed when this free play model is preloaded [30, 48, 62].

Comparisons with the cubic representation of free play shows slightly different behavior in some regards. The benefit of using this type of nonlinearity representation is that it is straightforward to use and does not run into the problem of smoothness. For example, Conner et al. [36] demonstrated that a non-smooth free play function is very sensitive to the choice and resolution of different numerical methods. Using a standard Runge-Kutta method alone resulted in a limit cycle solution set settling into an incorrect attractor. Using the modified approach of Hénon's numerical integration method allowed for more accurately locating switching points between linear subdomains of the free play region and yielding the correct limit cycle period. Some issues with a cubic model are that it does not show any dependence on initial conditions and does not show reduced speeds at which flutter is observed, something that has been proved experimentally. Cubic nonlinearity does contribute to LCO behavior, including results showing supercritical flutter behavior [3, 16].

Other lesser used free play models include the use of a hyperbolic function.

Asjes et al. [3, 1] were able to effectively use this function, but Vasconcellos et al. [59, 63] had difficulty obtaining satisfactory results and required corrections to match analytical results with experimental data. Very few studies have looked into aeroelastic analysis with the hysteresis model, but it has been shown that the dynamic response exhibits stable and unstable LCO, coexistence of LCO, saddle-node bifurcation, Neimark-Sacker bifurcation, chaotic motion at local and global levels, and other unique predicted behavior that is different from the piecewise model of free play [58, 64].

2.3 Aerodynamic Models

For analytical studies of free play that stem from the 2D structural models developed in the previous sections, correctly developing and using aerodynamic models is crucial to the overall aeroelastic analysis. In same manner as the structural models were developed, aerodynamic models begin with the fundamentals of unsteady aerodynamics. Research goals and needs dictate the level of complexity of the aerodynamic models. For large 3D structural models, computational fluid dynamics (CFD) codes are developed and used with various fluid-structural solvers.

2.3.1 Unsteady Aerodynamics

The aerodynamic forces and moments that correspond to the right-hand side of the governing equations of motion for the various structural models presented in the previous sections are time dependent. Due to the changing motion of the airfoil at different airspeeds and different instances in time, the flow-field around an airfoil will correspondingly change and vary with time. Thus, unsteady aerodynamics must be used in all of the aeroelastic models. The fundamental theories of unsteady aerodynamics were developed by Theodorsen [65] in the early 1930s. They are based on

potential flow involving small perturbations and harmonic motion. The unsteadiness of the flow is characterized by using functions of reduced frequency. The theory has many components and assumptions but can be simply stated through the circulatory and noncirculatory contributions that affect airfoil motion. Unsteady aerodynamics has been developed by many researchers and studied extensively [18, 19, 66, 67, 68]. We will not attempt any derivations in this chapter, but rather explain how unsteady aerodynamics is used in aeroelastic analysis with free play.

Using thin-airfoil theory, Theodorsen's unsteady lift and moment equations are [19]

$$L = 2\pi\rho_\infty UbC\left(k\right)\left[\dot{h} + U\theta + b\left(\frac{1}{2} - a\right)\dot{\theta}\right] + \pi\rho_\infty b^2\left(\ddot{h} + U\dot{\theta} - ba\ddot{\theta}\right) \tag{2.23a}$$

$$M_{\frac{1}{4}} = -\pi\rho_\infty b^3\left[\frac{1}{2}\dot{h} + U\dot{\theta} + b\left(\frac{1}{8} - \frac{a}{2}\right)\ddot{\theta}\right]. \tag{2.23b}$$

Equation 2.23 corresponds to Figure 3.1 in Chapter 3. The term $C\left(k\right)$ in Equation 2.23a is a function of reduced frequency k, where

$$C(k) = \frac{H_1^{(2)}(k)}{H_1^{(2)}(k) + iH_0^{(2)}(k)}, \tag{2.24}$$

and

$$H_n^2\left(k\right) = J_n\left(k\right) - iY_n\left(k\right), \ (n = 0, 1). \tag{2.25}$$

$H_n^2\left(k\right)$ are the Hankel functions of the second kind, represented by Bessel functions of the first and second kind, respectively [19].

It should be noted that the resulting unsteady aerodynamics equations involve integral terms. Combining these equations into the structural equations of motion results in the equations of motion being in integro-differential form. This can be tackled in several ways using approximations developed by workers in the field of unsteady aerodynamics.

The use of unsteady aerodynamics is extensive across the literature involving free play. Most of the aeroelastic analyses are performed using these theories. While

it would be cumbersome to discuss the many variations and uses observed in all of the literature, this section provides an example of its use for a two degree-of-freedom aeroelastic model. Due to the lengthiness of the derivations and resulting equations, examples of the use of unsteady aerodynamics for three and four degree-of-freedom aeroelastic models are omitted and referenced for additional reading.

Revisiting the non-dimensional form of the equations of motion for the two degree-of-freedom structural model described in Equation 2.9, and assuming no external force contributions (setting $P(\tau),\ Q(\tau)$ to 0), the coefficients of lift and moment for incompressible flow are given by Fung [68] as

$$\begin{aligned} C_L(\tau) &= \pi\left(\xi'' - a_h\alpha'' + \alpha'\right) + 2\pi\left\{\alpha(0) + \xi'(0) + \left[\frac{1}{2} - a_h\right]\alpha'(0)\right\}\phi(\tau) \\ &\quad + 2\pi\int_0^\tau \phi(\tau-\sigma)\left[\alpha'(\sigma) + \xi''(\sigma) + \left(\frac{1}{2} - a_h\right)\alpha''(\sigma)\right]d\sigma \end{aligned} \tag{2.26a}$$

$$\begin{aligned} C_M(\tau) &= \pi\left(\frac{1}{2} + a_h\right)\left\{\alpha(0) + \xi'(0) + \left[\frac{1}{2} - a_h\right]\alpha'(0)\right\}\phi(\tau) \\ &\quad + \pi\left(\frac{1}{2} + a_h\right)\int_0^\tau \phi(\tau-\sigma)\left[\alpha'(\sigma) + \xi''(\sigma) + \left(\frac{1}{2} - a_h\right)\alpha''(\sigma)\right]d\sigma \\ &\quad + \frac{\pi}{2}a_h\left(\xi'' - a_h\alpha''\right) - \left(\frac{1}{2} - a_h\right)\frac{\pi}{2}\alpha' - \frac{\pi}{16}\alpha''. \end{aligned} \tag{2.26b}$$

In the equations above, σ is a dummy variable used to perform the convolution integrals in the non-dimensional time domain τ. Using Jones' approximation with the Wagner function, we get [29]

$$\phi(\tau) = 1 - \psi_1\exp^{-\varepsilon_1\tau} - \psi_2\exp^{-\varepsilon_2\tau}, \tag{2.27}$$

where, $\psi_1 = 0.165$, $\psi_2 = 0.335$, $\varepsilon_1 = 0.0455$, and $\varepsilon_2 = 0.3$. Further simplification can be done by introducing new variables as done by Lee et al. [69],

$$\begin{aligned} w_1 &= \int_0^\tau e^{-\varepsilon_1(t-\sigma)}\alpha(\sigma)\,d\sigma,\ w_2 = \int_0^\tau e^{-\varepsilon_2(t-\sigma)}\alpha(\sigma)\,d\sigma \\ w_3 &= \int_0^\tau e^{-\varepsilon_1(t-\sigma)}\xi(\sigma)\,d\sigma,\ w_4 = \int_0^\tau e^{-\varepsilon_2(t-\sigma)}\xi(\sigma)\,d\sigma. \end{aligned} \tag{2.28}$$

Performing some algebra and rearrangement of terms, the governing equations of motion can be written in matrix form as a set of eight first-order differential equations,

as follows [29],

$$\dot{\boldsymbol{X}} = f\left(\boldsymbol{X}\right), \tag{2.29}$$

where $\boldsymbol{X}$ is a vector with eight components:

$$x_1 = \alpha,\ x_2 = \alpha',\ x_3 = \xi,\ x_4 = \xi',\ x_5 = w_1,\ x_6 = w_2, x_7 = w_3,\ x_8 = w_4.$$

Equation 2.29 can be solved numerically. A similar approach is employed by Dai et al. [35], where the governing equations of motion for a two degree-of-freedom model is reduced to a set of six first-order differential equations. Li et al. [42] and Sazesh and Shams [37] use similar frameworks to use unsteady aerodynamics for three degree-of-freedom structural models. Application to a four degree-of-freedom model is detailed in reference [48].

2.3.2 Compressibilty and Turbulence

Although subsonic unsteady aerodynamics theories are very useful for aeroelastic analyses involving free play, other nonlinear aerodynamic effects can significantly influence dynamic aeroelastic stability. Two main considerations include the effects compressibility and turbulence. Both of these considerations are relevant for modern flight as large commercial aircraft cruise at transonic speeds and may encounter random gust loads flying through turbulent air [70, 71].

At high subsonic and supersonic flow, compressibility effects must be considered. While a great body of research exists for individual treatment of subsonic and supersonic flow, the modeling of transonic flow is highly complex. This type of flow is characterized by a wing in high subsonic flow experiencing localized regions of supersonic flow, depending on its thickness, shape, and geometry. Transonic flow can induce shock waves on the wing or its control surfaces, reducing control surface effectiveness and resulting in premature aeroelastic instability in the form of control surface buzz, flutter, or LCO [16, 72, 73, 74]. Transonic flow can also bring about

destabilizing viscous effects that can cause flow separation due to shock wave and boundary layer interactions [29].

Although only a few studies have explored transonic and supersonic flight regimes for free play analysis, the general findings are that free play in both transonic and supersonic flow is severely destabilizing. The equations for both type of aerodynamics is nonlinear. However, the treatment of unsteady supersonic flow is more straightforward than transonic flow. In the literature for free play, the common treatment of supersonic flow is using local piston theory aerodynamics. Details on the derivation can be found in [40]. Guo and Chen [28] successfully used a second-order piston theory to examine supersonic and hypersonic flow with the structural model shown in Figure 2.5c. Assuming that only unsteady aerodynamic lift ($p\left(t\right) = -L$) and moment ($r\left(t\right) = M_{EA}$) are acting on the two degree-of-freedom double wedge airfoil, the right-hand sides of Equations 2.8 are respectively defined by piston theory as,

$$L = 4p_\infty \gamma M_\infty b \left(\frac{\dot{h}}{V_\infty} - ba\frac{\dot{\alpha}}{V_\infty} + \alpha \right) - p_\infty \gamma \left(\gamma + 1\right) M_\infty^2 b^2 \hat{\tau} \left(\frac{\hat{\alpha}}{V_\infty} \right) \tag{2.30a}$$

$$\begin{aligned} M_{EA} = p_\infty \gamma M_\infty b^2 \left(4 \left(a\frac{\dot{h}}{V_\infty} - \left(\frac{b}{3} + ba^2 \right) \frac{\dot{\alpha}}{V_\infty} + a\alpha \right) \right) \\ + \left(\gamma + 1\right) M_\infty \hat{\tau} \left(\frac{\dot{h}}{V_\infty} - 2ba\frac{\dot{\alpha}}{V_\infty} + \alpha \right), \end{aligned} \tag{2.30b}$$

where M_∞ is the Mach number, γ is the heat capacity ratio for an ideal gas, and V_∞ and p_∞ are freestream velocity and pressure, respectively. The study looked at piecewise free play and cubic nonlinearity, finding supercritical Hopf bifurcations, fold bifurcations, and LCO with a jump phenomenon in amplitude. Abbas et al. [75] used third-order piston theory for supersonic and hypersonic flows for a two degree-of-freedom double wedge structural model. They found subcritical flutter, chaotic behavior, and reduction in linear flutter speeds when examining different structural nonlinearities in all degrees of freedom.

When dealing with transonic flow, several different approaches exist. Bendiksen [71] provides an excellent overview of unsteady transonic aerodynamics modeling for aeroelasticity. Due to the complexity of these models, derivations and equations are omitted from this thesis. However, uses of various transonic aerodynamics theories are presented here with references to research involving free play. Kousen and Bendiksen [76] explored a two degree-of-freedom structural model with a torsional freeplay of ± 1 degree in transonic flow, which was modeled by CFD using inviscid 2D unsteady Euler's equations. This resulted in 75% reduction in linear flutter speed and multiple LCO behavior. Kholodar et al. [77] performed a similar analysis using a harmonic balance approach, as opposed to the time domain approach examined by Kousen and Bendiksen [76], and found that the resulting LCO in transonic regimes are highly sensitive to Mach number, exhibiting sudden changes in stability and behavior. Other studies have also used transonic small disturbance theory for conducting analyses on 3D structural models with free play, yielding similar results in premature degradation of aeroelastic stability [78, 79]. It is interesting to note that when Kim et al. [78] considered free play with boundary layer viscous effects in transonic flow with little to no separation, the reduction in flutter velocity was less severe and LCO amplitudes were decreased in comparison to the case of inviscid transonic flow.

When dealing with multiple structural and aerodynamic nonlinearities, the aeroelastic response for airfoils depends on the strength of the individual nonlinearities. Such is the case when dealing with turbulence. Poirel and Price [27] provide an excellent example of turbulence modeling with free play. They numerically examined stationary probability structure for the aeroelastic response of a two degree-of-freedom flat plate with cubic hardening nonlinearity in pitch, corresponding to Figure 2.5b. The vertical and longitudinal components of turbulence were modeled as stochastic differential equations shown below,

$$du_T + \frac{U_m}{L} u_T dt = \sigma_T \left(\frac{2U_m}{\pi L} \right)^{\frac{1}{2}} dW_1 \tag{2.31a}$$

$$
\begin{aligned}
&dw_T + \frac{2U_m}{L} w_T dt + \frac{U_m^2}{L^2} \left(\int_0^t w_T ds \right) dt \\
&= \sigma_T \left(\frac{U_m^3}{\pi L^3} \right)^{\frac{1}{2}} \left(\int_0^t dW_2 \right) dt + \sigma_T \left(\frac{3U_m}{\pi L} \right)^{\frac{1}{2}} dW_2,
\end{aligned}
\tag{2.31b}
$$

where u_T and w_T are the longitudinal and vertical components of turbulence, respectively. Additionally, U_m is the mean freestream velocity, L is the lift force on the plate, σ_T is the turbulence velocity standard deviation, and W_1 and W_2 are the two statistically independent Wiener processes. The solutions to Equations 2.31 are incorporated into modified unsteady aerodynamics to include time-varying airspeed and accounted for the governing equations with some mathematical manipulation. See reference [27]. The resulting solutions showed interesting "decoupled" nonlinear responses for the pitch, pitch rate, heave, and heave rate, where the marginal probability density functions of the response exhibited uni- to bi-modality at different airspeeds. For intermediate levels of turbulence, a double bi-modality is observed between pitch angle and mean airspeed. See Figures 2.16 on next page.

Low level turbulence, $\sigma_{T,nd}^2 = 0.01$:

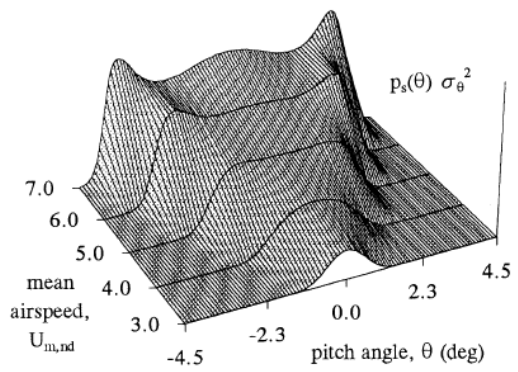

(a)

Intermediate level turbulence, $\sigma_{T,nd}^2 = 0.05$:

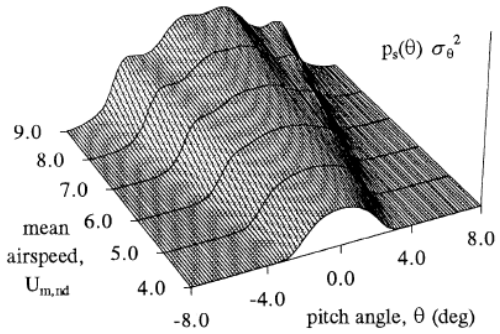

(b)

High level turbulence, $\sigma_{T,nd}^2 = 0.3$:

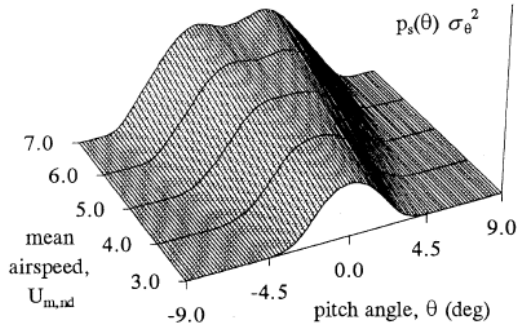

(c)

Figure 2.16: For increasing levels of turbulence, the aerodynamic effects overshadow the effects of structural nonlinearity [27].

2.4 Means of Analysis

In the field of aeroelasticity, a majority of the literature is deterministic. There are obvious difficulties with nonlinear deterministic calculations since few purely analytical methods can be employed to solve for all states of dynamic instability. However, many computational advances have been made in aeroelasticity for both deterministic and non-deterministic methods. Some of the main methods are highlighted in this section. In both approaches, classical theories from nonlinear dynamics and dynamic aeroelasticity must be employed to qualitatively understand the resulting aeroelastic behavior. Several important references in these fields include [18, 19, 40, 68, 70, 80].

2.4.1 Deterministic Approaches

The literature on free play shows two predominant analysis approaches: time domain solutions and frequency domain solutions. Numerical time integration provides a straightforward manner to map the time history of the governing equations of motion. Several numerical schemes have been successfully employed that involve discretizing the equations of motion at instants in time with small integration step sizes. Modified forms of the fourth order Runge-Kutta method are the most popular in the literature and allow for efficient numerical integration [29, 40]. While the standard Runge-Kutta method is useful for the smooth functions, there are known issues with its use when the aeroelastic model contains the piecewise representation of free play. It was shown to map the incorrect limit cycle oscillations, bifurcations, or chaotic attractors, regardless of how small the step size may be, due to errors in accurately locating switching points [35, 36]. This an issue that has been addressed, resulting in modified numerical approaches. The main drawbacks in time marching come from the high computational expense for increased accuracy in results. While several reduction methods and numerical schemes have been developed to target this issue, challenges

still remain [18, 34].

The frequency-domain analysis involves balancing the Fourier components of dominant harmonics to an assumed motion of response that is an expansion of the aerodynamic input to the aeroelastic system. This is known as the harmonic balance method, or the describing function technique. It was first used by Shen [13]. The major difficulty with the use of harmonic balance methods for nonlinear aeroelastic systems free play is that a large number of harmonics are required to obtain accurate solutions [69]. Regardless, higher order harmonic balance has been employed in numerous instances [46, 81, 82]. A thorough review of these frequency domain methods can be found in [32].

2.4.2 Non-Deterministic Approaches

Limited research exists on the application of a probabilistic or stochastic framework for the modeling of control surface free play nonlinearities in wing structures. Due to the complexities and variations in aircraft wing structures, and the large number of uncertainties and randomness in the fluid-structure interactions, developing an adequate aeroelastic model with the free play nonlinearity is already a difficult task. Many simplifications and assumptions are necessary to establish a model that can yield meaningful solutions to this problem. As a result, much of the literature examines this problem deterministically, employing unique analytical and computational methods that map out various solutions for specific wing sections in selected aerodynamic models, as explained in the previous sections. Substantial experimental work has also been done to validate some of these models. By examining published data, there are clearly many variabilities in the parameters that define the freeplay problem and therefore uncertainties in the solutions for the dynamical structural response of wings.

Four sources of uncertainties in the formulation of the free play problem are

stochastic variations in material properties, structural dimensions, boundary conditions, and external excitations [33, 83, 84]. Historically, external excitations have been predominantly examined while the other variations have been assumed negligible or accounted for arbitrarily into engineering analyses via factors of safety. However, this perception has changed over the years. The technology in the aerospace industry is becoming increasingly sophisticated with more structural parameters that behave flexibly and nonlinearly, such as composites. Other flight variations also need to be accounted for, such as inertial changes and mass changes (fuel consumption and cargo movement). Furthermore, predictions for aged aircraft cannot be easily quantified with deterministic methods alone. There is a strong desire for the use of stochastic methods within the industry to help prevent over-design and minimize costs [85, 86].

A basic type of uncertainty analysis is synthesizing probabilistic models numerically from deterministic models via sampling. Yi and Zhichun [33] demonstrated this with Monte Carlo simulations performed on a two degree-of-freedom system in incompressible flow with preloaded freeplay, with the airfoil moment, free play amount, and stochastic initial pitching angle assumed to be Gaussian random variables. Nonparametric estimation was then used to obtain a probability density function (PDF) for the response. Sensitivity analysis was also performed to quantify the strongest parameters of influence and probabilistic aeroelastic analysis was used to determine the stability of the airfoil system. Similarly, Pitt et al. [86] used a Monte Carlo simulation for random reduced frequency ranges to develop a probabilistic characterization of flutter for a two degree-of-freedom airfoil with unsteady aerodynamics. Advanced simulation methods, such as integrated interpolation methods with polynomial chaos expansion, have been found to be computationally quicker than Monte Carlo methods, but accuracy in results remain a concern [87].

More sophisticated uncertainty quantification methods have been examined by several researchers in application to aeroelastic systems, but few deal with geometric

nonlinearities. Mignolet and Chen [88] examined broad application of nonparametric stochastic modeling with geometric nonlinearity to assess variability of panel flutter boundary and response to forced acoustic excitation. Control based methods, such as iterative learning control and robust flutter analysis via perturbation approach, have also examined parametric uncertainty of nonlinear systems [89, 90]. Yuting and Chao [85] provide an overview of such control based methods and further developments in methods for aeroelastic analysis with uncertainties. A detailed review of uncertainty modeling with reduced order models and robust active control methods is discussed in reference [16]. Parallels to such methods exist with problems involving free play in landing gears [91].

Other types of lesser-used probabilistic or stochastic models have been developed. For example, Stanford and Beran [56] examined a reliability-based design optimization approach using perturbation methods and employing constraints on maximum allowable flutter probability. Parametrically uncertain boundary conditions with random torsional stiffness and nondeterministic panel thickness are analyzed to optimize minimal mass for panels. Stochastic random aerodynamic excitation is another common model that has been applied to the free play problem. Some of the earliest discussions on these models are found in [27, 29, 92]. More recently, spectral analysis methods have been successfully utilized [93]. Other recent contributions include works from Irani et al. [94] and Sazesh and Shams [37], who examine flutter with the novel approach of using response variance of flap angle to identify flutter instability under stochastic loading of a three degree-of-freedom airfoil. Work in the probabilistic area is promising for the field aeroelasticity.

2.5 Experimental Studies

The results from the aeroelastic analyses described in the previous sections provide a fundamental understanding of expected dynamic behavior with free play structural nonlinearities. These theoretical results must then be validated and supplemented by experimental studies to better understand the free play problem. Combined, both theoretical and experimental studies ultimately contribute to establishing the safe operating flight envelope for an aircraft. However, performing controlled flutter testing with free play is a difficult task. Initial experimentation takes place in wind tunnels, where representative wing sections are used. In this area of research, there have been very few extensive experimental studies. Very little has changed from the earliest free play experiments first conducted in 1955 by Woolston et al. [12]. The setup involved placing a straight wing horizontally in a wind tunnel. The wing was only allowed to move in the pitch and plunge directions, with restoring moments provided by springs. A measured gap was placed in the torsional axis of the system to represent the free play, as shown in Figure 2.17. Then air was pushed down the wind tunnel with gradually increasing speed until flutter was reached.

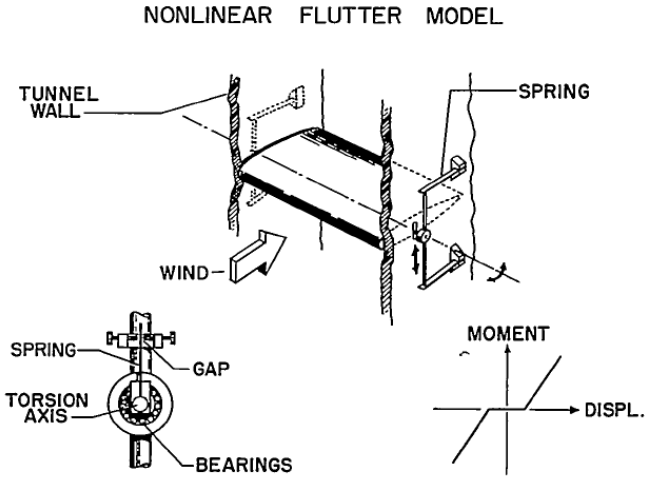

Figure 2.17: This type of experimental setup represents a two degree-of-freedom model. Displacement measurements were recorded electronically [12].

There were many issues with this type of setup, primarily with lack of control over a neutral starting position when experiments were conducted. By rotating the wing section and flutter apparatus vertically, better control over initial conditions was achieved by limiting the influence of weight as well as friction on linear bearing. O'Neil [95] set up such a test apparatus. See Figure 2.18a. One of the main issues with flutter testing is preventing the tests from reaching divergence. Otherwise, repeatability is not possible and potential destruction of the test section or damage to the flutter apparatus and equipment within the wind tunnel can occur. As a result, only limited motion is allowed by means constraints in the pitch and plunge direction. This mechanism is shown Figure 2.18b.

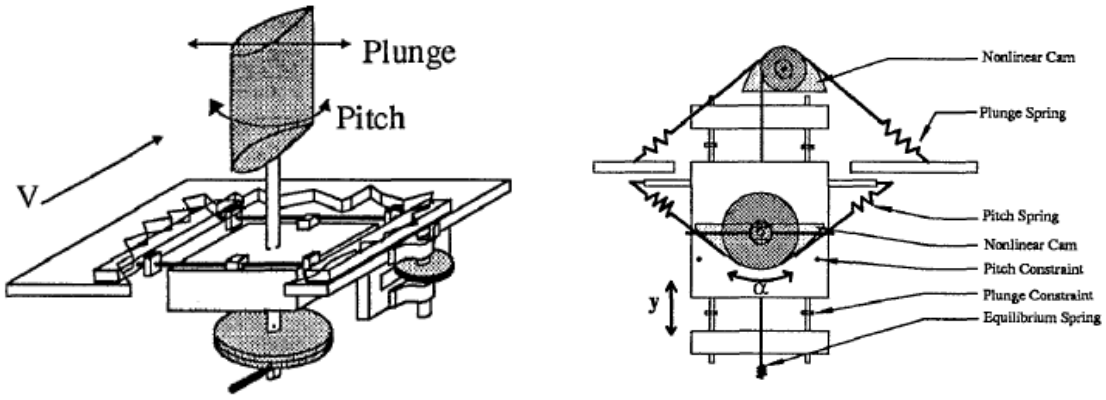

(a) (b)

Figure 2.18: The mechanisms shown here enable controlled nonlinear pitching and plunging motion and removes effects of gravity on the test wings [95].

The experiments were performed within a subsonic 2' x 3' wind tunnel at Texas A & M University, with accelerometers measuring frequency response for each degree of freedom. This study was one of the first of its kind that was able to examine flutter conditions for continuous nonlinear restoring forces, particularly with hardening and softening stiffnesses [95].

More recently, similar experiments with two, three, and four degree-of-freedom straight wing sections have been conducted, yielding more useful data due to better

instrumentation. Unique methods for controlling free play have been developed. For example, Marsden and Price [96] used a clearance hole of varying size with a connection between two pulleys connecting the wing section to a system of spring cables providing torsional stiffness. See Figure 2.19a. Tang and Dowell [47] and Connor et al. [97] used a leaf spring support with a gap to imitate free play in pitch for a two degree-of-freedom and three degree-of-freedom model, respectively. See Figures 2.19b. Abdelkefi et al. [98] and Vasconcellos et al. [63] repeated both experiments with an open-circuit blow wind tunnel using a foam-aluminum-fiberglass wing, using the set up shown in Figure 2.20. Lastly, Al-Mashhadani et al. [48] performed an identical wind tunnel experiment as Connor et al. [97], except with a four degree-of-freedom wing section involving free play in the trim tab.

While these experimental studies provide good data for validating theoretical results, they lack complexity and do not use appropriate similitude methods to appropriately model aircraft wings. Commercial aviation wing control surfaces usually do not extend the full span of a wing. Often, wings contain more than one control surface that can move independently. On a commercial jet, the wing can have a control surface in the front known as a slat. Other control surfaces include flaps, flaperons, and spoilers, some of which only rotate in one direction above or below the wing and can also extend longitudinally [49]. Most of the experiments in the literature fail to consider these situations. Furthermore, most of the experiments are in low speed wind tunnels where results do not entirely correlate to actual flutter experienced during flight. There are a few exceptions, however. Fichera and Ricci [81] developed a scaled H-tail model for wind tunnel testing with free play in the rudder. Morino and Obayashi [100] performed a high-speed wind tunnel test with a scaled horizontal stabilizer wing with free play in its control surface.

There are challenges and difficulties in performing controlled wind tunnel flutter tests using correct similitude methods with structural nonlinearity and simulating

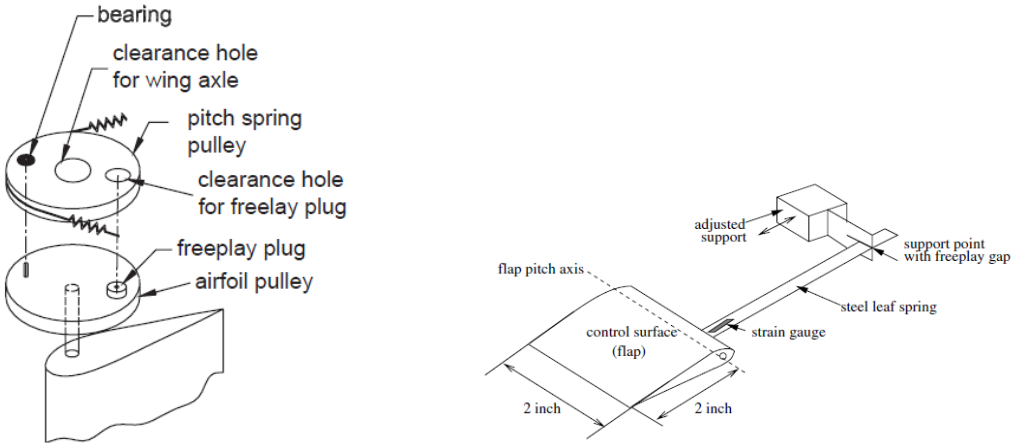

(a) (b)

Figure 2.19: Two different methods for establishing free play are shown, with both confirming accuracy with the respective theoretical models used by the researchers [96, 99]

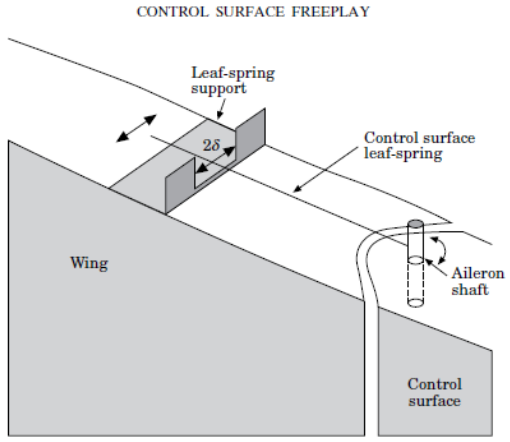

Figure 2.20: The mechanism from Figure 2.19b can be extended to control surfaces such as a flap or trim tab, while maintaining complete stiffness in the wing [97].

appropriate aerodynamic conditions. There is always a risk of failure regardless of how well planned and controlled an experiment is, as observed with the high-speed wind tunnel tests conducted by Morino and Obayashi [100]. For these reasons, flight flutter testing is still the most important method to define an aircraft's flight envelope and meeting safety and reliability requirements, despite being very costly and time consuming [101].

2.6 Gaps and Future Trends

Despite the extensive research on free play, many aspects of the problem are not fully developed or examined in entirety due to the complex nature of the model formulation and analysis. While it is generally accepted that free play increases accumulated damage and reduces fatigue life of aircraft wing structures, there are only very limited publicly available studies that document or model the entire phenomenon, mostly due to the scale and cost of performing such studies [57]. Furthermore, much of the literature does not consider the effects of internal damping in their models. Many models make assumptions on the geometry and mass distribution of aircraft wings as being straight and uniform. Additionally, variations in material composition, combined with variable mass distribution and planforms often found in modern aircraft, are also limited in the study of free play. Few studies have really examined the variations in angle of attack on free play [33, 60, 61, 102]. Finally, one of the main limitations of many models is that their validity is reserved to small angles of free play. Models with large angle deflection and large amount of free play are difficult to verify experimentally due to high risk of catastrophe. Little is known about the behavior for large angles of airfoil motion with free play, mostly because such scenarios are extreme and rare circumstances in modern aviation. Some other lesser-examined areas of research include combining acoustic, thermodynamic, and frictional or drag-related effects due to compressibility. Although these are just some of the shortcomings in current research regarding free play, existing research is, however, well established with good agreement on the results from much of the research community, thus enabling further growth and development in future studies.

Chapter 3

Aeroelastic Model

3.1 Structural Model

The initial formulation of the aeroelastic model begins with the derivation of the equations of motion that govern the simplest type of wing section: a thin, rigid, symmetric airfoil with two degrees of freedom, in pitch θ and plunge h, as shown in Figure 3.1. A detailed discussion about the assumptions involved is given in Section 2.1. The straight line distance measured from the leading edge to the trailing edge of the airfoil is known as the chord length. In Figure 3.1, the chord length is $2b$, where b is an arbitrary length constant.

The elastic axis (EA) of the wing, located at point P in Figure 3.1, is the origin from which the airfoil pitch and plunge are measured. The springs k_h and k_θ act at this point, representing the restoring translational and rotational stiffnesses of the wing, respectively. Point P is also the center of origin for both the local coordinate system unit vectors $(\hat{\boldsymbol{b}}_1, \hat{\boldsymbol{b}}_2, \hat{\boldsymbol{b}}_3)$ and the global Cartesian coordinate system unit vectors $(\hat{\boldsymbol{i}}_1, \hat{\boldsymbol{i}}_2, \hat{\boldsymbol{i}}_3)$. Points Q and C are the aerodynamic center (AC) and center of gravity (CG), respectively. AC is the point on an airfoil about which the aerodynamic pitching moment stays constant, regardless of the airfoil pitch angle (or angle of attack). For

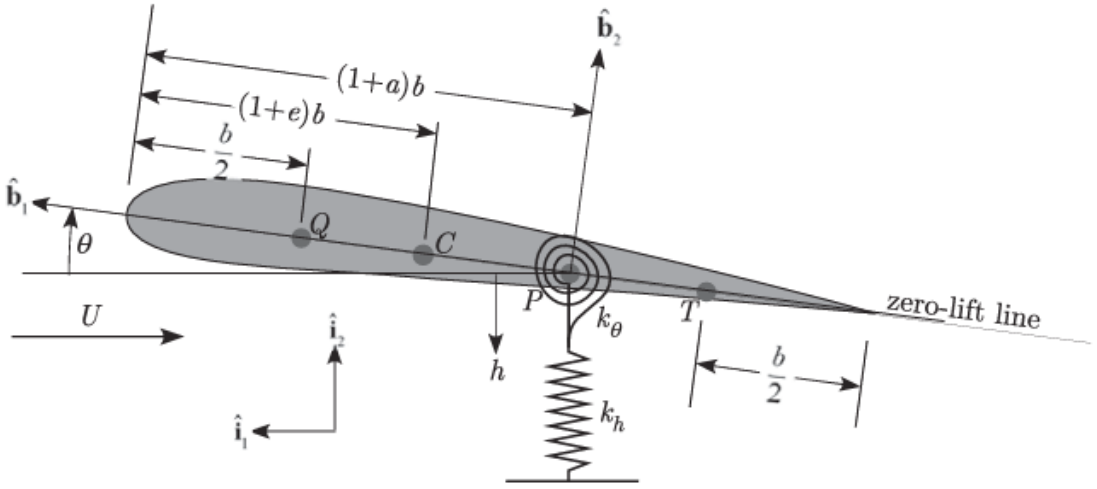

Figure 3.1: This "typical section" is a representative model of a thin airfoil used in many models across the literature [19].

an uncambered, flat airfoil, the location of AC is at quarter-chord from the leading edge, at point Q. The aerodynamic lift force, which acts through the center of pressure of the airfoil, is also located at the quarter-chord. The center of pressure is the point on an airfoil where the total pressure can be assumed to be acting through [18].

The relative locations of EA (point P) and CG (point C) are taken by measuring the distance of each point from the leading edge of the airfoil and representing that quantity as a scalar multiple of half the chord length b. These locations depending based on the mass distribution of the wing. Here, locations of EA and CG are given as $(1+a)b$ and $(1+e)b$, respectively, where a and e are non-dimensional constants that account for the variability in the locations of EA and CG on different wing sections. True values of a and e are usually obtained experimentally [19].

The relationship between the two local and global coordinate systems is very important. The axes of both unit vectors $\hat{\boldsymbol{b}}_3$ and $\hat{\boldsymbol{i}}_3$ coincide, pointing inwards perpendicular to the plane of the coordinate system shown in Figure 3.1. Thus, the relationship between local and global coordinate systems is described by a clockwise

rotation about $\hat{\boldsymbol{b}}_3 = \hat{\boldsymbol{i}}_3$, where $\hat{\boldsymbol{i}}_1 \times \hat{\boldsymbol{i}}_2 = \hat{\boldsymbol{i}}_3$ and $\hat{\boldsymbol{b}}_1 \times \hat{\boldsymbol{b}}_2 = \hat{\boldsymbol{b}}_3$. Thus,

$$\begin{Bmatrix} \hat{\boldsymbol{b}}_1 \\ \hat{\boldsymbol{b}}_2 \end{Bmatrix} = \begin{bmatrix} \cos(\theta) & \sin(\theta) \\ -\sin(\theta) & \cos(\theta) \end{bmatrix} \begin{Bmatrix} \hat{\boldsymbol{i}}_1 \\ \hat{\boldsymbol{i}}_2 \end{Bmatrix}. \tag{3.1}$$

We will need to use this relationship in the subsequent derivation of the equations of motion for the two degree-of-freedom airfoil in Figure 3.1.

3.1.1 Derivation of EOM for 2-DOF Airfoil

The calculus of variations is used to derive the equations of motion (EOM) for the airfoil. First, the potential (strain) energy of the system is calculated,

$$PE = \frac{1}{2}k_h h^2 + \frac{1}{2}k_\theta \theta^2. \tag{3.2}$$

Next, we derive the expression for the airfoil's kinetic energy, which is a bit more involved because it must be calculated with respect to the center of mass of the airfoil. The kinetic energy is expressed as

$$KE = \frac{1}{2}m\boldsymbol{v}_C \cdot \boldsymbol{v}_C + \frac{1}{2}I_C\dot{\theta}^2, \tag{3.3}$$

where m is the mass of the airfoil, and $\boldsymbol{v}_C$ and I_C are the velocity vector and moment of inertia at point C, respectively. The velocity vector at point C is related to the plunge and rotational displacements caused by airfoil motion at point P,

$$\begin{aligned} \boldsymbol{v}_C &= \boldsymbol{v}_P + \dot{\theta}\hat{\boldsymbol{b}}_3 \times \boldsymbol{r}_{PC} \\ &= \boldsymbol{v}_P + \dot{\theta}\hat{\boldsymbol{b}}_3 \times b\left[(1+a) - (1+e)\right]\hat{\boldsymbol{b}}_1. \end{aligned} \tag{3.4}$$

In Equation 3.4, $\boldsymbol{v}_P$ is the plunge velocity vector at point P. From Figure 3.1, we see that the defined plunge displacement direction is downwards, which immediately tells us that $\boldsymbol{v}_P = -\dot{h}\hat{\boldsymbol{i}}_2$. The second term in Equation 3.4 is the tangential velocity contribution from the angular velocity, which is given by the cross product of the angular velocity and the distance to point C from point P. Carrying out the algebra

in Equation 3.4 yields

$$\boldsymbol{v}_C = -\dot{h}\hat{\boldsymbol{i}}_2 - b\dot{\theta}x_\theta\hat{\boldsymbol{b}}_2, \tag{3.5}$$

where $x_\theta = e - a$ and $\hat{\boldsymbol{b}}_2 = -\sin(\theta)\hat{\boldsymbol{i}}_1 + \cos(\theta)\hat{\boldsymbol{i}}_2 \approx \theta\hat{\boldsymbol{i}}_1 + \hat{\boldsymbol{i}}_2$, due to the relationship defined in Equation 3.1. Assuming small θ, we get $\hat{\boldsymbol{b}}_2 \approx \theta\hat{\boldsymbol{i}}_1 + \hat{\boldsymbol{i}}_2$. Combining Equations 3.3 and 3.5 and neglecting higher order terms, we get the value of the kinetic energy to be

$$KE = \frac{1}{2}m\left(\dot{h}^2 + 2bx_\theta\dot{h}\dot{\theta}\right) + \frac{1}{2}\left(I_C + mb^2{x_\theta}^2\right)\dot{\theta}^2. \tag{3.6}$$

Conveniently, the term $(I_C + mb^2{x_\theta}^2)$ is the application of the parallel axis theorem corresponding to the moment of inertia at point P. Therefore, that term will be replaced by I_P going forward. Next, the generalized forces for the airfoil must be calculated for both degrees of freedom with respect to variables h and θ. To find the generalized force, the virtual work done by the aerodynamic lift and pitching moment at point Q must be calculated. First, $\boldsymbol{v}_Q$, the velocity at point Q, is calculated. That will allow us to find the variations in plunge and angular displacements for the virtual work calculations. Similar to $\boldsymbol{v}_P$ found above, total velocity at point Q is obtained by accounting for the inertial and angular contributions of the airfoil motion at point P. This yields

$$\begin{aligned}\boldsymbol{v}_C &= \boldsymbol{v}_P + \dot{\theta}\hat{\boldsymbol{b}}_3 \times \boldsymbol{r}_{PQ} \\ &= \boldsymbol{v}_P + \dot{\theta}\hat{\boldsymbol{b}}_3 \times b\left[(1+a) - \frac{1}{2}\right]\hat{\boldsymbol{b}}_1.\end{aligned} \tag{3.7}$$

Equation 3.7 then simplifies to

$$\boldsymbol{v}_Q = -\dot{h}\hat{\boldsymbol{i}}_2 + b\dot{\theta}\left(\frac{1}{2} + a\right)\hat{\boldsymbol{b}}_2. \tag{3.8}$$

The variation of displacement for point Q is

$$\delta\boldsymbol{p}_Q = -\delta h\hat{\boldsymbol{i}}_2 + b\delta\theta\left(\frac{1}{2} + a\right)\hat{\boldsymbol{b}}_2. \tag{3.9}$$

For the variation in angular displacement, we find that the virtual rotation is simply $\delta\theta\hat{\boldsymbol{b}}_3$ because the angular velocity at point Q is the angular velocity of the

airfoil, which is given by $\dot{\theta}\hat{\boldsymbol{b}}_3$. Now, we can proceed to solve for the virtual work done by the aerodynamic lift and pitching moment. This equation is given by

$$\delta W = L\hat{\boldsymbol{i}}_2 \cdot \delta \boldsymbol{p}_Q + M_{\frac{1}{4}}\hat{\boldsymbol{i}}_3 \cdot \delta\theta\hat{\boldsymbol{b}}_3. \tag{3.10}$$

where L is the aerodynamic lift force at point Q, $M_{\frac{1}{4}}$ is the aerodynamic pitching moment at the quarter-chord location, and $\hat{\boldsymbol{b}}_3 = \hat{\boldsymbol{i}}_3$, as defined previously. The dot products are carried out with the help of Equation 3.1. Using the small θ assumption, the virtual work then becomes

$$\delta W = -L\delta h + \left(M_{\frac{1}{4}} + b\left(\frac{1}{2} + a\right)L\right)\delta\theta. \tag{3.11}$$

Equation 3.11 gives us the generalized forces corresponding to the generalized coordinates $q_1 = h$ and $q_2 = \theta$. These are

$$Q_h = -L \tag{3.12a}$$

$$Q_\theta = M_{\frac{1}{4}} + b\left(\frac{1}{2} + a\right)L. \tag{3.12b}$$

At this point, we have the complete set of equations that are needed to derive the equations of motion for the two degree-of-freedom airfoil. We use Lagrange's equation,

$$\frac{d}{dt}\left(\frac{\partial K}{\partial \dot{q}_i}\right) + \left(\frac{\partial P}{\partial q_i}\right) = Q_i,\ (n = h, \theta), \tag{3.13}$$

substituting in Equations 3.6, 3.2, and 3.12 and performing the following derivatives,

$$\frac{d}{dt}\left(\frac{\partial KE}{\partial \dot{h}}\right) = m\left(\ddot{h} + bx_\theta\ddot{\theta}\right)$$

$$\frac{d}{dt}\left(\frac{\partial KE}{\partial \dot{\theta}}\right) = I_P\ddot{\theta} + mbx_\theta\ddot{h}$$

$$\left(\frac{\partial PE}{\partial h}\right) = k_h h$$

$$\left(\frac{\partial PE}{\partial \theta}\right) = k_\theta\theta.$$

Combining all of the above results, the equations of motion for an undamped two degree-of-freedom airfoil are

$$m\left(\ddot{h}+bx_\theta\ddot{\theta}\right)+k_h h=-L \tag{3.14a}$$

$$I_P\ddot{\theta}+mbx_\theta\ddot{h}+k_\theta\theta=M_{\frac{1}{4}}+b\left(\frac{1}{2}+a\right)L. \tag{3.14b}$$

We can transform Equation 3.14 into matrix form as

$$\begin{bmatrix} m & mbx_\theta \\ mbx_\theta & I_P \end{bmatrix}\begin{bmatrix} \ddot{h} \\ \ddot{\theta} \end{bmatrix}+\begin{bmatrix} k_h & 0 \\ 0 & k_\theta \end{bmatrix}\begin{bmatrix} h \\ \theta \end{bmatrix}=\begin{bmatrix} -L \\ M_{\frac{1}{4}}+b\left(\frac{1}{2}+a\right)L \end{bmatrix}\equiv\begin{bmatrix} Q_h \\ Q_\theta \end{bmatrix}. \tag{3.15}$$

The matrix representation will be used for the dynamical analysis of the system.

3.2 Aerodynamics Model

Several types of unsteady aerodynamics models exist, with the most popular unsteady model in the literature being the Theodorsen's unsteady equations for lift and moment on a flat plate airfoil, or some variations of these equations. Theodorsen's unsteady model makes several strong assumptions, one of them being that the unsteady motion is entirely oscillatory in nature. Furthermore, the major challenge with the use of Theodorsen's unsteady equations is that the equations are in the frequency domain. Thus, several sophisticated approximations and transformations are necessary to represent the unsteady equations in the time domain [65, 103]. This transformation into the time domain also requires experimentally obtaining some of the coefficients in the unsteady equations. Many of the approximations also result in lengthy integro-differential equations with complicated coefficients that are difficult to interpret physically. Thus, the validity of these aerodynamic models is limited to how accurately the aeroelastic analysis predicts the dynamic behavior of the airfoil when compared with results from lab testing.

This thesis will focus on using a new type of incompressible unsteady aero-

dynamics model for free play analysis. Peters [103] provides an excellent historical overview of the development of the unsteady theories that deal with two-dimensional, incompressible flow. While several choices are available for use in this thesis, the unsteady model selected is a finite-state, induced-flow model that was introduced in 1995 by Peters et al. [104]. The theory is based on the idealization of an induced flow field near the airfoil resulting from the interactions of shed vortices with arbitrary airfoil motion. The advantage of using this model is that it is strictly derived in the time domain using first principles of fluid mechanics, thus avoiding the difficulties of transformation from the frequency domain. This newer unsteady, aerodynamics model has been shown to yield results comparable to those of classical unsteady aerodynamics models [19]. The use of this generalized finite-state, induced-flow model would be a first in the area of free play analysis.

3.2.1 Background

Two-dimensional, finite-state unsteady induced flow theory is very similar to the two-dimensional Theodorsen's unsteady flow theory. There are several ways to arrive at the unsteady aerodynamics equations. However, we will show the derivation to be an equivalent form of the unsteady Theodorsen's unsteady equations with special conditions. Hence, Theodorsen's unsteady equations and Theodorsen's function, $C(k)$, which is a complex number, must first be understood at a qualitative level. Theodorsen's unsteady equations corresponding to the airfoil selected in this paper are [19]

$$L = 2\pi\rho_\infty UbC(k)\left[\dot{h} + U\theta + b\left(\frac{1}{2} - a\right)\dot{\theta}\right] + \pi\rho_\infty b^2\left(\ddot{h} + U\dot{\theta} - ba\ddot{\theta}\right) \tag{3.16a}$$

$$M_{\frac{1}{4}} = -\pi\rho_\infty b^3\left[\frac{1}{2}\ddot{h} + U\dot{\theta} + b\left(\frac{1}{8} - \frac{a}{2}\right)\ddot{\theta}\right], \tag{3.16b}$$

where the Theodorsen's function is

$$C(k) = \frac{H_1^{(2)}(k)}{H_1^{(2)}(k) + iH_0^{(2)}(k)}. \tag{3.17}$$

The variables θ and h are the same as the variables used for the structural model shown in Figure 3.1. In Equation 3.17, $H_1^{(2)}(k)$ and $H_0^{(2)}(k)$ are Hankel's functions of the second kind, $k = \omega b/U$ is reduced (non-dimensional) frequency, and $i = \sqrt{-1}$. Before the importance of Theodorsen's function is explained, unsteady flow must be understood qualitatively as well.

Unsteady flow, in general, is assumed to consist of circulatory and non-circulatory parts. Lift contributions from circulatory flow, defined as circulatory lift, is the lift resulting from bound circulation on the airfoil. Non-circulatory flow, on the other hand, captures the effects of apparent mass and apparent inertia on the airfoil, represented by the flow acceleration terms. With these definitions, we find that in Equations 3.16 the circulatory terms are only observed in the aerodynamic lift force L. In particular, this circulatory part of the unsteady lift is given by

$$2\pi\rho_\infty UbC(k)\left[\dot{h} + U\theta + b\left(\frac{1}{2} - a\right)\dot{\theta}\right].$$

This circulatory part in the unsteady lift contains two important quantities: the "effective angle of attack" between the airfoil and unsteady flow, represented by the variable α, defined below, and Theodorsen's function $C(k)$. The effective angle of attack,

$$\alpha = \left[\frac{\dot{h}}{U} + \theta + \frac{b}{U}\left(\frac{1}{2} - a\right)\dot{\theta}\right], \tag{3.18}$$

represents the relative airflow that the airfoil "feels" when present in unsteady flow. Not only does this value depend on the instantaneous pitch angle θ, but also plunge velocity $\dot{h}$ and angular velocity of the airfoil $\dot{\theta}$. The value of effective angle of attack involves first order terms due to the fact that flow direction varies along the chord of the airfoil, resulting in variation in lift throughout the airfoil motion at different instants of time. Furthermore, the lift response and magnitude are not always propor-

tional to the effective angle of attack. Instead, unsteady motion can induce a phase lag in the airfoil response and a reduction in total lift. Both of these phenomena, which are experimentally observed, are captured in the lift equation by multiplying the effective angle of attack by Theodorsen's function $C(k)$ [66].

Theodorsen's function, shown in Figure 3.2, is a complex function of reduced frequency k. Starting with $k = 0$, we find that $C(0) = 1$ from the definition in Equation 3.17. $C(k)$ is a complex number with real value $\mathrm{Re}[C(k)]$, which reduces for increasing k, while the imaginary part $\mathrm{Im}[C(k)]$ varies as shown in Figure 3.2. Physically, the phase lag in the lift response, ϕ, is interpreted from Theodorsen's function as $\phi = \arctan(\frac{\mathrm{Im}[C(k)]}{\mathrm{Re}[C(k)]})$; the real part of Theodorsen's function is used in the circulatory part of the unsteady lift.

In practical cases, the reduced frequency k rarely exceeds a value of 1, even for highly unsteady flow. In particular, for the case of slowly varying arbitrary airflow motion, *quasi-steady aerodynamics* assumptions can be made, where k is assumed to be in the range $0 \leq k \leq 0.05$ [105]. For quasi-steady flow, the approximation $C(k) = 1$ is made, where the phase lag by the definition above becomes $\phi = \frac{\pi}{2}$. The quasi-steady assumption is often a good and valid assumption for aircraft flying in high-altitude cruise conditions. At this point, we are ready to explore the finite-state, unsteady induced flow theory.

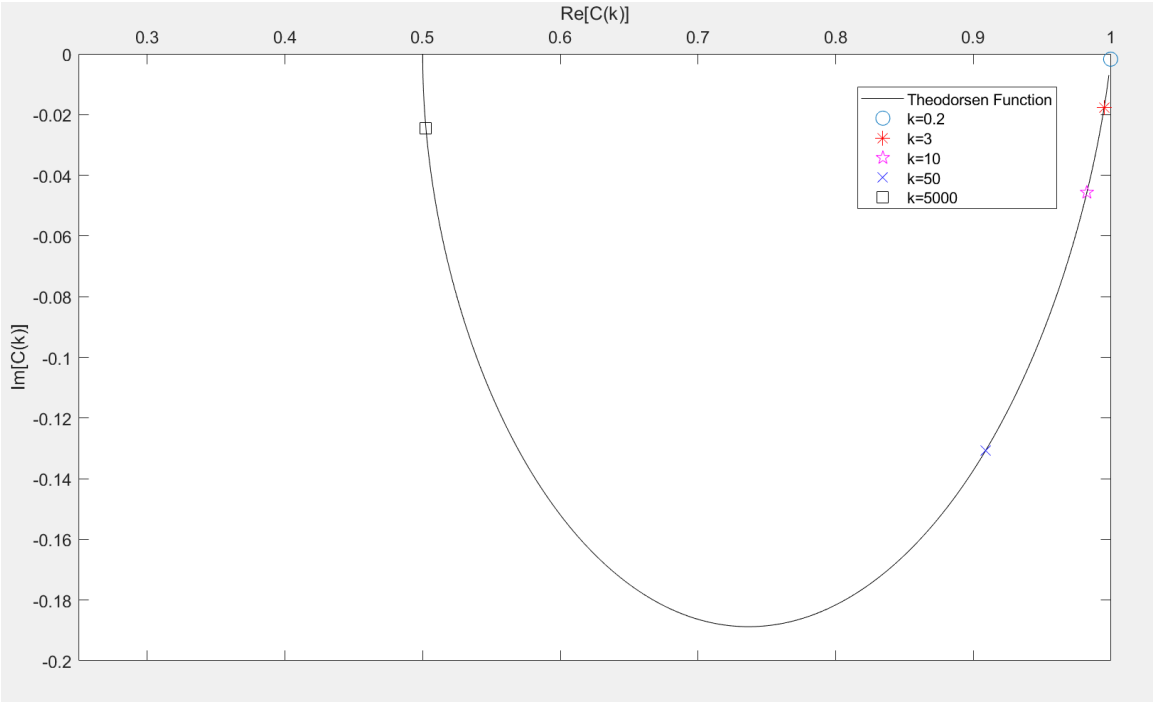

Figure 3.2: Theodorsen's function contains only positive real parts and negative imaginary parts. As the reduced frequency k approaches infinity, the function approaches a limiting real value of 0.5 with no imaginary component, as seen at the left side of the curve. The right endpoint of the curve approaches a limiting real value of 1 (no imaginary components) when $k = 0$.

3.2.2 Finite-State, Induced-Flow Theory

The induced flow model by Peters et al. [104] is a finite-state, time domain representation of unsteady aerodynamics that is derived analytically by using first principles in fluid mechanics. In this thesis, we will show that it is possible, to an extent, to derive the unsteady equations of Peters [103] directly from Theodorsen's unsteady equations discussed above.

Starting with Equations 3.16, we assume that the flow is incompressible and inviscid and will remain that way. Imposing the conservation laws of mass and momentum in the flow field around the airfoil, we can show that the non-circulatory, inertial terms from the Theodorsen's unsteady equations remain the same as in the Peters et al. [103] model, regardless of variations in the flow field around the airfoil resulting

from induced flow. The major difference in the models come from how the circulatory lift is defined. First, the finite-state, induced-flow theory assumes quasi-steady flow, and so $C(k) = 1$. Secondly, when induced-flow is considered for an arbitrarily moving airfoil, the flow field near the airfoil is altered, thus changing the airfoil's effective angle of attack. A derivation of the effective angle of attack for this new aerodynamics model is provided below, as well as a discussion about induced flow. Ultimately, the new unsteady equations are derived.

We begin by introducing the variable λ_0 as the average velocity of the induced flow field around the airfoil acting in the perpendicular downwards direction relative to the chordline of the airfoil. An induced flow field around an airfoil is the downwash due to shed vorticity that is produced as air deflects off of the airfoil. The induced flow field vary along the length of the chord of the airfoil and λ_0 provides its average value approximation at the three-quarter chord location (point T in Figure 3.1). According to classical thin-airfoil theory convention, the three-quarter chord location is the where angle of attack for an airfoil is calculated. Henceforth, all of the derivations for the effective angle of attack will be done with respect to the three-quarters chord location on the airfoil.

The effective angle of attack, α, is found by calculating the angle between the airfoil chordline and the relative wind velocity direction that the airfoil encounters. Relative wind is thought of as the velocity that the airfoil "feels" with respect to the induced flow field near the airfoil. By definition, it is the difference between the airfoil motion and the relative velocity field near the airfoil with induced flow. Visually, this phenomena can be seen in Figure 3.3, where the relative wind velocity is a vector that points in the $\hat{\boldsymbol{a}}_1$ direction in the local relative wind coordinate system. The effective angle of attack is also shown in the diagram with its relationship to the direction of the chordline, $\hat{\boldsymbol{b}}_1$.

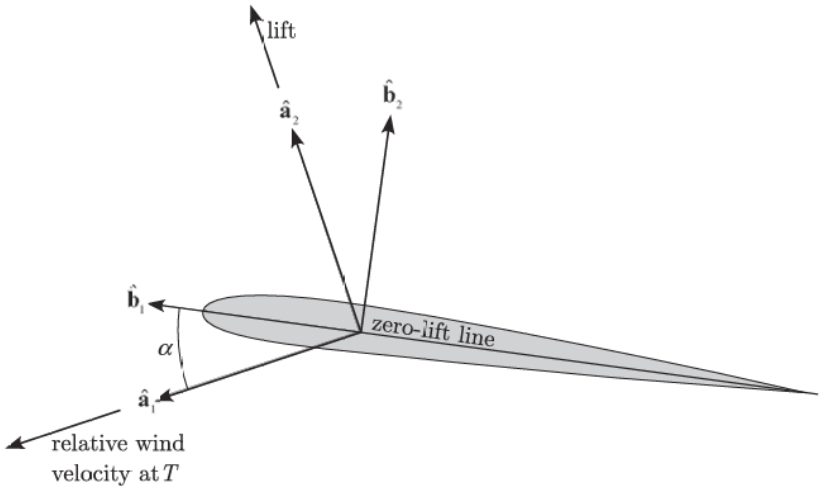

Figure 3.3: Relative wind is the instantaneous velocity of the airfoil with respect to unsteady flow that has been induced near the airfoil [19].

The local relative wind coordinate system is related to the local airfoil coordinate system by a counterclockwise rotation of α about $\hat{\boldsymbol{a}}_3 = \hat{\boldsymbol{i}}_3 = \hat{\boldsymbol{b}}_1 \times \hat{\boldsymbol{b}}_2$. This relationship is defined by

$$\begin{Bmatrix} \hat{\boldsymbol{a}}_1 \\ \hat{\boldsymbol{a}}_2 \end{Bmatrix} = \begin{bmatrix} \cos(\alpha) & -\sin(\alpha) \\ \sin(\alpha) & \cos(\alpha) \end{bmatrix} \begin{Bmatrix} \hat{\boldsymbol{b}}_1 \\ \hat{\boldsymbol{b}}_2 \end{Bmatrix}. \tag{3.19}$$

Keep in mind that the local airfoil coordinate system is related to the global Cartesian coordinate system by Equation 3.1. We rewrite the relationship as

$$\begin{Bmatrix} \hat{\boldsymbol{i}}_1 \\ \hat{\boldsymbol{i}}_2 \end{Bmatrix} = \begin{bmatrix} \cos(\theta) & -\sin(\theta) \\ \sin(\theta) & \cos(\theta) \end{bmatrix} \begin{Bmatrix} \hat{\boldsymbol{b}}_1 \\ \hat{\boldsymbol{b}}_2 \end{Bmatrix}. \tag{3.20}$$

We are ready to derive the instantaneous relative wind velocity vector using the appropriate vector notation. As mentioned earlier, it is defined in vector space as the difference between the airfoil motion and the relative velocity field near the airfoil with induced flow. Calculating the velocities at the three-quarter chord location (point T in Figure 3.1), the instantaneous relative wind vector, with magnitude W, is given by

$$W\hat{\boldsymbol{a}}_1 = \boldsymbol{v}_T - \left(-U\hat{\boldsymbol{i}}_1 - \lambda_0\hat{\boldsymbol{b}}_2\right), \tag{3.21}$$

where the airfoil velocity at three-quarter chord (point T), is given by

$$\boldsymbol{v}_T = \boldsymbol{v}_P + \dot{\theta}\hat{\boldsymbol{b}}_3 \times \boldsymbol{r}_{PT}, \tag{3.22}$$

and $\boldsymbol{r}_{PT}$ is the position vector from point P to point T given by

$$\begin{aligned} \boldsymbol{r}_{PT} &= \left[\frac{b}{2} + (1+a)\,b - 2b\right]\hat{\boldsymbol{b}}_1 \\ &= b\left(a - \frac{1}{2}\right)\hat{\boldsymbol{b}}_1. \end{aligned} \tag{3.23}$$

Collecting all the terms into Equation 3.21, we find

$$W\hat{\boldsymbol{a}}_1 = U\hat{\boldsymbol{i}}_1 - \dot{h}\hat{\boldsymbol{i}}_2 + \left[b\dot{\theta}\left(a - \frac{1}{2}\right) - \lambda_0\right]\hat{\boldsymbol{b}}_2. \tag{3.24}$$

Applying the small θ approximation and using the relationships in Equations 3.19 and 3.20, we can rewrite Equation 3.24 in terms of the local airfoil coordinates, $\hat{\boldsymbol{b}}_1$ and $\hat{\boldsymbol{b}}_2$,

$$W\hat{\boldsymbol{a}}_1 = (U - \dot{h}\theta)\hat{\boldsymbol{b}}_1 + \left(-U\theta - \dot{h} + b\dot{\theta}\left(a - \frac{1}{2}\right) + \lambda_0\right)\hat{\boldsymbol{b}}_2. \tag{3.25}$$

We can approximate $U - \dot{h}\theta \approx U$ because $\dot{h}\theta$ is a nonlinear, higher-order term that can be assumed to be $\dot{h}\theta << U$. Physically, this assumptions is interpreted as the magnitudes of the airfoil motion being significantly less than the aircraft speed.

We can also decompose the wind vector on the left-hand side of Equation 3.25 into its trigonometric relationships,

$$W\hat{\boldsymbol{a}}_1 = W\cos(\alpha)\hat{\boldsymbol{b}}_1 - W\sin(\alpha)\hat{\boldsymbol{b}}_2. \tag{3.26}$$

Here, we can assume small α and can normalize the magnitude of the wind vector by dividing all terms by U, giving us

$$\frac{W}{U}\hat{\boldsymbol{a}}_1 = \frac{W}{U}\hat{\boldsymbol{b}}_1 - \frac{W}{U}\alpha\hat{\boldsymbol{b}}_2. \tag{3.27}$$

Equation 3.27 then becomes

$$\frac{W}{U}\hat{\boldsymbol{a}}_1 = (1)\hat{\boldsymbol{b}}_1 + \left(-\theta - \frac{\dot{h}}{U} + \frac{b\dot{\theta}}{U}\left(a - \frac{1}{2}\right) + \frac{\lambda_0}{U}\right)\hat{\boldsymbol{b}}_2. \tag{3.28}$$

From Equation 3.27 and 3.28, we can see that the effective angle of attack for

induced-flow, unsteady aerodynamics is

$$\alpha = \left[\theta + \frac{\dot{h}}{U} + \frac{b}{U}\left(\frac{1}{2} - a\right)\dot{\theta} - \frac{\lambda_0}{U}\right]. \tag{3.29}$$

Equation 3.29 now replaces the effective angle of attack in the circulatory lift of Theodorsen's unsteady equations. Finally, we arrive at the unsteady finite-state, induced flow equations for lift and pitching moment,

$$L = 2\pi\rho_\infty U b\left[\dot{h} + U\theta + b\left(\frac{1}{2} - a\right)\dot{\theta} + \lambda_0\right] + \pi\rho_\infty b^2\left(\ddot{h} + U\dot{\theta} - ba\ddot{\theta}\right) \tag{3.30a}$$

$$M_{\frac{1}{4}} = -\pi\rho_\infty b^3\left[\frac{1}{2}\ddot{h} + U\dot{\theta} + b\left(\frac{1}{8} - \frac{a}{2}\right)\ddot{\theta}\right]. \tag{3.30b}$$

This equation is coupled with the structural equations to complete the aeroelastic equations of motion for our model.

This model, however, is not complete. In Equations 3.30, there is the additional unknown λ_0 term, which is the approximated average induced flow velocity at the three-quarter chord point. Peters et al. [103] resolve this issue by showing that the induced flow can be represented in terms of the variables of airfoil motion. Specifically,

$$\lambda_0 \approx \frac{1}{2}\sum_{n=1}^{N} b_n \lambda_n, \tag{3.31}$$

where N is the number of user-defined finite induced flow states $\lambda_1,\ \lambda_2, \ldots, \lambda_N$. These states represent velocity coefficients of induced flow fields as opposed to velocities at discrete points on or near the airfoil. These states are hierarchical, requiring only a few number of states to be chosen for the aeroelastic analysis to yield accurate results. More detailed discussion is found in [104]. In that reference, it is stated that an optimal selection for N is between four and nine induced flow states to obtain results that are consistent with established theories in the field. Choosing a too large N can lead to ill-conditioning and result in degraded accuracy in the model.

In Equation 3.31, b_n are weighted averaging constants whose sum is constrained to being 1 due to how this theory is developed by Peters [103]. The least-squares

approximation of b_n, given by

$$b_n = \begin{cases} (-1)^{n-1} \frac{(N+n-1)!}{(N-n-1)!} \frac{1}{(n!)^2} & n \neq N \\ (-1)^{n-1} & n = N, \end{cases} \tag{3.32}$$

is used for this thesis due its higher accuracy for the large time scales that we use in our time-domain analysis. We can let $\{\lambda\}$ be an $N \times 1$ column matrix that contains the values of λ_n. Hodges and Pierce [19] show that the induced flow dynamics for the Peters et al. model is governed by the following set of N first-order differential equations,

$$[A]\{\dot{\lambda}\} + \frac{U}{b}\{\lambda\} = \{c\}\left[\ddot{h} + U\dot{\theta} + b\left(\frac{1}{2} - a\right)\ddot{\theta}\right]. \tag{3.33}$$

$[A]$ and $\{c\}$ are coefficient matrices that are found based on following relationships, given N user-defined induced-flow states:

$$[A] = [D] + \{d\}\{b\}^T + \{c\}\{d\}^T + \frac{1}{2}\{c\}\{b\}^T, \tag{3.34}$$

where b_n are defined above, and,

$$D_{nm} = \begin{cases} \frac{1}{2n} & n = m + 1 \\ -\frac{1}{2n} & n = m - 1 \\ 0 & n \neq m \pm 1 \end{cases} \tag{3.35a}$$

$$d_n = \begin{cases} \frac{1}{2} & n = 1 \\ 0 & n \neq 1, \end{cases} \tag{3.35b}$$

and

$$c_n = \frac{2}{n}. \tag{3.35c}$$

See references [103, 104] for more details on the specifics of this model.

Equations 3.31 and 3.34 give the relationships necessary to relate λ_0 to the variables of the structural model that describes the airfoil motion. At this point, we are ready to synthesize a full state-space representation of the aeroelastic model.

3.3 State-Space Representation

Establishing a state-space model for the equations of motion of the entire system allows us to perform dynamical analyses in the time domain. First, consider Equation 3.15. The 2×2 matrices on the left side of the equation and the vector on the right side can be replaced by short-form matrices as

$$\left[M_{struct}\right]\begin{bmatrix}\ddot{h}\\ \ddot{\theta}\end{bmatrix} + \left[K_{struct}\right]\begin{bmatrix}h\\ \theta\end{bmatrix} = \begin{bmatrix}-L\\ M_{\frac{1}{4}} + b\left(\frac{1}{2}+a\right)L\end{bmatrix} \equiv \left\{F_{aero}\right\}. \tag{3.36}$$

We can input Equations 3.30 into the right side of this equation to find

$$\begin{aligned} -L = &-\pi\rho_\infty b^2\ddot{h} + \pi\rho_\infty b^3 a\ddot{\theta} - 2\pi\rho_\infty U b\dot{h} + \pi\rho_\infty U b^2(2a-2)\dot{\theta} \\ &- 2\pi\rho_\infty U^2 b\theta + 2\pi\rho_\infty U b\lambda_0 \end{aligned} \tag{3.37a}$$

$$\begin{aligned} M_{\frac{1}{4}} + b\left(\frac{1}{2}+a\right)L = &\pi\rho_\infty b^3 a\ddot{h} - \pi\rho_\infty b^4\left(\frac{1}{8}+a^2\right)\ddot{\theta} + \pi\rho_\infty U b^2(1+2a)\dot{h} \\ &+ \pi\rho_\infty U b^3\left(a-2a^2\right)\dot{\theta} + \pi\rho_\infty U^2 b^2(1+2a)\theta \\ &- \pi\rho_\infty U b^2(1+2a)\lambda_0. \end{aligned} \tag{3.37b}$$

These equations can be put into matrix form as

$$\begin{aligned} \left\{F_{aero}\right\} = &\begin{bmatrix}-\pi\rho_\infty b^2 & \pi\rho_\infty b^3 a\\ \pi\rho_\infty b^3 a & -\pi\rho_\infty b^4\left(\frac{1}{8}+a^2\right)\end{bmatrix}\begin{bmatrix}\ddot{h}\\ \ddot{\theta}\end{bmatrix} \\ &+ \begin{bmatrix}-2\pi\rho_\infty U b & \pi\rho_\infty U b^2(2a-2)\\ \pi\rho_\infty U b^2(1+2a) & \pi\rho_\infty U b^3(a-2a^2)\end{bmatrix}\begin{bmatrix}\dot{h}\\ \dot{\theta}\end{bmatrix} \\ &+ \begin{bmatrix}0 & -2\pi\rho_\infty U^2 b\\ 0 & \pi\rho_\infty U^2 b^2(1+2a)\end{bmatrix}\begin{bmatrix}h\\ \theta\end{bmatrix} + \begin{bmatrix}2\pi\rho_\infty U b\\ -\pi\rho_\infty U b^2(1+2a)\end{bmatrix}\left[\lambda_0\right]. \end{aligned} \tag{3.38}$$

Just like Equation 3.36, we can rewrite Equation 3.38 in short-form as

$$\left\{F_{aero}\right\} = \left[M_{aero}\right]\begin{bmatrix}\ddot{h}\\ \ddot{\theta}\end{bmatrix} + \left[B_{aero}\right]\begin{bmatrix}\dot{h}\\ \dot{\theta}\end{bmatrix} + \left[K_{aero}\right]\begin{bmatrix}h\\ \theta\end{bmatrix} + \left[P_{aero}\right]\left[\lambda_0\right]. \tag{3.39}$$

We can combine Equations 3.36 and 3.39, and rearrange matrices corresponding to like variable vectors, and obtain

$$\left[M_{struct} - M_{aero}\right] \begin{bmatrix} \ddot{h} \\ \ddot{\theta} \end{bmatrix} = \left[K_{aero} - K_{struct}\right] \begin{bmatrix} h \\ \theta \end{bmatrix} + \left[B_{aero}\right] \begin{bmatrix} \dot{h} \\ \dot{\theta} \end{bmatrix} + \left[P_{aero}\right] \left[\lambda_0\right], \tag{3.40}$$

where

$$\left[M_{struc} - M_{aero}\right] = \begin{bmatrix} m + \pi\rho_\infty b^2 & mbx_\theta - \pi\rho_\infty b^3 a \\ mbx_\theta - \pi\rho_\infty b^3 a & I_P + \pi\rho_\infty b^4 \left(\frac{1}{8} + a^2\right) \end{bmatrix} \tag{3.41a}$$

$$\left[K_{aero} - K_{struc}\right] = \begin{bmatrix} -k_h & -2\pi\rho_\infty U^2 b \\ 0 & -k_\theta + \pi\rho_\infty U^2 b^2 \left(1 + 2a\right) \end{bmatrix}. \tag{3.41b}$$

For sake of brevity and simpler notation, we will rename Equations 3.41a and 3.41b as $\left[M_{sys}\right]$ and $\left[K_{sys}\right]$, respectively.

Equation 3.40 must now be transformed into a non-dimensional form so that the numerical results from this model can be physically interpreted for any general case. The non-dimensional parameters that will be used are listed Table 3.1. These parameters were found in [19, 106]

Non-dimensional (N.D.) Parameter	**Proportionality Relationship**
N.D. Plunging Variable ($\bar{h}$)	$\bar{h} = \frac{h}{b}$
N.D. Pitching Variable ($\bar{\theta}$)	$\bar{\theta} = \theta$
N.D. Induced Airflow Velocity ($\bar{\lambda}_0$)	$\bar{\lambda}_0 = \frac{\lambda_0}{U}$
N.D. Frequency Ratio (σ)	$\sigma = \frac{\omega_h}{\omega_\theta}$
N.D. Mass Ratio Parameter (μ)	$\mu = \frac{m}{\pi \rho_\infty b^2}$
N.D. Radius of Gyration (r^2)	$r^2 = \frac{I_P}{mb^2}$
N.D. Freestream Velocity (V)	$V = \frac{m}{b^2 \omega_\theta}$
N.D. Time (τ)	$\tau = \omega t,\ \frac{d}{dt} = \omega \frac{d}{d\tau},\ \frac{d^2}{dt^2} = \omega^2 \frac{d^2}{d\tau^2}$

Table 3.1: Table of non-dimensional parameters and proportionality relationships.

To correctly transform the entire system of equations into non-dimensional form, the first rows in the matrices of Equation 3.40 must initially be multiplied by b. Then the entire system of equations are divided by mU^2. Upon doing this step, the variables of airfoil motion, h and θ, and their derivatives are replaced by their proportional non-dimensional parameter equivalencies. Finally, all of the terms in the equations are grouped in a manner to yield only non-dimensional terms for

our dynamical equations of motion. These manipulated matrices, shown below with asterisk superscripts, thus become non-dimensional,

$$\left[M^*{}_{sys}\right] = \left(\frac{1}{\mu V^2}\right)\begin{bmatrix} \mu+1 & \mu x_\theta - a \\ \mu x_\theta - a & \mu r^2 + \left(\frac{1}{8} + a^2\right) \end{bmatrix} \tag{3.42a}$$

$$\left[B^*{}_{aero}\right] = \left(\frac{1}{\mu V^2}\right)\begin{bmatrix} -2V & (2a-2)V \\ (1+2a)V & (a-2a^2)V \end{bmatrix} \tag{3.42b}$$

$$\left[K^*{}_{sys}\right] = \left(\frac{1}{\mu V^2}\right)\begin{bmatrix} -\mu\sigma^2 & -2V^2 \\ 0 & -\mu r^2 + V^2\left(1+2a\right) \end{bmatrix} \tag{3.42c}$$

$$\left[P^*{}_{aero}\right] = \left(\frac{1}{\mu V^2}\right)\begin{bmatrix} 2V^2 \\ -\left(1+2a\right)V^2 \end{bmatrix}. \tag{3.42d}$$

The common term of $1/\mu V^2$ can be divided out of Equation 3.40 since it appears on both sides of the equation.

To perform time domain analyses, the equations of motion have to be put into state space form. Before state variables are introduced, Equation 3.40 must be put into standard form. This is done by multiplying both sides of the equation by the inverse of matrix $\left[M^*{}_{sys}\right]$ to get

$$\begin{bmatrix} \bar{h}'' \\ \bar{\theta}'' \end{bmatrix} = \left[M^*{}_{sys}\right]^{-1}\left[K^*{}_{sys}\right]\begin{bmatrix} \bar{h} \\ \bar{\theta} \end{bmatrix} + \left[M^*{}_{sys}\right]^{-1}\left[B^*{}_{aero}\right]\begin{bmatrix} \bar{h}' \\ \bar{\theta}' \end{bmatrix} + \left[M^*{}_{sys}\right]^{-1}\left[P^*{}_{aero}\right]\left[\bar{\lambda}_0\right], \tag{3.43}$$

where

$$\left[M^*{}_{sys}\right]^{-1} = \left(\frac{1}{(\det M^*{}_{sys})}\right)\begin{bmatrix} \mu r^2 + \left(\frac{1}{8} + a^2\right) & -\mu x_\theta + a \\ -\mu x_\theta + a & \mu + 1 \end{bmatrix}, \tag{3.44}$$

and

$$\det M^*{}_{sys} = \mu^2\left(r^2 - {x_\theta}^2\right) + \mu\left(r^2 + a^2 + 2ax_\theta + \frac{1}{8}\right) + \frac{1}{8}.$$

The primes on the non-dimensional variables $\bar{h}$ and $\bar{\theta}$ in Equation 3.43 denote non-

dimensional time derivatives. Also, once again for the sake of brevity and simpler notation, we define

$$\left[\ E\ \right] = \left[M^*{}_{sys}\right]^{-1}\left[K^*{}_{sys}\right] \tag{3.45a}$$

$$\left[\ F\ \right] = \left[M^*{}_{sys}\right]^{-1}\left[B^*{}_{aero}\right] \tag{3.45b}$$

$$\left[\ G\ \right] = \left[M^*{}_{sys}\right]^{-1}\left[P^*{}_{aero}\right]. \tag{3.45c}$$

The final steps before we can continue into state vector formulation is to relate the variable $\bar{\lambda}_0$ in Equation 3.43 back to the non-dimensional system variables of pitch and plunge. This is achieved by transforming Equations 3.31-3.35 into non-dimensional form using the transformations of Table 3.1. The first relation we get is

$$\bar{\lambda}_0 \approx \frac{1}{2}\sum_{n=1}^{N} b_n \bar{\lambda}_n, \tag{3.46}$$

where b_n remains the same as in Equation 3.32. When this equation is substituted into Equation 3.43, the 2×1 matrix $\left[\ G\ \right]$ transforms into the following $2\times N$ matrix,

$$\left[\ \bar{G}\ \right] = \left[M^*{}_{sys}\right]^{-1}\begin{bmatrix} b_1 V & -(0.5+a)b_1 V \\ b_2 V & -(0.5+a)b_2 V \\ \vdots & \vdots \\ b_N V & -(0.5+a)b_N V \end{bmatrix}^T. \tag{3.47}$$

Additionally, the variable $\left[\bar{\lambda}_0\right]$ in Equation 3.43 is replaced by the $N \times 1$ vector $\left[\ \bar{\lambda}_1,\ \bar{\lambda}_2, \ldots,\ \bar{\lambda}_N\right]^T$.

Finally, the dimensionless form of Equation 3.33 is derived by dividing both sides of the equation by ${\omega_\theta}^2 b$, yielding

$$[A]\left\{\bar{\lambda}'\right\} + V\{\bar{\lambda}\} = \{c\}\left[\bar{h}'' + V\bar{\theta}' + \left(\frac{1}{2} - a\right)\bar{\theta}''\right], \tag{3.48}$$

where $\{\bar{\lambda}\}$ is the vector of N non-dimensional induced flow states $\bar{\lambda}_n$. The above equation must be put into standard form for it to be solvable using a state-space

model. Both sides of Equation 3.48 must be left multiplied by $[A]^{-1}$, followed by isolating highest order differential variables to one side of the equation. This yields

$$\{\bar{\lambda}'\} = -V\,[A]^{-1}\,\{\bar{\lambda}\} + [A]^{-1}\,\{c\}\left[\bar{h}'' + V\bar{\theta}' + \left(\frac{1}{2} - a\right)\bar{\theta}''\right]. \tag{3.49}$$

At this point, we are ready to introduce the state variables. Let

$$[x_1,\ x_2,\ x_3,\ x_4,\ x_5,\ x_6, \ldots,\ x_N]^T = \left[\bar{h},\ \bar{\theta},\ \bar{h}',\ \bar{\theta}',\ \bar{\lambda}_1,\ \bar{\lambda}_2, \ldots,\ \bar{\lambda}_N\right]^T. \tag{3.50}$$

Then,

$$[\dot{x_1},\ \dot{x_2},\ \dot{x_3},\ \dot{x_4},\ \dot{x_5},\ \dot{x_6}, \ldots,\ \dot{x_N}]^T = \left[\bar{h}',\ \bar{\theta}',\ \bar{h}'',\ \bar{\theta}'',\ \bar{\lambda}_1',\ \bar{\lambda}_2', \ldots,\ \bar{\lambda}_N'\right]^T.$$

Using the newly introduced state variables, we can express our system of two second-order differential equations in Equation 3.43 as a system of $N+4$ first-order differential equations, given by

$$\begin{bmatrix} \dot{x}_1 \\ \dot{x}_2 \\ \dot{x}_3 \\ \dot{x}_4 \\ \dot{x}_5 \\ \dot{x}_6 \\ \vdots \\ \dot{x}_N \end{bmatrix} = \left[\begin{array}{cccc:ccc} 0 & 0 & 1 & 0 & 0 & 0 & \ldots & 0 \\ 0 & 0 & 0 & 1 & 0 & 0 & \ldots & 0 \\ \hdashline \multicolumn{2}{c}{\left[\ E\ \right]} & \multicolumn{2}{c:}{\left[\ F\ \right]} & \multicolumn{3}{c}{\left[\ \bar{G}\ \right]} \\ \hdashline \multicolumn{4}{c:}{} & \multicolumn{3}{c}{} \\ \multicolumn{4}{c:}{\left[\ R_{sys}\ \right]} & \multicolumn{3}{c}{\left[\ R_{aero}\ \right]} \\ \multicolumn{4}{c:}{} & \multicolumn{3}{c}{} \end{array}\right] \begin{bmatrix} x_1 \\ x_2 \\ x_3 \\ x_4 \\ x_5 \\ x_6 \\ \vdots \\ x_N \end{bmatrix}. \tag{3.51}$$

In Equation 3.51,

$$\left[\ R_{sys}\ \right] = \left[\ A\ \right]^{-1} \left\{\ c\ \right\} \begin{bmatrix} E(1,1) + (0.5-a)E(2,1) \\ E(1,2) + (0.5-a)E(2,2) \\ F(1,1) + (0.5-a)F(2,1) \\ F(1,2) + (0.5-a)F(2,2) + V \end{bmatrix}^T \tag{3.52}$$

$$\left[R_{aero} \right] = \left[A \right]^{-1} \left\{ c \right\} \begin{bmatrix} \bar{G}(1,1) + (0.5-a)\bar{G}(2,1) \\ \bar{G}(1,2) + (0.5-a)\bar{G}(2,2) \\ \vdots \\ \bar{G}(1,N) + (0.5-a)\bar{G}(2,N) \end{bmatrix}^T - V \left[A \right]^{-1}, \quad (3.53)$$

where the matrices are size $N \times 4$ and $N \times N$, respectively.

3.4 Nonlinear Modeling

There are several mathematical representations of the free play nonlinearity in pitch, as discussed in Section 2.2. The two models that are examined in this thesis are the piecewise and cubic representations of free play.

Recall, we define the system's pitch stiffness to be equal to $k_\theta M(\theta)$, where k_θ is an arbitrary stiffness constant and $M(\theta)$ is a mathematical function of pitch that determines the pitching nonlinearity. If the system has linear stiffness, then the stiffness will obey Hooke's Law and $M(\theta) = \theta$. However, for the piecewise and cubic free play models, we define their mathematical representation by

$$M(\theta) = (\theta + \delta) - (\theta + \delta)\, H\,(t + \delta) + (\theta - \delta)\, H\,(t - \delta) \quad (3.54)$$

and

$$M(\theta) = C_1\theta + C_3\theta^3, \quad (3.55)$$

respectively. In Equation 3.54, H is the Heaviside function that turns the stiffness "on" and "off" around the bounds of the free play amount that is given the variable δ. While this mathematical form is slightly different from the one given in Equation 2.17, both equations are identical. In Equation 3.55, C_1 and C_3 are scaling parameters that provide the best fit cubic approximation to the piecewise model of free play. The choice of constants for C_1 and C_3 depends largely on the domain within which the piecewise model is valid. For a domain of best fit with a large range, the cubic model

would more closely match the linear subdomains as opposed to the flat spot of free play, resulting in weak nonlinearities. Selecting a domain that is too small would result in the best fit approximation giving good match to the flat spot subdomain but poorly resembling the linear subdomains, resulting in strongly cubic nonlinearities. Through trial and error, the domain of best fit for the cubic model was selected to be between $-3^\circ \leq \alpha \leq 3^\circ$, where the best fit approximations struck a good balance between the flat spot and linear subdomains.

Now that we have defined the nonlinearities, we will derive the nonlinear form of the state-space model shown in the previous section. The derivation provided works for both free play models. The first step is to rewrite the original equations of motion given in Equations 3.36 as

$$\begin{bmatrix} m & mbx_\theta \\ mbx_\theta & I_P \end{bmatrix} \begin{bmatrix} \ddot{h} \\ \ddot{\theta} \end{bmatrix} + \begin{bmatrix} k_h & 0 \\ 0 & k_\theta \end{bmatrix} \begin{bmatrix} h \\ M(\theta) \end{bmatrix} = \begin{bmatrix} -L \\ M_{\frac{1}{4}} + b\left(\frac{1}{2} + a\right) L \end{bmatrix}, \tag{3.56}$$

where the pitch variable θ is now replaced by $M(\theta)$. Note, L and $M_{\frac{1}{4}}$ remain the same as in Equation 3.37. Then, following the same procedure as in Section 3.3, we rearrange the equations by combining terms that have the same variables, and making all parameters dimensionless, yielding

$$\begin{bmatrix} \mu + 1 & \mu x_\theta - a \\ \mu x_\theta - a & \mu r^2 + \left(\frac{1}{8} + a^2\right) \end{bmatrix} \begin{bmatrix} \bar{h}'' \\ \bar{\theta}'' \end{bmatrix} = \begin{bmatrix} -\mu\sigma^2 & -2V^2 \\ 0 & V^2\left(1 + 2a\right) \end{bmatrix} \begin{bmatrix} \bar{h} \\ \bar{\theta} \end{bmatrix}$$
$$+ \begin{bmatrix} -2V & (2a-2)V \\ (1+2a)V & (a - 2a^2)V \end{bmatrix} \begin{bmatrix} \bar{h}' \\ \bar{\theta}' \end{bmatrix} + \begin{bmatrix} 2V^2 \\ -\left(1 + 2a\right)V^2 \end{bmatrix} \begin{bmatrix} \bar{\lambda}_0 \end{bmatrix} + \begin{bmatrix} 0 \\ -\mu r^2 \end{bmatrix} \begin{bmatrix} M(\theta) \end{bmatrix}, \tag{3.57}$$

or

$$\begin{bmatrix} M^*{}_{sys} \end{bmatrix} \begin{bmatrix} \bar{h}'' \\ \bar{\theta}'' \end{bmatrix} = \begin{bmatrix} \widetilde{K}^*_{sys} \end{bmatrix} \begin{bmatrix} \bar{h} \\ \bar{\theta} \end{bmatrix} + \begin{bmatrix} B^*{}_{aero} \end{bmatrix} \begin{bmatrix} \bar{h}' \\ \bar{\theta}' \end{bmatrix} + \begin{bmatrix} P^*{}_{aero} \end{bmatrix} \begin{bmatrix} \bar{\lambda}_0 \end{bmatrix} + \begin{bmatrix} 0 \\ -\mu r^2 \end{bmatrix} \begin{bmatrix} M(\bar{\theta}) \end{bmatrix}. \tag{3.58}$$

Finally, we put the above equation into standard form, substitute $\bar{\lambda}_0$ with the ex-

panded form of the finite state variables $\bar{\lambda}_1,\ \bar{\lambda}_2, \ldots,\ \bar{\lambda}_N$ and their relationship with the system variables of plunge and pitch as shown in the previous section, and introduce the same state-variables as Equation 3.50. We obtain the final nonlinear state-space form as

$$\begin{bmatrix} \dot{x}_1 \\ \dot{x}_2 \\ \dot{x}_3 \\ \dot{x}_4 \\ \dot{x}_5 \\ \dot{x}_6 \\ \vdots \\ \dot{x}_N \end{bmatrix} = \left[\begin{array}{cccc:ccc:c} 0 & 0 & 1 & 0 & 0 & 0 & \ldots & 0 & 0 \\ 0 & 0 & 0 & 1 & 0 & 0 & \ldots & 0 & 0 \\ \hdashline \multicolumn{4}{c:}{\begin{bmatrix} \widetilde{E} \end{bmatrix} \begin{bmatrix} F \end{bmatrix}} & \multicolumn{3}{c:}{\begin{bmatrix} \bar{G} \end{bmatrix}} & \begin{bmatrix} L \end{bmatrix} \\ \hdashline \multicolumn{4}{c:}{\begin{bmatrix} \widetilde{R}_{sys} \end{bmatrix}} & \multicolumn{3}{c:}{\begin{bmatrix} \widetilde{R}_{aero} \end{bmatrix}} & \begin{bmatrix} \widetilde{R}_{non} \end{bmatrix} \\ & & & & & & & & \end{array}\right] \begin{bmatrix} x_1 \\ x_2 \\ x_3 \\ x_4 \\ x_5 \\ x_6 \\ \vdots \\ x_N \\ M(x_2) \end{bmatrix}, \tag{3.59}$$

where

$$\begin{bmatrix} \widetilde{E} \end{bmatrix} = \begin{bmatrix} M^*_{sys} \end{bmatrix}^{-1} \begin{bmatrix} \widetilde{K}^*_{sys} \end{bmatrix} \tag{3.60a}$$

$$\begin{bmatrix} F \end{bmatrix} = \begin{bmatrix} M^*_{sys} \end{bmatrix}^{-1} \begin{bmatrix} B^*_{aero} \end{bmatrix} \tag{3.60b}$$

$$\begin{bmatrix} L \end{bmatrix} = \begin{bmatrix} M^*_{sys} \end{bmatrix}^{-1} \begin{bmatrix} 0 \\ -\mu r^2 \end{bmatrix} \tag{3.60c}$$

$$\begin{bmatrix} \bar{G} \end{bmatrix} = \begin{bmatrix} M^*_{sys} \end{bmatrix}^{-1} \begin{bmatrix} b_1 V & -(0.5+a) b_1 V \\ b_2 V & -(0.5+a) b_2 V \\ \vdots & \vdots \\ b_N V & -(0.5+a) b_N V \end{bmatrix}^T \tag{3.61}$$

$$\left[\widetilde{R}_{sys} \right] = \left[A \right]^{-1} \left\{ c \right\} \begin{bmatrix} \widetilde{E}(1,1) + (0.5-a)\widetilde{E}(2,1) \\ \widetilde{E}(1,2) + (0.5-a)\widetilde{E}(2,2) \\ F(1,1) + (0.5-a)F(2,1) \\ F(1,2) + (0.5-a)F(2,2) + V \end{bmatrix}^T \tag{3.62}$$

$$\left[\widetilde{R}_{aero} \right] = \left[A \right]^{-1} \left\{ c \right\} \begin{bmatrix} \bar{G}(1,1) + (0.5-a)\bar{G}(2,1) \\ \bar{G}(1,2) + (0.5-a)\bar{G}(2,2) \\ \vdots \\ \bar{G}(1,N) + (0.5-a)\bar{G}(2,N) \end{bmatrix}^T - V \left[A \right]^{-1} \tag{3.63}$$

$$\left[\widetilde{R}_{non} \right] = \left[A \right]^{-1} \left\{ c \right\} \left[L(1,1) + (0.5-a)L(2,1) \right]. \tag{3.64}$$

Note, the tilde on the variables in Equations 3.59-3.62 signifies nonlinear.

Now, we are ready to begin conducting time domain analysis on this system. In the next chapter, the numerical methodologies are explained and the subsequent results are shown. A discussion of the results is given along with a comparison of data with the published literature. Finally, the data is then used to build the initial probabilistic framework for the final goal of this thesis.

Chapter 4

Results and Discussion

In this chapter, we provide the results from performing dynamical analyses on the linear and nonlinear aeroelastic systems derived in Chapter 3. We initially provide the computational framework necessary for conducting time domain analyses on all of the aeroelastic systems. All considerations that were made for the numerical integration schemes are given in detail, along with the discussions on their numerical stability and convergence. A novel discussion regarding the issue of numerical stiffness in the differential equation is also provided. Next, we provide the values for the parameters in our aeroelastic systems.

This chapter provides the results from the time domain analysis performed on the linear system and the nonlinear systems. Methods used for the nonlinear dynamical analyses are provided, followed by the discussion of the results. Finally, we wrap up this chapter by detailing the probabilistic framework and by providing the results from the stochastic analysis of the nonlinear systems.

4.1 Numerical Procedures Used

To thoroughly examine our system in the time domain, detailed time histories of our model were recorded for all velocities of interest (see Section 4.1.3). To accomplish

this, all aeroelastic systems (linear and nonlinear) were numerically integrated over a *sufficiently* large range of non-dimensional time such that all variabilities of the system behavior was fully captured well into its steady-state. This procedure was then repeated for every velocity of interest. Once the time histories were obtained, further numerical studies were done to identify stable and unstable regimes and unique phenomena - such as limit cycle oscillations, quasi-periodic behavior, and chaos - that are attributed to the different types of nonlinearities examined. This section will discuss and explain the criteria for determining the scale, scope, and methods of the time domain analyses.

For this thesis, all numerical studies were conducted in MATLAB on a personal laptop with an Intel(R) Core(TM) i5-8250U CPU operating at 1.60GHz. Limitations in accuracy, along with the trade-offs in computing time, are addressed below.

4.1.1 Differential Equation Solvers

Three different types of differential equation solvers were examined. The first is the classical Fourth Order Runge-Kutta (RK4) solver. This is a fixed step size solver, where each step of the numerical integration is fixed to a preselected step-size of h. Given a system of first order differential equations, expressed as

$$\dot{x} = f(t, x), \tag{4.1}$$

the RK4 method recursively estimates the $n + 1$ state of x from the values of its previous state, given by

$$x_{n+1} = x_n + \frac{h}{6}\left(k_1 + 2k_2 + 2k_3 + k_4\right), \tag{4.2}$$

where

$$k_1 = f(t_n, x_n)$$

$$k_2 = f(t_n + \frac{h}{2}, x_n + \frac{1}{2}k_1 h)$$

$$k_3 = f(t_n + \frac{h}{2}, x_n + \frac{1}{2}k_2 h)$$

$$k_1 = f(t_n + h, x_n + k_3 h)$$

$$t_{n+1} = t_n + h.$$

The accuracy of the RK4 method improves as the step size h is reduced [107]. However, the trade-off is that the total time required for computation drastically increases depending on the order of the system. We wrote a `MATLAB` script that performed the numerical integration of the RK4 method.

The second solver that was examined is the built-in `MATLAB` function `ode45`. This is a variable step-size *nonstiff* differential equation solver. It is the most commonly used `MATLAB` differential equation solver, using an explicit fourth *and* fifth order Runge-Kutta formula, known as the Dormand-Prince method, to compute the solution of x_{n+1} using information from the x_n state. The relative step size is governed by convergence of the solver, as specified by the error tolerances defined in the `ode45` function [108].

Finally, the third solver that was examined is the built-in `MATLAB` function `ode15s`. This function is a variable step size, variable order solver based on numerical differentiation formulas of orders 1 to 5, where a multi-step approach is utilized to yield the solution [108]. The `ode15s` function is generally used for *stiff* differential equations. Stiffness is broadly regarded as phenomena where solutions to differential equations can become numerically unstable when using certain types of numerical solvers. This problem can present itself in different ways in `MATLAB`, such as when a numerical solver fails to provide a solution, is very inefficient, or converges to an incorrect solution [109, 110]. While it may appear natural to use this type of solver if stiffness is suspected, there is added computational cost for large nonlinear systems when using `ode15s` due to the additional algorithmic output necessary to perform the numerical integration.

In nonlinear aeroelasticity time-domain analyses, solvers that utilize some variation of the RK4 method are most frequently used. Variable step size solvers are only typically used when free play is modeled using a piecewise function, due to the non-smooth nature of the model [35, 36, 111]. Otherwise, the classical RK4 method is utilized with fixed-step size, particularly in instances with cubic nonlinearity. We will show with our numerical results that this method is not only inefficient, but it is also a poor choice when stiffness is suspected in the differential equations.

In most cases, the rationale for choice and type of solver is heavily influenced by the computational cost (speed). However, very little discussion is found in the literature examining the manipulation of error tolerances, especially when the numerical solvers use variable step size. This matter becomes more important when considering systems that have multiple stability regions, as in the case of nonlinear systems. A solver with error tolerances that are not small enough could produce solutions that have settled incorrectly or drifted into different equilibrium states [110]. These phenomena can also be mistaken as stiffness being present in the differential equations. In our results, we will show that choosing smaller error tolerances dramatically affect the computed behavior of a strongly nonlinear system near its flutter boundary.

The final discussion point in the numerical framework is that stiffness may arise in the differential equations that have strong, coupled nonlinearities. To our knowledge, this thesis may be the first to present such a discussion on stiff differential equations in the field of free play. In some instances when stiffness is present, there may be stability regions where some components of a solution decay more rapidly over other parts of the solution, which may result in inaccurate solutions. The instances that are considered in this thesis looked into how rapidly changing stability regions near the flutter boundary can be incorrectly computed. While the natural approach may be to use stiff solvers, they too are prone to yielding inaccurate results if their error tolerances are too large. Therefore, we will show that using a solver that

prioritizes high accuracy (smaller error tolerances) over the computational speed in specified situations can produce both reliable and efficient solutions.

4.1.2 Error Control

Selecting the appropriate error control bounds is a tricky and complicated task. The `MATLAB` ODE solvers track error at each state using an algorithm that computes the local error by taking both relative error and absolute error as functional inputs. Specific details are can be found in reference [108]. The default values of relative error, `'RelTol'`, and absolute error, `'AbsTol'`, are set to 10^{-3} and 10^{-6}, respectively. As a general rule of thumb, `'RelTol'` determines the number of correct significant digits in a solution at each time step, whereas `'AbsTol'` determines the threshold below which the difference in the computed values are unimportant [112]. There is drawback to setting these tolerances too low, which can lead to increased accumulation of round-off error due to the large number of integration steps necessary for computing a solution. Trial and error is necessary to some extent as is an understanding of the physical interpretations of the solutions output by the numerical solvers.

For our purposes, we decided to only manipulate the relative error while holding absolute error at its default value because we are dealing with small dimensionless values that are sensitive to changes in the initial conditions. Multiple simulations were run using solvers with default error values and solvers in which `'RelTol'` was set to 10^{-7}. The results and discussion are provided in the subsequent sections. The main conclusion was that smaller relative error was most important to consider when calculating results near the flutter boundary.

4.1.3 Baseline Solver and Integration Requirements

Unless mentioned otherwise, the `ode45` function was the baseline solver that was adopted here for obtaining a majority of the data presented in the subsequent sections.

We developed a conditional scheme that would select a modified version of the `ode45` function with smaller error tolerances if the velocity was below the linear flutter velocity. For such velocities, the relative error tolerance of 10^{-7} was used in the `ode45` function due to our needs of higher accuracy for results near the flutter boundary. For velocities higher than the linear flutter velocity, our code would switch to using the unmodified `ode45` function due to its faster computation speed. All of the simulation results using other solvers were compared to the results of this baseline solver that had the added logically controlled error tolerances.

All numerical simulations were integrated from zero to 3×10^5 dimensionless time. This range was determined through trial and error. For the most part, all data associated with all times larger than 1.5×10^5 were found to be steady-state values. The rate at which the transient behavior decayed to steady state varied for the different ranges of velocities, with slower transition to steady-state for lower velocities. Thus, we truncated the data for all times below 1.5×10^5 so that the steady-state values were used for all of our analyses.

The dimensionless velocities of interest for our studies range from 0.5 to 4.2. The lower end was selected to start at 0.5 because for lesser velocities the systems was essentially motionless with zero displacement for all linear and nonlinear systems. All interesting behavior was found for velocities larger than 0.5, and thus, that was the starting point for all time-domain analysis. The upper end velocity was set at a value much larger than the linear flutter velocity. While, no subsonic aircraft is truly designed to operate at velocities that exceed its projected linear flutter speed, such rare instances can occur during an in flight emergency, perhaps if an aircraft experiences an uncontrolled dive. Therefore, it is interesting from a theoretical perspective to see what type of instabilities may occur should an aircraft exceed its designed velocities. Using the FAA's ultimate factor of safety of 1.5 [113], we set the upper threshold of the velocities by multiplying the rounded up linear flutter velocity of 2.8 by 1.5,

giving us 4.2.

Lastly, the initial conditions for all numerical simulations were set to zero for all states except pitch, which was set to an initial perturbation of $-3°$. The initial perturbation was set in the pitch degree of freedom because that is the state that was closely examined for this thesis. While the numerical integration gives us the data for all of the states of the examined system, the pitch degree of freedom is most important to examine because the nonlinearities in stiffness are present in the pitch. Therefore, all of the data that is presented in this thesis correspond only to the pitch dynamics of the airfoil system.

4.2 Constant Parameters

The linear and nonlinear state space equations, Equations 3.51 and 3.59, were analyzed by using various time domain methods that are explained in the subsequent sections. In these equations, the following system constants were used $a = -\frac{1}{3},\ e = -\frac{1}{10},\ \sigma = \frac{2}{5},\ r = -\frac{2}{5},\ \mu = 50$. All constants were selected based on values found in the literature reviewed in Chapter 2. The choice of N, the number of inflow states in the aerodynamics model, was set to 9 because of its good agreement with Theodorsen's model [104]. While a larger N would lead to better accuracy, choosing N too large would lead to ill-conditioning in the state-space matrix due to how b_n is defined in Equation 3.32. Varying N can be a future topic of research with free play studies.

4.3 Linear Flutter

The first step is to determine the linear flutter velocity. This is a very important metric that not only helps in the design of the scope and the scale of the aeroelastic studies, but also serves as a baseline measurement against which the instabilities of the nonlinear systems are compared.

The linear flutter speed is computed by conducting an eigenvalue analysis of linear Equation 3.51. The system has a total of 13 eigenvalues, of which the first four correspond to structural deformation in bending and torsion, and the last 9 correspond to the behavior of the 9 aerodynamic induced flow states. Starting at $V = 0$, and increasing the dimensionless velocity in 10^{-3} increments, all of the system's eigenvalues were calculated, recorded, and plotted. The system's stability was determined by the real parts of the eigenvalues. Positive real eigenvalues indicate that the system has became unstable at that velocity corresponding to the eigenvalue. This is known as flutter. The velocity at which positive real eigenvalues are first observed is denoted as the linear flutter velocity, V_f. This value was found to be $V_f = 2.783$ for our aeroelastic model. The first two eigenvalues, corresponding to the plunge and the pitch, were the only eigenvalues to become positive in the range of velocities examined. In Figure 4.1, the evolution of the first four eigenvalues is provided. In comparison, the linearized model of Dai et al. [34] yields $V_f = 2.546$ when the same system constants are used, corresponding to a relative difference of 9.3%. The difference in these two results are likely due to the choice of the aerodynamics model. We will maintain our results to be accurate for our system with the aerodynamics model that we selected to use.

For a more accurate flutter velocity, we performed the eigenvalue analysis with 10^{-6} increments. We found that the refined linear flutter velocity to be $V_f = 2.782970$. Establishing this benchmark value for linear flutter velocity, we next begin time domain analysis of the both the linear and nonlinear systems to examine the system's behavior at a range of velocities of interest.

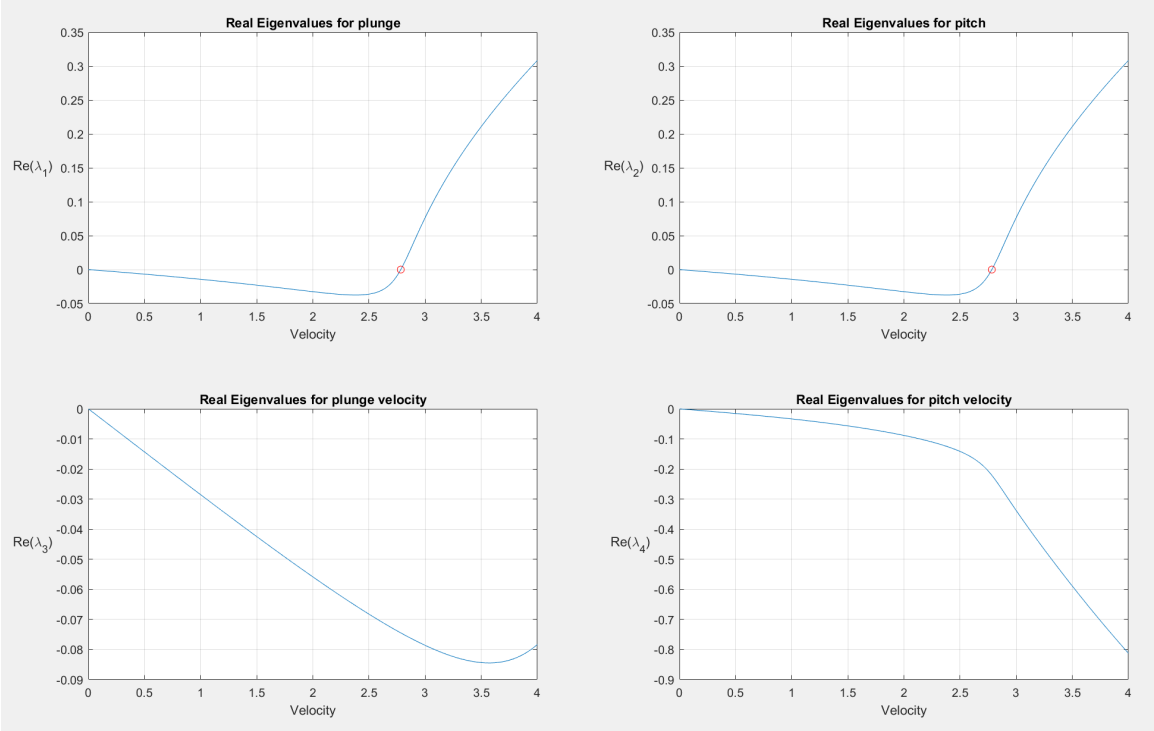

Figure 4.1: The red circle in the graphs on the top row indicate the velocities at which where the system transitions to having positive eigenvalues.

4.4 Results: Linear System

The dynamical behavior of the linear system is straightforward. For all velocities below the linear flutter speed of V_f, the system converges to zero displacement for its steady state. For velocities larger than V_f, the system completely diverges and the solutions' amplitudes grow without bound. At the flutter velocity $V_f = 2.782970$, the system bifurcates into a fixed amplitude oscillation with amplitude size of approximately 2.145 degrees as shown in time history plot given in Figure 4.2.

It should be noted that the system's true flutter velocity is likely an irrational number that is slightly different than 2.782970 by an order of magnitude smaller than 10^{-6}. Despite its phase plot showing an apparent single closed loop with two fixed points, the system's response is very slowing changing its amplitude. This was seen

by zooming into the positive fixed points in the phase plot, as shown in Figure 4.3. There appears a thick band of curves that are moving away from each other by a distance less than 10^{-8}, as seen by the fact that no new fixed points are detected after the first few initial points.

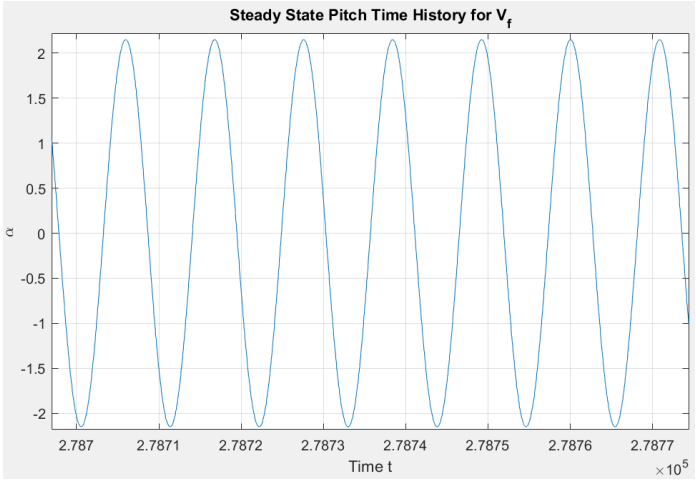

Figure 4.2: This time history plot shows an apparent fixed amplitude oscillation.

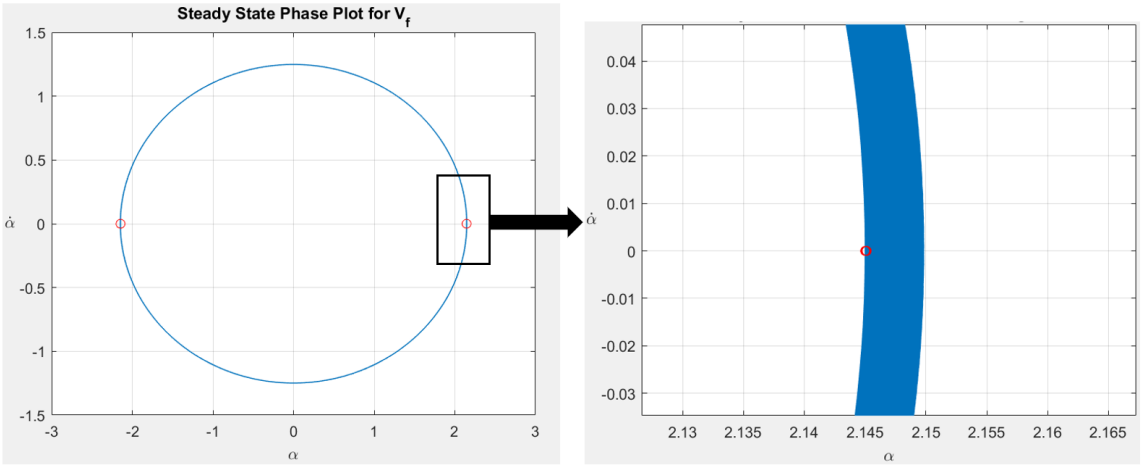

Figure 4.3: This phase plot for linear system at the computed linear flutter velocity. The red dots show the detected fixed points.

At velocities very close to V_f, the system's behavior is interesting. When the velocity is less than V_f, the rate of decay towards motionless steady state amplitude reduces drastically. In a similar manner, the rate of amplitude increase beyond the linear flutter is also reduced drastically. The behavior for both velocities is shown in

Figures 4.4a and 4.4b. In Figure 4.4a, at velocity $V = 2.8792$, the system decays very slowly and has not settled into a steady state value at time 3×10^5. In Figure 4.4b, the system continually grows in amplitude in a very slow manner. In both cases, the rate of decay or growth appears to be slightly exponential.

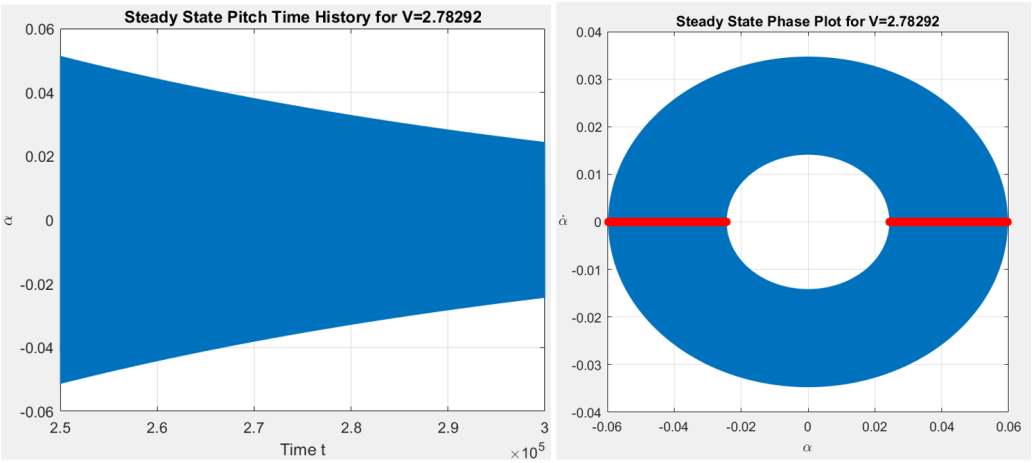

(a)

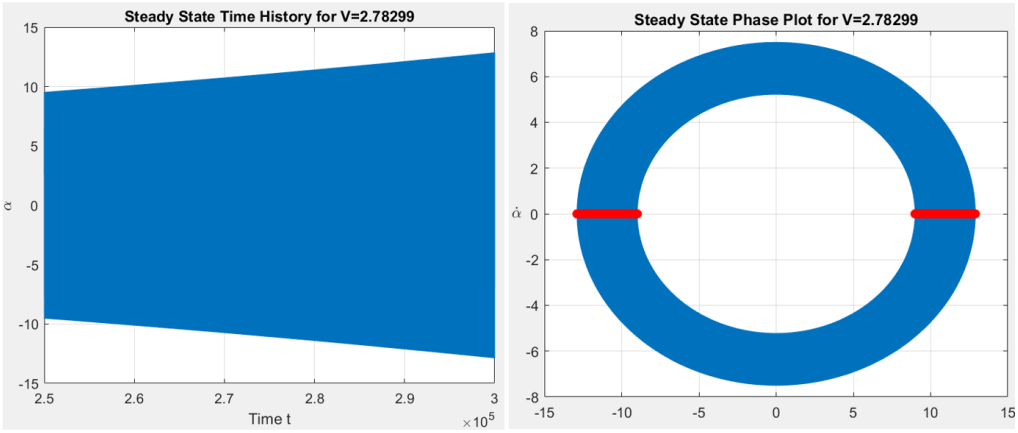

(b)

Figure 4.4: The time histories and phase plots for velocities near the linear flutter velocity. (a) The phase plot trajectory is slowly spiraling into the center. (b) The phase plot in slowly spiraling away from the center.

As explained in Section 4.1.1, the RK4 method is computationally inefficient when compared with the `ode45` function. In the table below, we show a side-by-side run time comparison between the RK4 method and the `ode45` function for three different velocities. The only case when the RK4 method was faster than the `ode45`

function is at the linear flutter velocity. Otherwise, the RK4 method was approximately 4 to 7 times slower than the `ode45` function.

	`ode45`	RK4 Method
$V = V_f$	39.412 seconds	23.858 seconds
$V = 1.17$	15.742 seconds	104.342 seconds
$V = 2.3$	29.710 seconds	112.171 seconds

Table 4.1: Comparison of run times using two different solvers.

Using both solvers, we show the time histories and phase plots for velocities $V = 1.17$ and $V = 2.3$ in Figures 4.5 and 4.6, respectively. While both appear identical, their steady-state phase plots reveal an interesting finding. Unlike the RK4 method, the `ode45` function does not completely settle to zero. There appears to be some residual roundoff error on the order of 10^{-12}. While such a small error may not appear as quantitatively significant, it does make us aware that all of our data is subject to some level of inaccuracies due the accumulation of roundoff error. The reason for the presence of a residual error is due to manner in which the solver's algorithm produces results. Detailed discussion can be found in references [108, 112].

Lastly, we tested the use of a stiff solver to see how the results would come out. The results, shown in Figure 4.7, were very poor and failed to converge accurately, thus suggesting that stiffness is not an important consideration with the linear system.

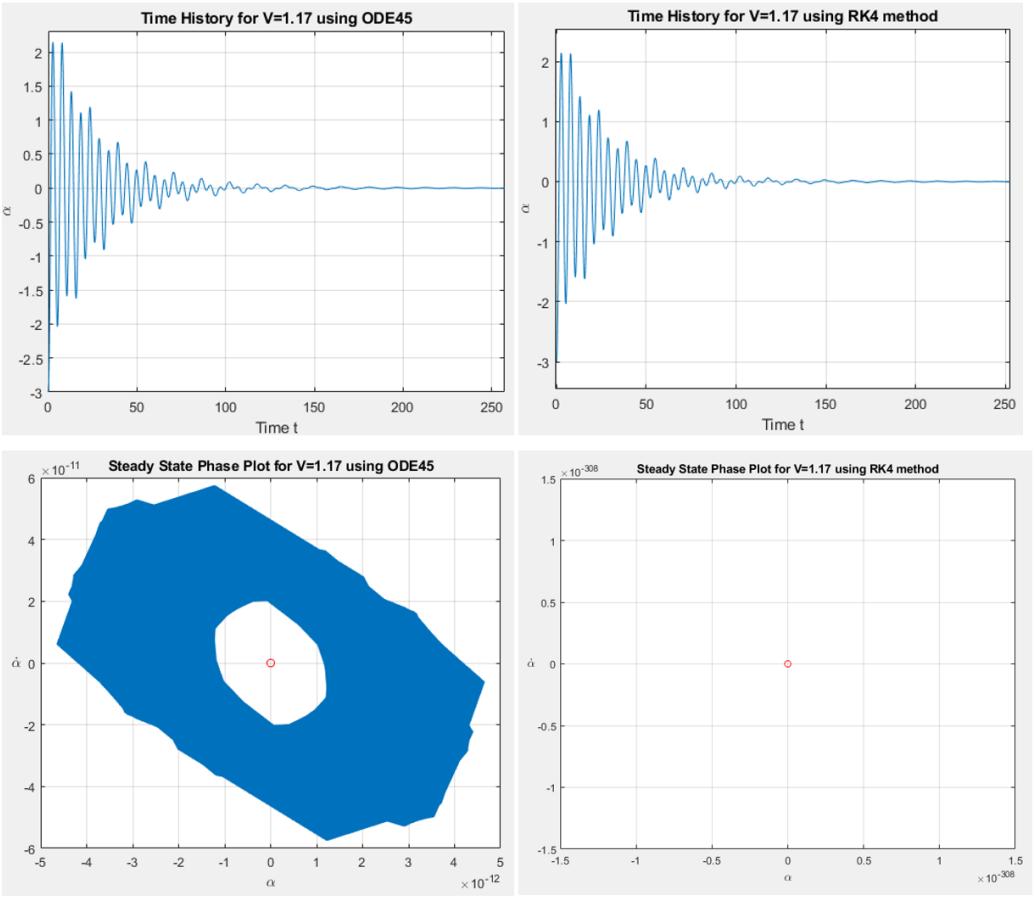

Figure 4.5: The left column of plots (time history and phase plot) are produced by using the `ode45` function. The right column of plots are produced by using the RK4 method. Both systems were solved for identical conditions at $V = 1.17$. Their solutions yield apparently identical time histories. However, their steady state behavior is slightly different, with the `ode45` function showing some residual roundoff error preventing the solution from fully settling to zero displacement. This is seen in the phase plot on bottom left. The RK4 solver allows for the correct steady state convergence to motionless pitch behavior, as seen by its phase plot on the bottom right, showing a single point at zero.

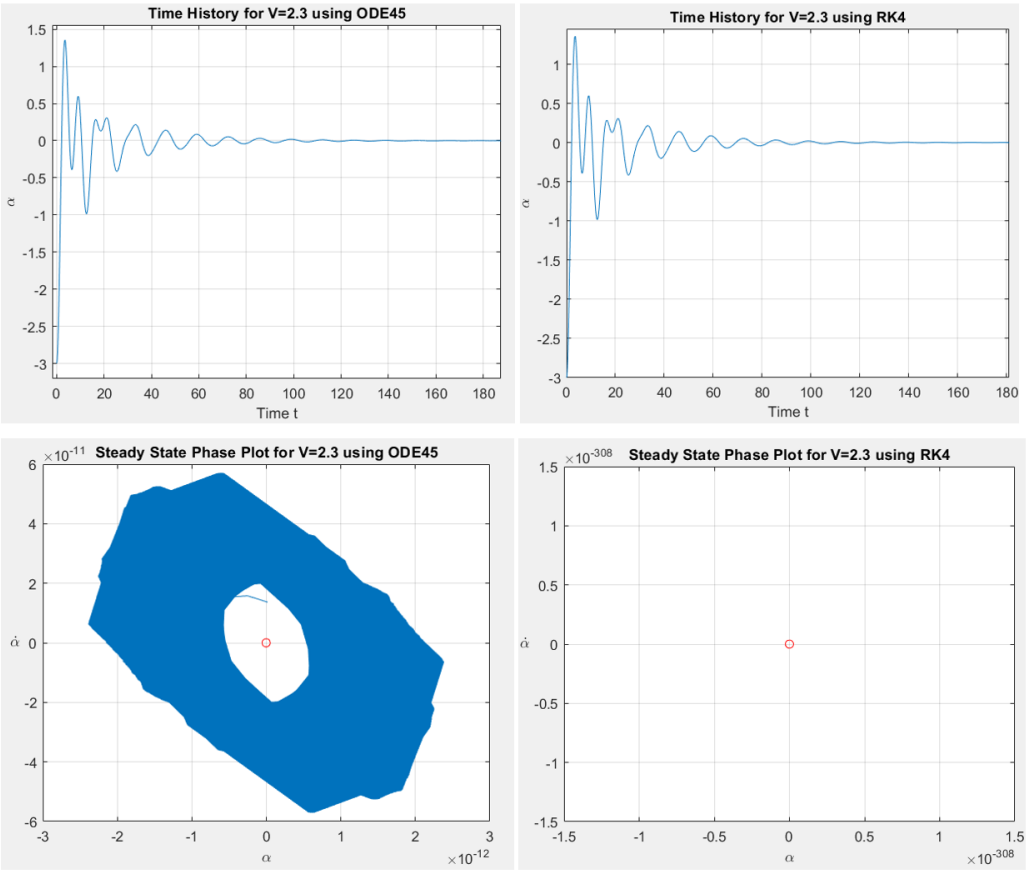

Figure 4.6: Similar to Figure 4.5, the left column of plots are produced by using the `ode45` function. The right column of plots are produced by using the RK4 method. Both systems were solved for the sub-flutter velocity of $V = 2.3$, yielding apparently identical time histories. Once again, as previously shown, the `ode45` function has residual roundoff error in its phase plot, shown on the bottom left, which prevents the solution from ever settling into zero displacement. In comparison, the phase plot produced by the RK4 solver, shown on the bottom right, gives a single point that is plotted at zero.

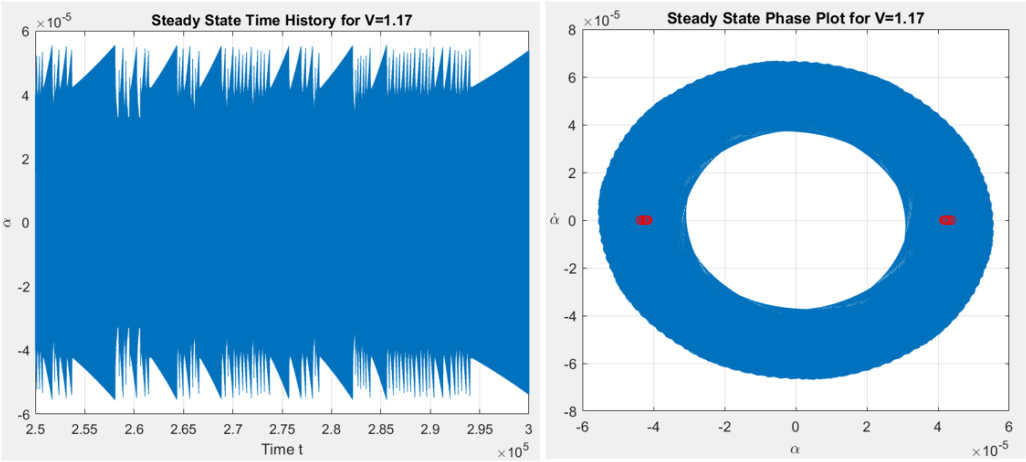

Figure 4.7: The use of a stiff solver when it is not warranted can result in poor and inaccurate solutions. These plots show large errors on the order of 10^{-5}.

4.5 Nonlinear Dynamical Analyses

For nonlinear systems, identifying the various regimes of nonlinear behavior is crucial for gaining a physical understanding of how the system behaves under varied specific conditions. Two large classes of nonlinear behavior were examined in this thesis: periodic (and quasiperiodic) oscillations and chaotic oscillations. Different analytical tools were used to determine the type of behavior experienced by the system for the specific conditions examined, and the phenomena associated with these. This section will discuss the methods that were used and the study design that was subsequently created.

4.5.1 Periodic Oscillations

After performing the numerical integration, the data for the pitch and pitch velocities were used to plot the steady-state phase portraits. From these plots, the initial assessments of periodicity was made. If repeating or almost-repeating closed loop trajectories were mapped in the phase portraits, then periodicity can be qualitatively assumed. Further assessments are necessary to quantitatively prove this assumption.

First, from the phase portraits, the fixed points or zero-crossings have to be obtained by following the orbits through their phase spaces. Since the accuracy of our data is limited by roundoff error in the numerical integration, we deemed that any two fixed points were considered as repeating fixed points if the absolute value difference was less than 10^{-8}. In the same manner, if the numerically integrated values for steady-state pitch settled into an infinitesimally decaying orbit whose peak amplitudes differed by less than 10^{-8}, then the difference was deemed negligible and the steady-state fixed point value was presumed to be the average of the two infinitesimal peaks. Following this procedure allowed us to determine if the orbits were periodic; if they were, then the number of repeating fixed points can determine the order of the orbit's periodicity [80]. Fixed points were obtained for all velocities of interest for all of the nonlinearities studied, and then plotted to create 2-D bifurcation diagrams corresponding to the various nonlinearities.

If periodicity cannot be clearly determined by the first method, then more advanced time-domain and frequency-domain analyses need to be applied. Autocorrelation analysis and Fourier analysis are the two methods that were used. Since our data is discretized, numerical discrete-time autocorrelation functions and Fast Fourier Transforms (FFT) were used to generate normalized autocorrelation plots and amplitude spectra. For periodic motion, the FFT would yield narrow band amplitude spectra with distinct peaks; the autocorrelation plot would yield repeating or consistent patterns if periodicity is present [114]. Additionally, if periodic motion is clearly determined, then the mean of the separation of the peaks in the autocorrelation plots can give a quantitative measure of the period of these oscillations.

4.5.2 Quasi-Periodic Oscillations and Subharmonics

As the velocity varies, periodicity may become more difficult to identify if the system is headed towards chaos. There are three main precursors to chaos that we looked

into: the presence of subharmonics, quasi-periodic oscillations, and transient chaos [115]. A stable periodic system can bifurcate and experience period-doubling with when the velocity changes. This gives rise to smaller frequency oscillations being observed within the larger periodic oscillations. In the phase space, this is observed by the presence of smaller self-intersecting closed loops within a larger closed loop. In the frequency domain, this is observed by the presence of large peaks at frequencies below the dominant frequency. With the presence of more subharmonics and period doubling, the system gets closer to chaos [114].

Another identifier of pre-chaos is the loss of true periodicity in a phenomena known as quasi-periodic oscillations. Such oscillations occur when the solution contains the sum of periodic oscillations whose frequencies are incommensurable [115]. When the frequencies are unknown, as in the case with our solutions, three graphical methods can be used to adequately make this judgement. First, the phase portrait will show graphs that are almost-periodic yet do not have clearly repeating oscillations. Their FFTs will show thick peaks as opposed to narrow peaks. Lastly, the method of Poincaré section can be used, where a pseudo-phase portrait is mapped at regular fixed instances when a specified "event" occurs. Since this is not a periodically forced system, the standard method of selecting fixed time instances does not work [34]. We adopted the method described by Dai et al. [34] and defined our "event" criteria as instances when plunge velocity equals zero ($\dot{\alpha} = 0$) and the plunge acceleration is positive. For quasi-periodic oscillations, the Poincaré section will show a closed loop of points [116]. Observing quasi-periodic oscillations is strong precursor to chaos.

Finally, the last type aperiodic motion that we searched for is one that involves intermittent or transient chaos. This is observed as short bursts of chaos that can appear and disappear within an apparent periodic or nearly periodic motion [115]. Intermittency is both difficult to observe and understand. Therefore, it is important to map the time history over a sufficiently large range of time to allow for such chaotic

transients to settle within periodic motion. In this thesis, we use the simple approach of examining the time history simultaneously with the phase portrait to see if such behavior can be visually inspected.

4.5.3 Chaotic Oscillations

Chaos is a condition that is only possible in nonlinear systems. We used three different graphical indicators and one numerical indicator to show the existence of chaos. The first approach involved using FFTs. A broad spectrum of frequencies with many peaks can suggest the existence of chaos [114]. The second graphical tool used was the autocorrelation plots. Chaotic motion appears as random-like oscillations that decay to zero in the autocorrelation plots. Poincaré sections are the third type of plots used to identify chaos. When chaos is present, the plot appears as a cluster of seemingly unorganized points, as opposed to being well structured [114].

The final approach to identifying chaos is the quantitative method of numerically calculating the largest Lyapunov exponent (LLE). Following the procedure outlined by Sprott [115], we chose two sets of initial conditions separated by a magnitude of 10^{-8} in the vector space. Then the orbits are allowed to march forward in time by one increment. At that instant, the vector difference of the two orbits is calculated and the natural logarithm of its ratio with the original perturbation value is recorded. This value becomes the initial Lyapunov exponent value. The perturbed orbit's position is then rescaled such that its distance from the first orbit is the size of the original perturbation in the direction of its maximum expansion according to its position in the vector space. Then the whole process is repeated for the next time increment and the new Lyapunov exponent value is recorded by summing the new natural logarithm ratio with the previous value and taking their averages. The process is iterated for the entire range of time. If the converged values of the Lyapunov exponent are positive, then this is a numerical indication of chaos. A positive Lyapunov exponent suggests

that two orbits with perturbed initial conditions have their orbit diverging from each other exponentially fast.

While we have several different methods of capturing chaos, none of the methods can always guarantee that chaos is present. Therefore, we must make our judgement by using all of the methods together and justifying our rationale in that matter. If multiple indicators of chaos test positive, then we can safely assume the presence of chaos. However, if the tests are inconclusive, then our judgement must remain inconclusive as well; there may be more occuring than meets the eye.

4.6 Nonlinear Systems

Several different types of nonlinear models were examined. All models were either cubic or piecewise-linear functions. There are some similarities in the resulting behavior with both types of nonlinear models. Roughly summarized, both models lead to a reduction in the flutter velocity when compared with the linear flutter velocity. The reduction in the flutter velocity for both models is a function of the free play amount. These systems tend to undergo a sequence of bifurcations, with some of the nonlinearities producing chaotic behavior. Despite the similarities, some unique differences are found with the use of the two types of free play models. All of the discussion is provided below in the subsequent sections.

4.7 Results: Cubic Free Play Models

All cubic models that we examined took on the mathematical form of Equation 3.55, where $M(\theta) = C_1\theta + C_3\theta^3$. Different cubic models had different values for the constants C_1 and C_3. For our work, we examined two classes of cubic free play models. The first class of cubic models had values of C_1 and C_3 that we selected (user defined). We only looked at one such model where we chose $C_1 = 0.01$ and $C_3 = 50$. These values

were selected because there have been other studies that have previously looked into this exact cubic model. This allowed us to compare our results to these studies. In particular, we compared our results to those found in the paper by Dai et al. [34]. Not only did they use this exact cubic model, their state-space aeroelastic model was developed in a similar manner to our state-space model.

The second class of cubic models were the best fit cubic functions, where the values of C_1 and C_3 were selected based on the best fit approximation of the cubic models to the piecewise models of free play. The domain of best fit for the cubic models was selected to be between $-3^\circ \leq \alpha \leq 3^\circ$, a range that we established using trial and error, as explained in Section 3.4. Ten different values of free play were examined using the best fit approach, which gave us ten different cubic models that corresponded to each amount of free play. We combined real data from the aviation industry on free play and used that in the development of our best fit cubic models. One of our new contributions here is using the abundance of data obtained by studying these nonlinear aeroelastic systems and translating the variability and sensitivity of the data into a stochastic model that can give quantitatively measures on the likelihood of experiencing aeroelastic instability. A full discussion is provided in the following sections.

4.7.1 User Defined Cubic Model: $C_1 = 0.01$ and $C_3 = 50$

We initiated the study of this nonlinear cubic model by incorporating it into the nonlinear state space model of Equation 3.59. Numerically integrating this equation, we began the first analyses by plotting the system's complete bifurcation diagram for the entire range of velocities that were studied. This plot is shown in Figure 4.8, with the boxed regions being areas of interest for closer examination. It shows some unique and interesting behavior, particularly in the regions that we selected, labeled from A to D. In this section, we will provide a thorough discussion of the nonlinear

dynamical phenomena that is captured in the bifurcation diagram and its physical interpretation.

The first objective was to determine the nonlinear flutter velocity associated with our nonlinear system. We established this value to be the first velocity at which multiple fixed points are obtained. This is seen on the bifurcation diagram in the boxed Region A as multiple points being vertically plotted for a single velocity. In Figure 4.9, we zoom into the bifurcation diagram where we first observe the system breaking into multiple fixed points at $V = 1.15$. We verified this by running a `MATLAB` script that checked the number of fixed points that were being plotted at each velocity. This allowed us to establish $V = 1.15$ as the nonlinear flutter velocity. This value is a 41.323% reduction from the linear flutter velocity. Clearly then, nonlinearities must a part of any flutter analysis.

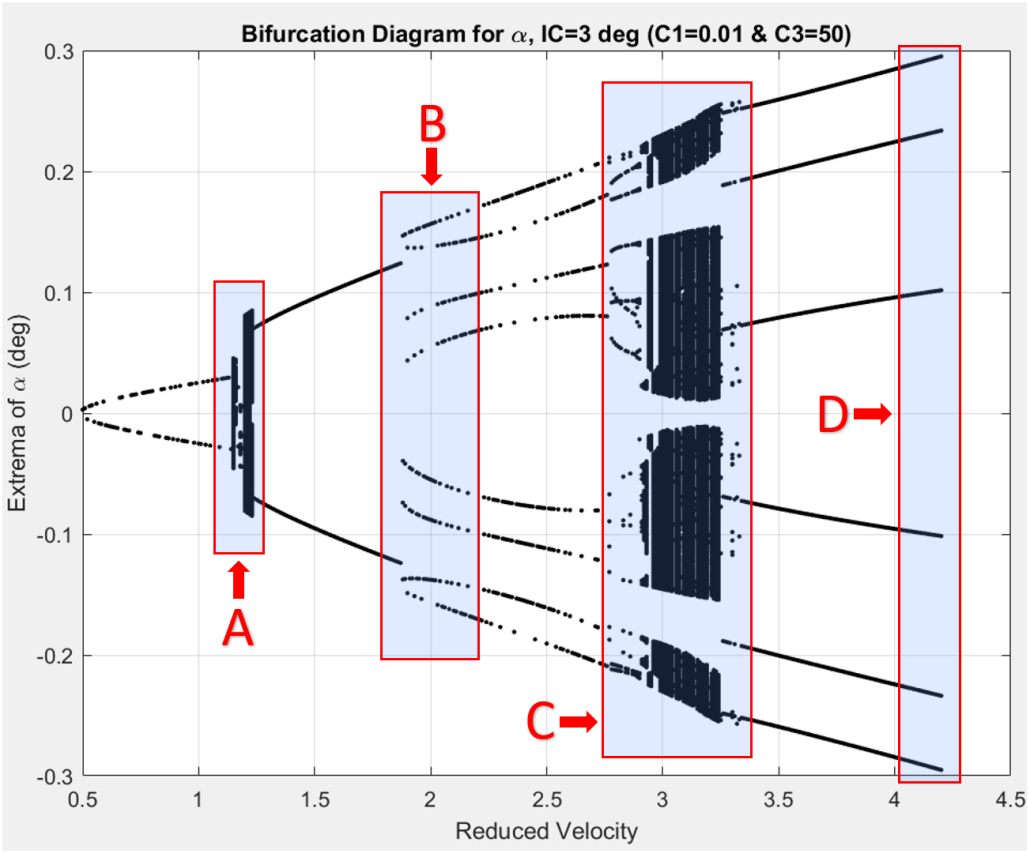

Figure 4.8: This bifurcation diagram allows us to qualitatively see how the system behaves for a large range of velocities.

It should be noted that the bifurcation diagram in Figure 4.8 shows that the system does not settle to zero displacement for values that are below its nonlinear flutter velocity. While the system does settle into a single point, this value is a nonzero displacement. Physically, this phenomena can appear to be puzzling. Our best explanation is that the strong cubic nonlinearity prevents this system from truly settling back into zero displacement when this system experiences unsteady aerodynamic forcing. When the system settles into nonzero displacements, the system is motionless - i.e., there is no pitch velocity.

As the velocity increases, the system switches between positive and negative displacement values into which it settles. For these increasing velocities that are below the nonlinear flutter velocity, the magnitude of the displacement into which the system settles also increases, switching back and forth between more positive or more negative displacement values as seen in the points plotted to the left of Region A in Figure 4.8. This switching behavior seen in Figure 4.9 also reveals that the system has no clear pattern on when it switches between positive and negative steady state displacement values. For example, from $V = 1.02$ to $V = 1.05$, the system alternates between positive and negative settled steady state values. Then there is group of consecutive velocities for which the system settles into positive displacement values, before jumping to a negative displacement value once. Then, a sequence positive fixed point values appear before a final switch to a negative fixed point value occurs, which is immediately followed by what appears to be a chaotic flutter.

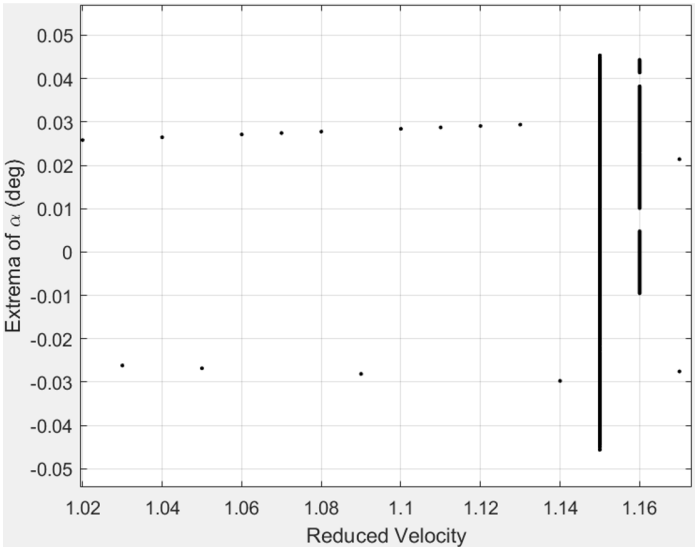

Figure 4.9: In Region A of Figure 4.8, at $V = 1.15$, we can see that the bifurcation diagram plots multiple fixed points, indicating that the system has encountered flutter.

Region A

There are numerous intriguing findings in the boxed Region A from Figure 4.8. First, we speculate that chaos occurs when the system first encounters flutter at $V = 1.15$. The thick black vertical band of many fixed points plotted at $V = 1.15$, seen in Figure 4.9, suggests that there is an apparent aperiodic behavior present, potentially chaotic. We tested our presumption by first plotting the time history at $V = 1.15$, shown in Figure 4.10. Immediately, we see that the response is very chaotic, with random-like oscillations that jump between positive pitch values and negative pitch values before the oscillations start to center at zero for much larger amplitudes. Plotting its phase portrait gives us Figure 4.11. This graph reveals a map that closely resembles the chaotic Lorenz system [80]. The manner in which the system evolves through time in its state space suggests the existence of a strange attractor. Such discussion is beyond the scope of this thesis but is very interesting to mention. Qualitatively, we have strong reason to believe in the existence of chaos at $V = 1.15$. Now, we must prove it through the use of the few different methods that we described in Section 4.5.

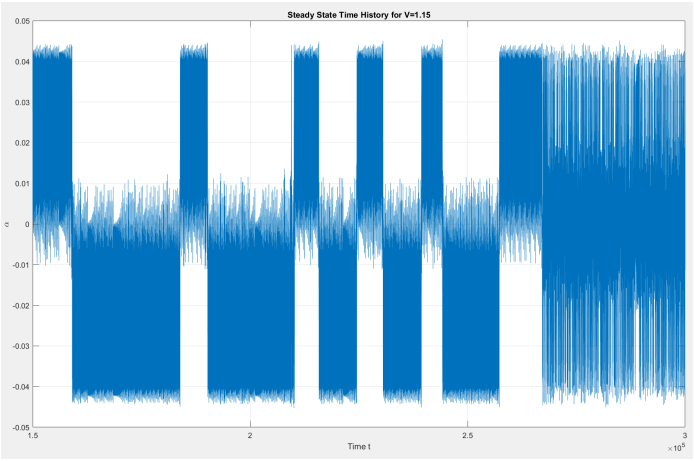

Figure 4.10: A chaotic time history is seen where the system's oscillatory response jumps around in a random-like manner.

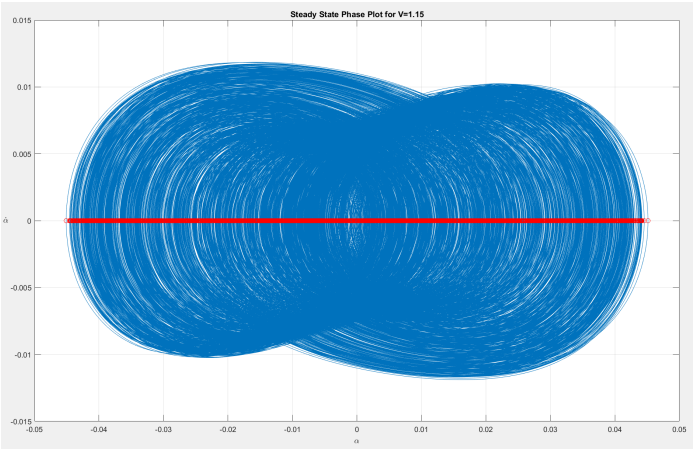

Figure 4.11: This shape resembles the butterfly plot of Lorenz's strange attractor. The red dots are the fixed points of the system's steady state that are seen as mapped vertically in the bifurcation diagram of Figure 4.8.

To prove the existence of the chaos, we plotted the Fast Fourier Transform (FFT), autocorrelation function, Poincaré section, and the largest Lyapunov exponent (LLE). The first three qualitative measures of chaos are given in Figures 4.13a, 4.13b, and 4.13c. In the FFT plot, we observe what appears to be a broad spectrum of frequencies with a few sharp peaks and many thick smaller peaks. It is interesting to see that the dominant frequency appears to be zero, which suggests that this system has an infinite period. This observation supports our belief of chaos. Furthermore, in Figure 4.13b, the autocorrelation function rapidly decays to zero, providing more

evidence of chaos. Even though there appears to be an underlying character to the shape of the decay in the autocorrelation function, a closer look reveals that there are many irregularities in the oscillations and no patterns emerge from it. Finally, the Poincaré section in Figure 4.13c shows a random-like cluster of points that are distributed in no particular shape. This is the final piece of qualitative evidence that proves that chaotic flutter is encountered at $V = 1.15$. The LLE plot is provided in Figure 4.12. Even though all of its values are positive, the plot cannot be reliably used to reasonable conclude chaos because it has large fluctuations that continue well into its steady state times. These fluctuations make it impossible to truly determine if the graph will stay positive as time goes to infinity. Despite that, the other three measure are enough to prove that chaos is present. Further discussion on the type of chaos encountered is beyond the scope of this thesis. More can be read on the numerous classifications of chaos in reference [115].

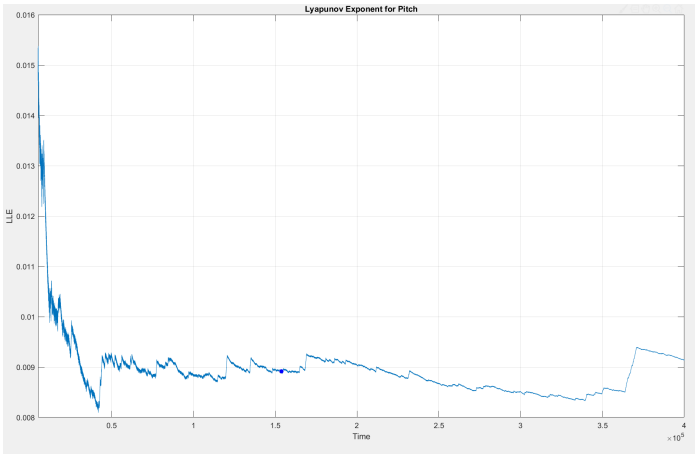

Figure 4.12: The LLE plot cannot be reliably used to prove chaos because of the large fluctuations seen towards its tail end. Possible refinements are needed in how the LLE was plotted.

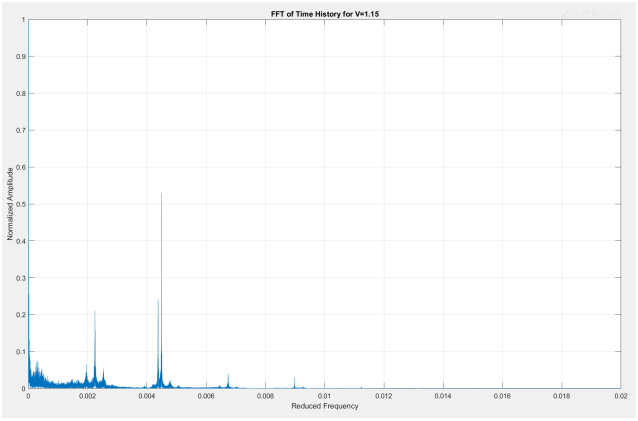

(a)

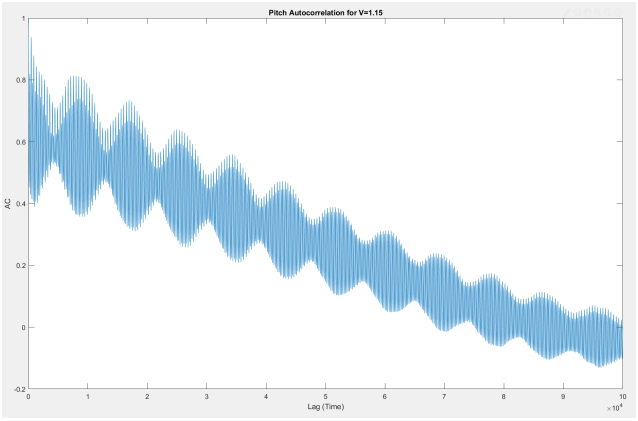

(b)

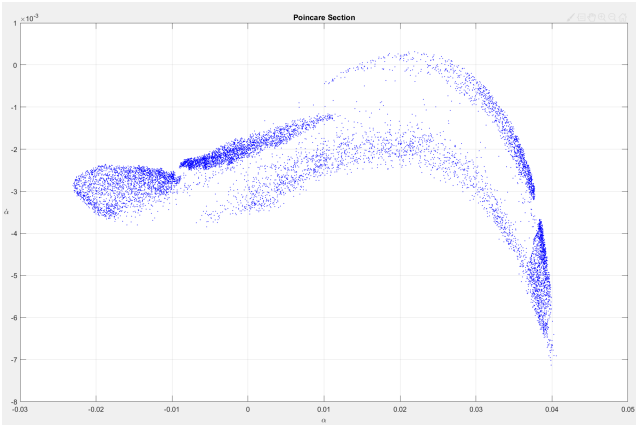

(c)

Figure 4.13: (a) In this FFT plot, a broad spectrum of frequencies is seen, with the dominant frequency appear at zero. (b) An irregularly shaped autocorrelation function that quickly decays to zero is observed. (c) A wide spread of points are plotted for the Poincaré section, consistent with chaotic behavior.

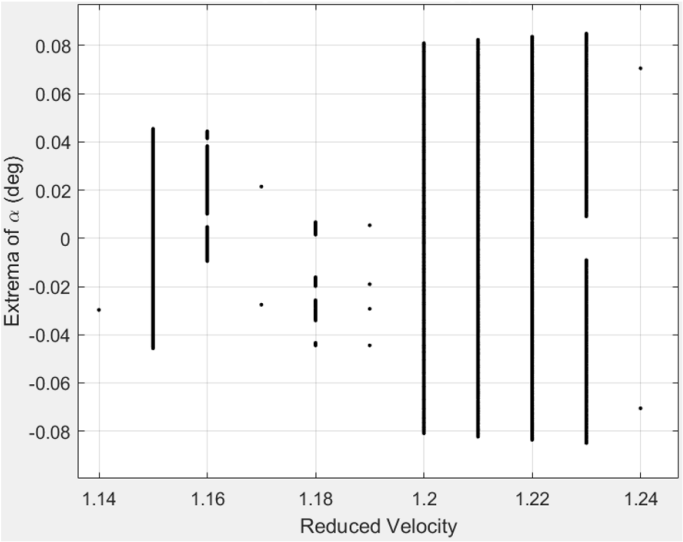

Figure 4.14: In Region A of the bifurcation diagram, the system's response structure wildly varies, going in and out of chaos for different velocities.

We find that after flutter is reached, the system undergoes a large change in the stability of its response structure for increasing velocities. When we zoom into Region A, as shown in Figure 4.14 above, we see that the system's steady state response for increasing velocity takes on a wise assortment of solutions. Chaos exists for almost all velocities between $V = 1.15$ to $V = 1.23$, except for velocities from $V = 1.17$ to $V = 1.19$. At these velocities, we observe both stable oscillatory response and quasi-periodic response, as shown in Figures 4.15 and 4.16, respectively. The periodic behavior at $V = 1.17$ and $V = 1.19$ is demonstrated in the FFT plots, given in Figure 4.17, which show narrow, distinct peaks and no underlying subharmonic behavior. Proving quasi-periodic behavior at $V = 1.18$ is more challenging but involves looking for closed-loop or semi-closed loop orbits in the Poincaré section and observing a set of small, narrow peaks that are either sub- or superharmonic. Both plots are shown in Figure 4.18.

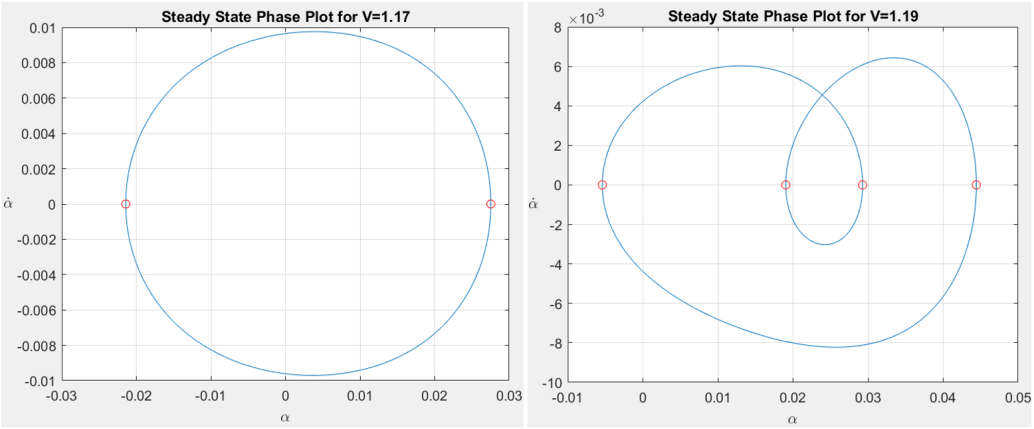

Figure 4.15: The phase plots of the system's response at $V = 1.17$ and $V = 1.19$ show stable oscillatory behavior with period-1 and period-2 limit cycles, respectively.

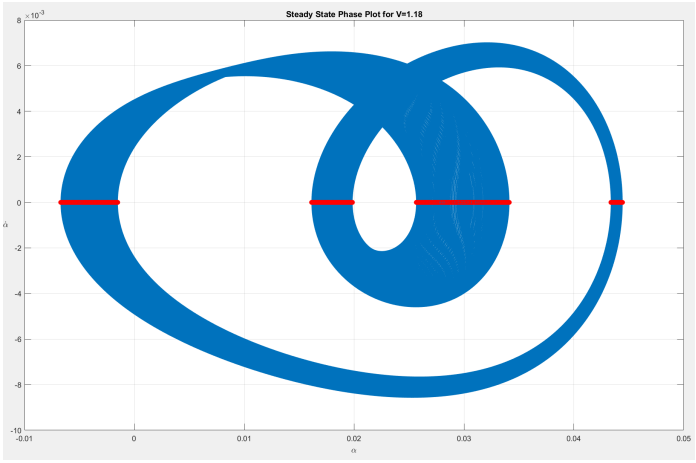

Figure 4.16: The phase plot for $V = 1.18$ shows trajectories that are nearly superimposed. It is unclear from this graph alone whether this is a quasi-periodic oscillation or chaotic. Further tests are needed.

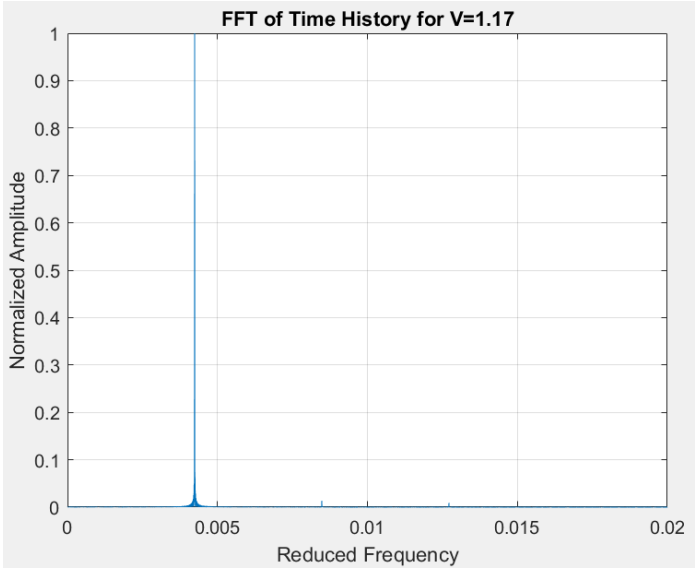

(a)

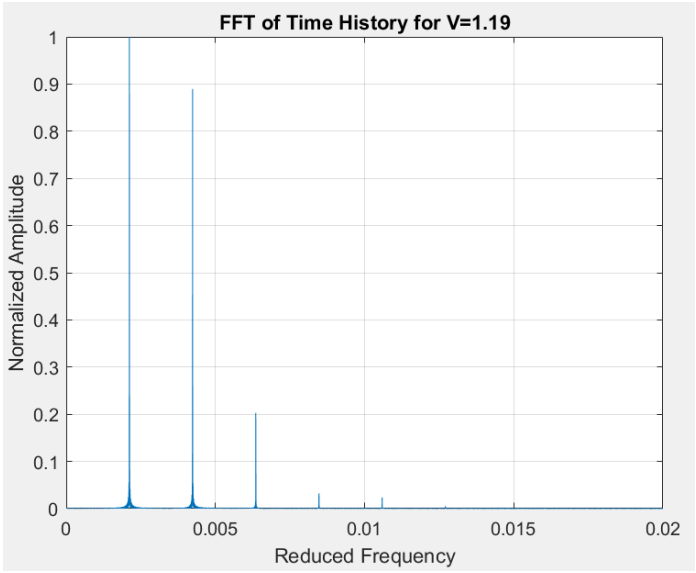

(b)

Figure 4.17: (a) A single peak suggests that a limit cycle oscillation (LCO) with a single closed loop exists at $V = 1.17$. (b) The presence of a few discrete superharmonic peaks suggest that period doubling took place and that there are no underlying frequencies that are unobserved in the phase plot diagram for $V = 1.19$.

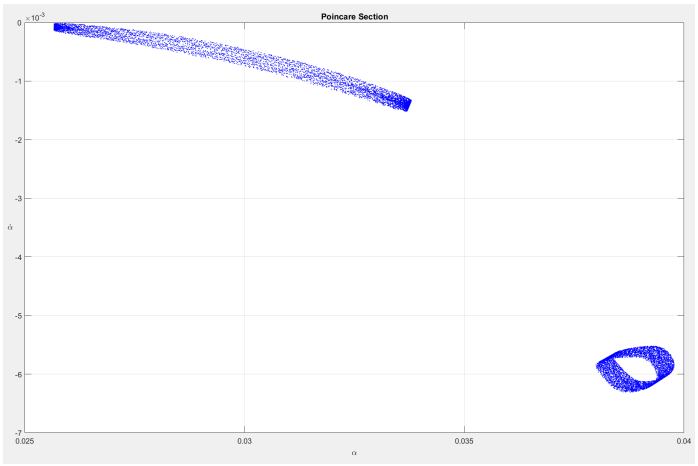

(a)

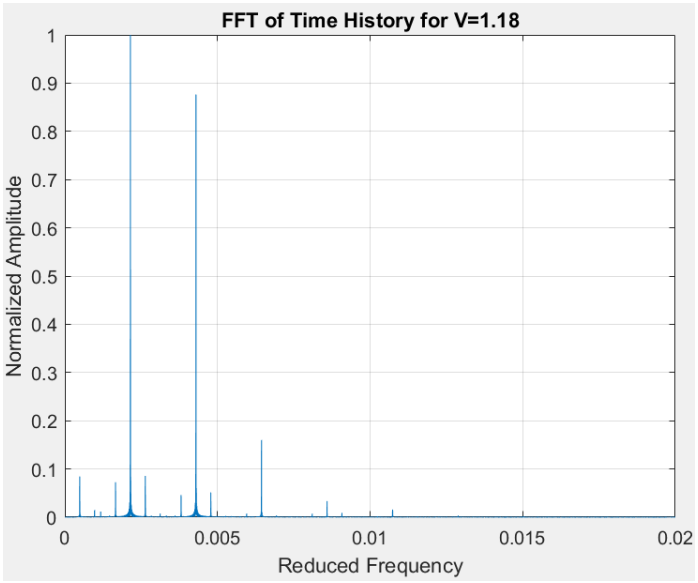

(b)

Figure 4.18: (a) The Poincaré section shows two clusters of points that resemble a closed loop orbit on the bottom right of the graph and a semi-closed loop orbit across the top left of the graph, both of which are indicators of quasi-periodic oscillations. (b) Quasi-periodicity is further confirmed by this FFT plot, which shows the presence of several distinct subharmonic peaks and other smaller impulsive peaks scattered across the plot.

In Figure 4.14, immediately after $V = 1.19$, the system once again exhibits chaos that continues until $V = 1.24$, when the system returns to being a stable limit cycle with two fixed points. This type of behavior with changing stability regions for changes in the velocities is strikingly similar to the behavior exhibited by the Mathieu Equation, which deals with time-dependent coefficients [117]. While we do not suggest that this may be the case for our system, the similarity in behavior is interesting. This is a topic that we wish to further investigate in future works.

The final studies that we conducted on the data associated with Region A involves examining how the results are affected when different solvers are used. Seeing the rapidly changing stability regions in the data near the nonlinear flutter boundary, we had good reason to believe that there may be stiffness present in our system of nonlinear differential equations. Our data presented here was obtained using a modified version of the `ode45` function as explained in Section 4.1.3. We decided to test this system at velocities near the nonlinear flutter boundary with the use of two other solvers to see how the results compare. We used the unmodified `ode45` function, a nonstiff solver, and the unmodified `ode15s` function, a stiff solver at three different velocities $V = 1.14$, $V = 1.17$, and $V = 1.19$. We also tested the use of the RK4 solver at $V = 1.17$ just to reinforce the idea of how much superior the `ode45` function is compared to a fixed step size solver like the RK4 solver.

The phase plots and time histories obtained using the three different solvers for $V = 1.14$ are provided in Figures 4.19 and 4.20. The phase plots reveal a fascinating finding. The modified `ode45` function with smaller error tolerances gives us a motionless solution with residual roundoff noise on the order of 10^{-11}, as shown in Figure 4.19a. However, the solutions obtained by using the unmodified `ode45` and `ode15s` functions show seemingly similar chaotic flutter being present at $V = 1.14$, as seen in Figures 4.19b and 4.19c. However, the respective time histories, in Figures 4.20b and 4.20c, are drastically different over the same range of time.

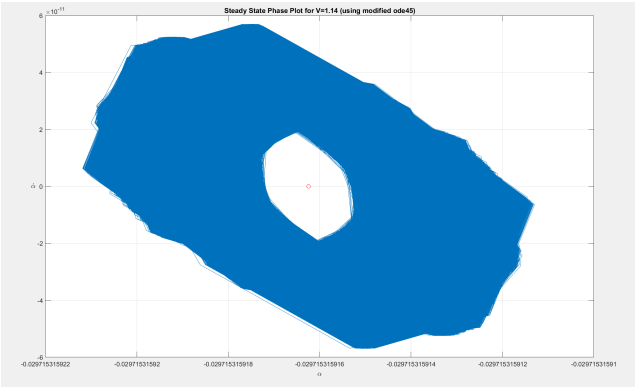

(a)

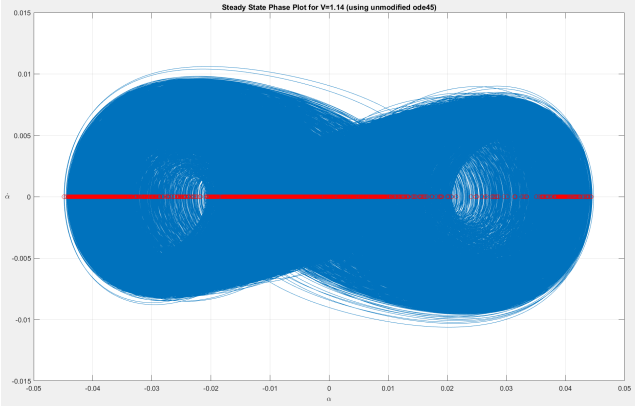

(b)

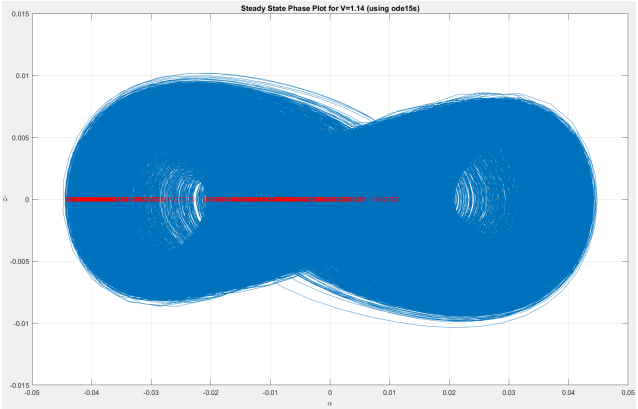

(c)

Figure 4.19: (a) Negligible residual roundoff noise is present in the steady state solution. This is physically interpreted as the system being motionless with pitch displacement of $-0.02972°$. (b) Chaos is observed when a nonstiff solver with looser error controls is used. (c) This solution corresponds to the use of a stiff solver. Its solution appears to be identical to the previous solution, however there are differences. One of the biggest difference here is that not all fixed points are accurate captured.

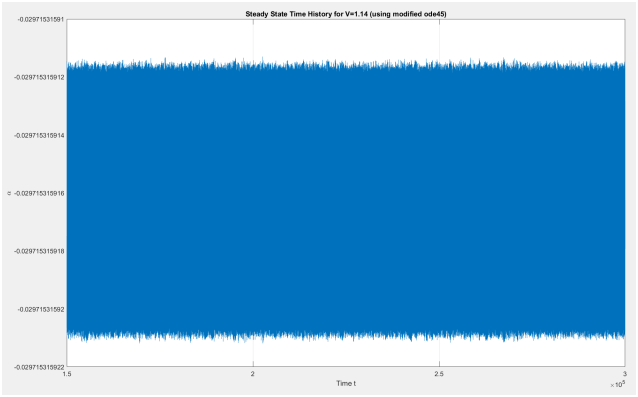

(a)

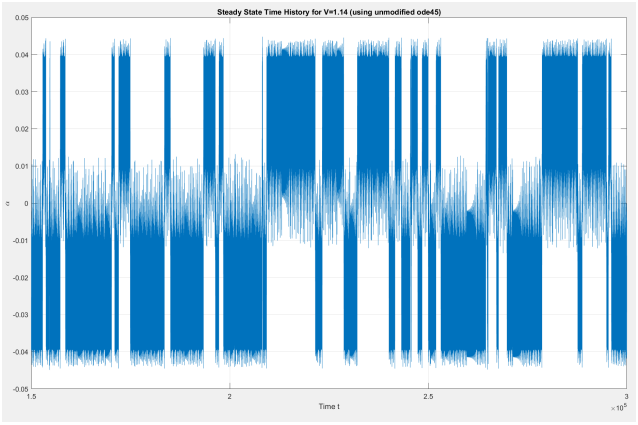

(b)

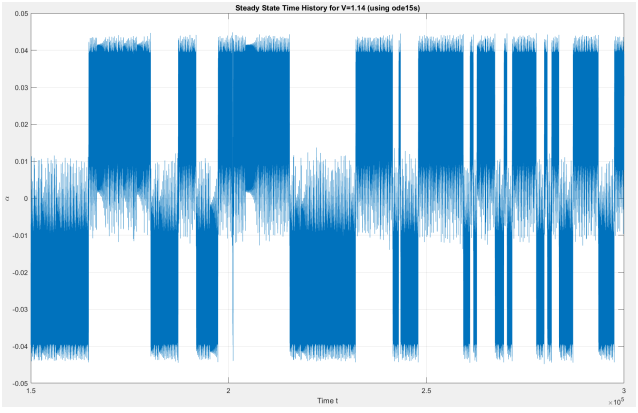

(c)

Figure 4.20: (a) Negligible residual roundoff noise is present on the order of 10^{-11}. (b) Chaotic time history is obtained with many random-like jumps and fluctuations in the oscillations. (c) A chaotic solution is obtained when a stiff solver is used, but the time history does not match with the previous solution that was obtained using a nonstiff solver.

These new results obtained by using different solvers highlight the importance of having solvers with appropriate bounded error controls. With the looser error tolerances, the solutions incorrectly showed chaos. In fact, when the unmodified `ode45` function is used, it predicts that the nonlinear flutter velocity is at $V = 1.13$ instead of what we found as the nonlinear flutter velocity, $V = 1.15$. While this difference in the computed flutter velocity is only separated by a magnitude of 0.02 on the dimensionless velocity scale, that difference can become physically significant when scaled for a large aircraft that can fly at speeds close to Mach 1.

We further tested stiffness by examining the system at $V = 1.17$ and $V = 1.19$, where we have the known stable solution shown in Figure 4.15. The unmodified `ode45` function gave accurate results in both cases. However, the stiff solver gave an inaccurate result for $V = 1.17$ and a choppy, non-smooth solution that was somewhat accurate for $V = 1.19$. The phase plots using the stiff solver are provided in Figures 4.21 and 4.22.

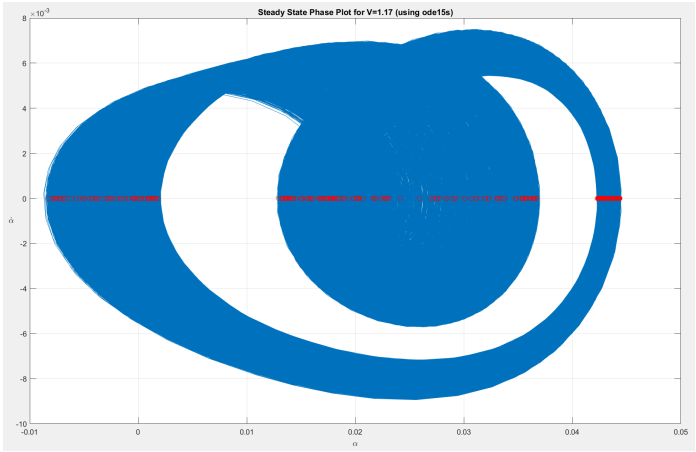

Figure 4.21: This phase plot shows an incorrect quasi-periodic behavior at $V = 1.17$ when using a stiff solver.

The computational times were recorded for each solver. The data is given in Table 4.2. We additionally performed a few tests with the RK4 solver at $V = 1.17$ to compare the efficiency and accuracy of the fixed step size solver with the efficiency and accuracy of variable step size solvers when dealing with strong nonlinearities. We

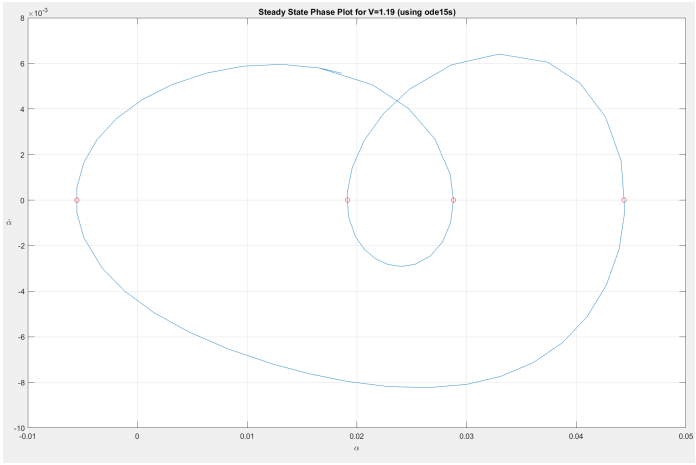

Figure 4.22: Despite the solution appearing to be correct, its resolution is poor, with the graph being non-smooth and choppy.

found that the RK4 solver would not converge to a solution unless its step size was $h \leq 0.01$. The solution that was produced with $h = 0.01$ was accurate but required 525.582 seconds, being over 17 times computationally slower than the modified `ode45` function.

	modified `ode45`	unmodified `ode45`	`ode15s`
$V = 1.14$	31.038 seconds	19.066 seconds	89.430 seconds
$V = 1.17$	28.578 seconds	18.531 seconds	68.334 seconds
$V = 2.3$	18.368 seconds	17.517 seconds	52.837 seconds

Table 4.2: Comparison of run times using three different solvers for the nonlinear aeroelastic system.

Unsurprisingly, the unmodified `ode45` function was the fastest solver. However, it ran into issues of accuracy at times, particularly near the nonlinear flutter boundary. Most surprising to us was that the stiff solver was both the slowest and least accurate solver. Despite this, we cannot conclusively rule out stiffness in our system since that would require further research, as explained in [109, 110]. We can conclude that considerations of error tolerances are significantly important and need to be addressed when performing numerical integration, especially with nonlinear systems. Such systems may be highly sensitive to variations in the numerical methodology implemented. This is a topic for future research in the field of nonlinear aeroelasticity.

Region B

As the system's velocity is increased between $V = 1.24$ and $V = 1.87$, the system's response remains a single closed loop limit cycle oscillation. The only change that occurs is that the amplitude of the oscillation increases for increasing velocities. In Figure 4.23, we provide two phase portraits for arbitrary velocities within the range of $V = 1.24$ and $V = 1.87$.

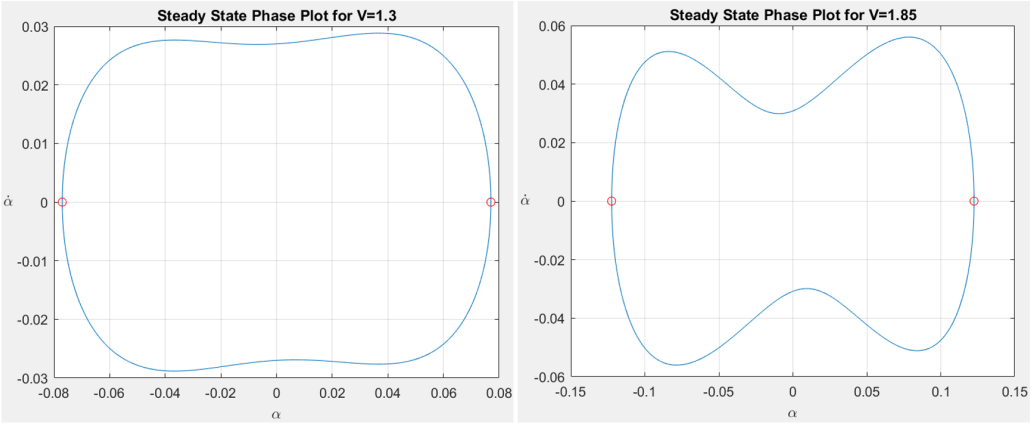

Figure 4.23: The phase portraits for $V = 1.30$ and 1.85 show that its evolution is headed towards a potential period doubling, as seen by the trajectories in the phase portrait showing a more pronounced curvature near the zero amplitude displacement values at $V = 1.85$ than at $V = 1.30$.

Immediately after $V = 1.87$, the system undergoes a jump phenomena, where the system response experiences both a jump in amplitude and a period doubling. This behavior is captured in the boxed Region B of the bifurcation diagram in Figure 4.8. The zoomed-in image of Region B is provided in Figure 4.24. What follows for $V > 1.88$ is a sequence of random-like solution "flipping", where the oscillations appear to flip about their horizontal axes with no particular pattern for certain values of V. This phenomena can be seen in the fixed points plotted in Figure 4.24, where some of the fixed points for $V > 1.88$ appear to be mirrored about the horizontal axis. For example, at $V = 1.89$, there are three negative valued fixed points; yet at $V = 1.90$, the negative fixed points become positive and vice-versa. When their phase

portraits are mapped, shown in Figure 4.25, the path mapped by the trajectories also appear as flipped and mirrored. This is the same phenomena that was observed by the system prior to experiencing flutter in Region A. The reasoning behind this is unexplained and requires further research.

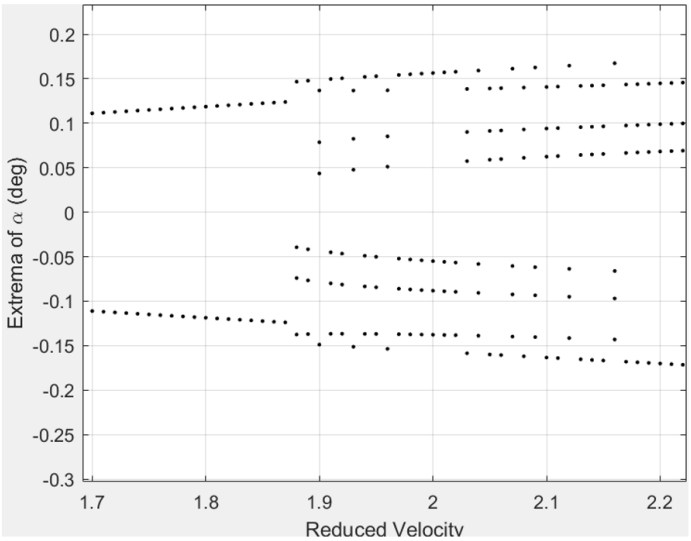

Figure 4.24: This zoomed-in image of Region B from Figure 4.8 shows a jump phenomena occurring at $V = 1.88$. After this, the fixed points are mapped in a mirrored manner about the horizontal axis for some of the velocity values.

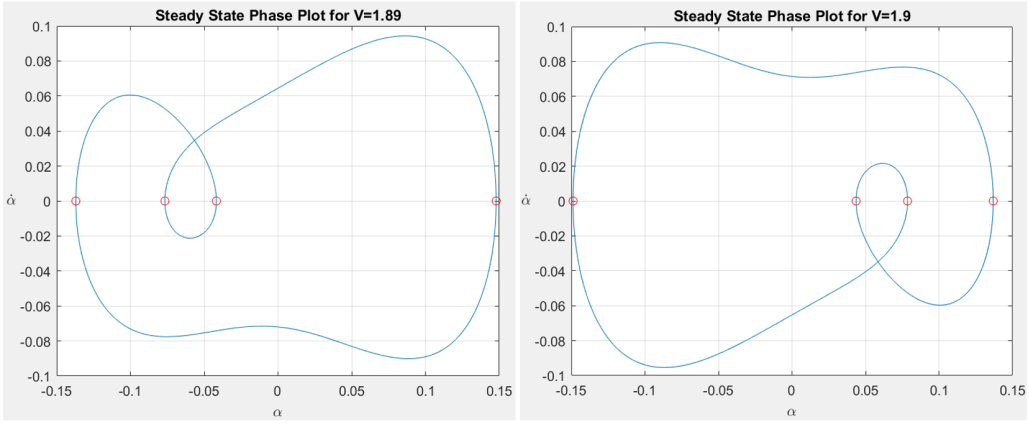

Figure 4.25: The mirroring phenomenon is seen in the phase portrait plots of two velocities that are close to each other, $V = 1.89$ on the left and $V = 1.90$ on the right.

Region C

As the velocity is further increased beyond $V = 2$, the amplitude response grows proportionally and the solutions continue to undergo flipping until $V = 2.77$. Once again, another period doubling occurs at that velocity. Recalling the discussion in Section 4.5, one of the routes to chaos is through repeated period doubling. This behavior holds true for our system. In Region C of the bifurcation diagram, shown in Figure 4.26, we see that the system finds its way towards chaos, by first experiencing period doubling and then quasi-periodicity.

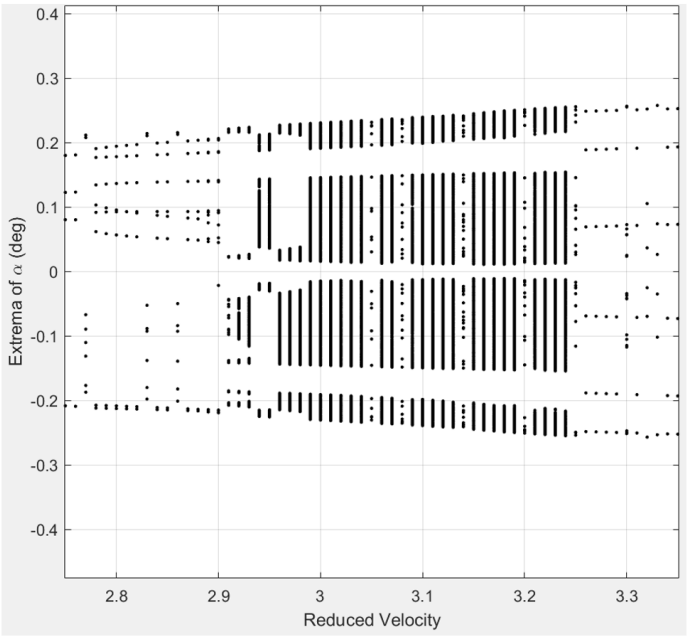

Figure 4.26: This zoomed-in image of Region C from Figure 4.8 shows further period doubling at $V = 2.77$, followed by quasiperiodic oscillations and then chaos for almost all velocities $2.96 \leq V \leq 3.24$. Then the system settles back into stable limit cycle oscillations.

The route towards chaos is mapped in Figure 4.27 by the phase portrait plots for increasing velocity. The FFTs of the systems at those velocities are given in Figure 4.28. From these graphs, the evolution of the system's response is better understood.

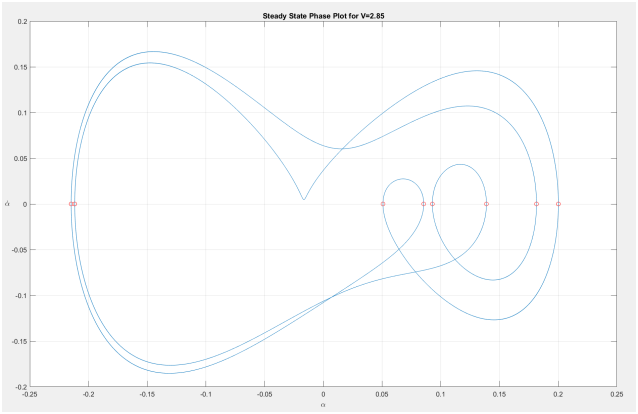

(a)

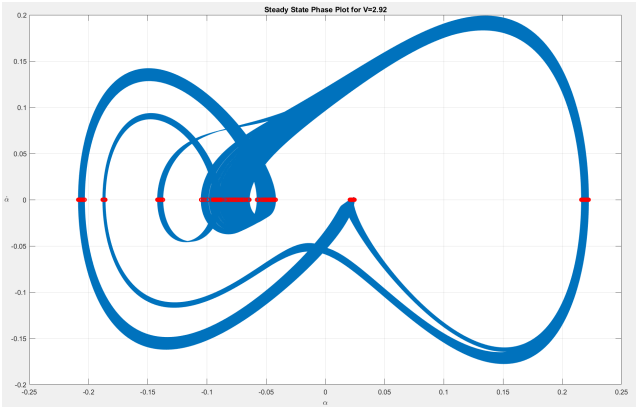

(b)

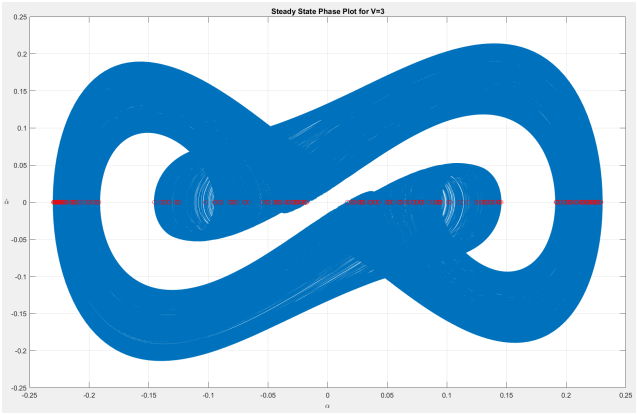

(c)

Figure 4.27: The evolution toward chaos is mapped, with increasing velocities showing more unstable behavior. (a) Periodic LCO is present at $V = 2.85$. This system appears to be headed towards period doubling. (b) At $V = 2.92$, the system encounters quasi-periodic behavior, which is seen by the trajectories not repeating their same return path in state space. (c) A chaotic solution appears at $V = 3.00$.

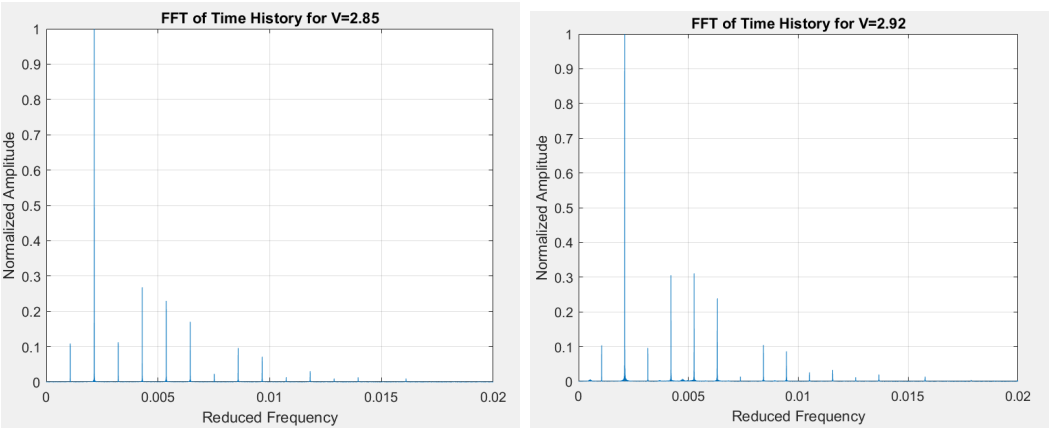

(a)

(b)

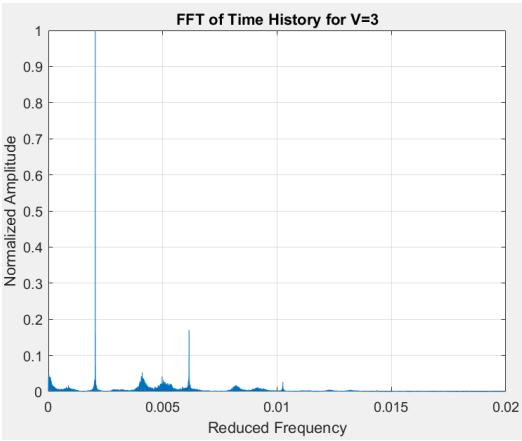

(c)

Figure 4.28: (a) Peaks are present at a small discrete number of frequencies. A small subharmonic peak is also seen to the left of the dominant frequency. (b) At $V = 2.92$, a large number of small narrow peaks begin to appear across the frequency spectrum. This is usually the case for quasi-periodic oscillations (c) Chaos is seen by the existence of a broad band spectrum of frequencies.

At $V = 2.85$, the system has already encountered multiple period doubling, which is seen by the presence of multiple closed and intersecting loops within the larger loops in Figure 4.27a. Its FFT, shown in Figure 4.28a, has a discrete number of tall, sharp peaks that indicate that the system is in a periodic oscillation regime. It also contains a small subharmonic peak below the dominant peak, indicating that some form instability is potentially present in these oscillations. However, the strength of the subharmonic is seen to be weak. At $V = 2.92$, in Figure 4.27b, the system enters quasi-periodic oscillations. The trajectories do not repeat the same return path as

it orbits in the state space. The quasi-periodicity claim is supported by the FFT plot in Figure 4.28b. A large number of small discrete peaks begin to appear. These smaller peaks affect the periodicity of the orbits. The lack of a broad band spectrum of frequencies suggests that chaos has not yet been reached. Thus, the oscillations are quasi-periodic. It should also be noted that the phase portrait for $V = 2.92$ is seen as being a flipped quasi-periodic map of the phase plot for $V = 2.85$. Finally, the system encounters chaos at $V = 3.00$, seen in Figure 4.27c. This is confirmed by the thick, broad band frequency spectrum in the FFT plot in Figure 4.28c.

Chaos is observed for almost all of the velocities between $2.96 \leq V \leq 3.24$. However, there are a few distinct velocities for which the system becomes semi-stable and experiences a repeating orbit with a large period that contains numerous self-intersecting loops. Chaos reappears in the system for the next velocity increment. The peak amplitude size of chaos grows with increasing velocity. Ultimately, the system's response structure slowly settles into a stable limit cycle for velocities larger than $V = 3.24$, seen by the discrete set of 4.26. The behavior exhibited in this region of the bifurcation diagram is similar to that seen in Region A, where the system experiences small stability regions within large velocity ranges experiencing chaos.

Below, we show the evolution out of chaos in Figure 4.29, where the phase plots for increasing velocities are given. Three velocities were selected. The first velocity is $V = 3.05$, where a repeating orbit with a large period appears, seen in Figure 4.29a. Determining its periodicity required looking at both FFT and the autocorrelation plots, shown in Figure 4.30. The FFT plot in Figure 4.30a shows many discrete peaks that are spread across the spectrum of frequencies in the plot, preventing conclusive determination of periodicity. However, the autocorrelation plot in Figure 4.30b shows a consistent pattern that maintains its form over the entire range of time, which allows us to conclude the existence of a long-lived periodic orbit at $V = 3.05$.

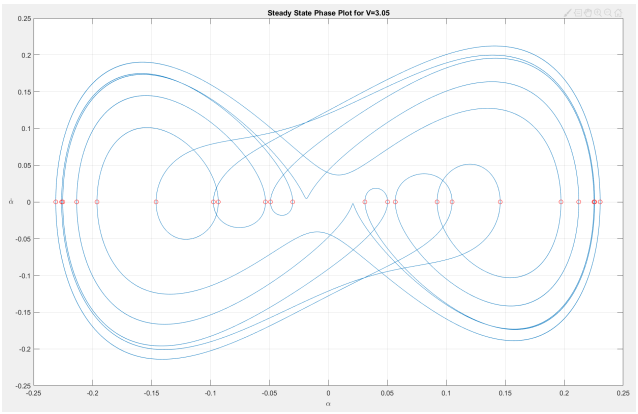

(a)

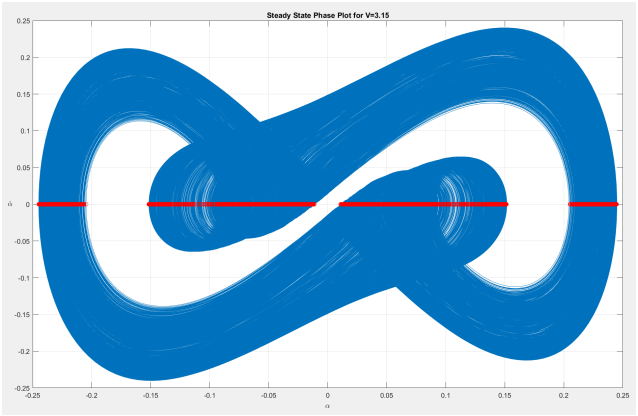

(b)

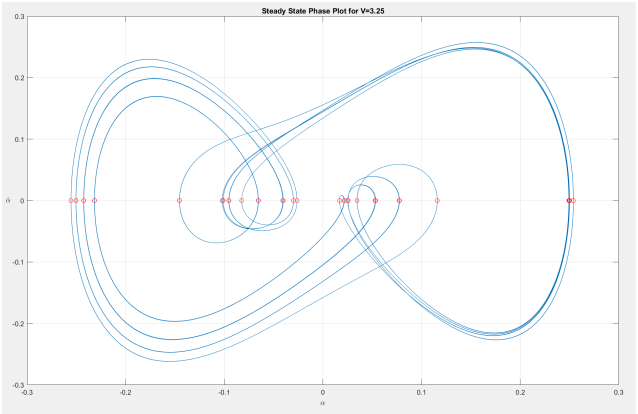

(c)

Figure 4.29: (a) At $V = 3.05$, chaos vanishes and a semi-stable, long-lived periodic orbit appears. (b) At $V = 3.15$, chaos returns. (c) At $V = 3.25$, the system begins to leave chaos but still has strong underlying subharmonic behavior in its response structure.

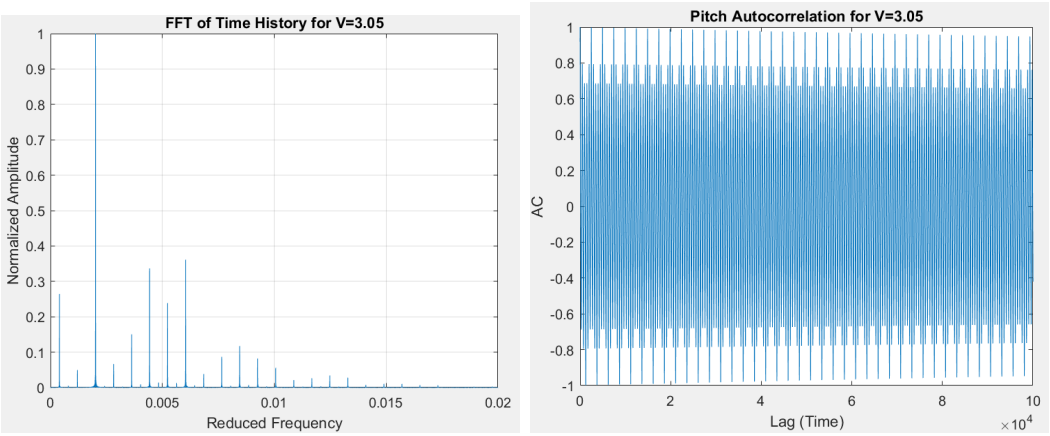

(a) (b)

Figure 4.30: (a) The FFT plot shows the presence of a number of discrete peaks spread across the entire spectrum of frequencies. Determining periodicity from this plot alone is difficult. (b) The autocorrelation plot validates that the oscillations are periodic due to the consistent, and largely non-decaying, patterns observed.

From the phase portrait plot in Figure 4.29b, we can see that there appears to be chaos occurring at $V = 3.15$ in same manner as we observed in Figure 4.27c. For this case, we will show the existence of chaos without using its FFT. We will only use the autocorrelation plot, Poincaré section, and the LLE plot. All three are given in Figure 4.31. First, the autocorrelation function in Figure 4.31a displays a rapidly decaying plot that approaches zero. This type of trend in the autocorrelation strongly suggests the presence of chaos. The Poincaré section in Figure 4.31c maps a cluster of disorderly distributed points that are plotted across the entire phase portrait plot. This a strong indicator of chaos. Finally, the LLE plot, given in Figure 4.31b, graphs all of the Lyapunov exponents as strongly positive. While there are some fluctuations, these variations become less pronounced with increasing time and the graph becomes steady with increasing time. This is a strong indication of chaos, since it means that two nearby initial conditions for this system diverge away from each other exponentially fast at $V = 3.15$. From these plots, we can conclusively state that chaos exists at $V = 3.15$.

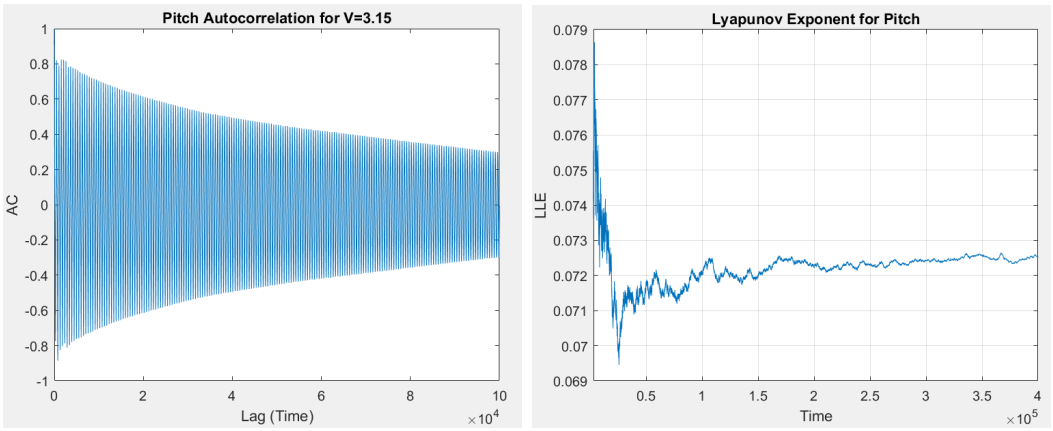

(a) (b)

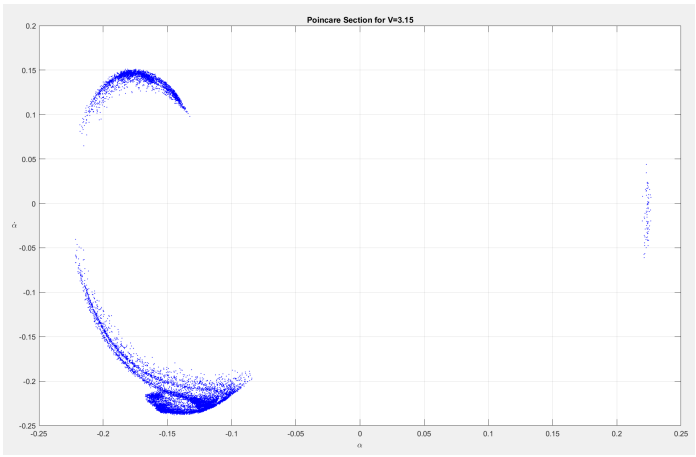

(c)

Figure 4.31: (a) The autocorrelation function rapidly trends to zero with increasing time, indicating chaos. (b) The LLE plot, while exhibiting some fluctuations, is strongly positive into later time. It can be concluded from this plot that the system is experiencing chaos. (c) The Poincaré section show a wide spread of points that have no structured shape to them. This is also a very strong indication of chaos.

The system exits chaos at $V = 3.25$, as the phase portrait in Figure 4.29c shows that it is not immediately clear what type of behavior this phase plot has mapped. It appears quasi-periodic but clearly has some trajectories that follow the same return path in its state space. A closer look at the FFT and autocorrelation plots show the strong presence of subharmonic oscillations. The FFT, shown in Figure 4.32a, has many discrete peaks scattered across the entire band of frequencies. The strength of these peaks is seen to be quite large, particularly for the subharmonic peaks. This can

explain the unique nature of the oscillations that are seen in this system's response at $V = 3.25$. This response appears to be dominated by multiple frequencies that lead to its "almost-periodic" behavior. This near periodicity is seen in the autocorrelation function plotted in Figure 4.32b. The plot appears to have a consistent pattern and shape in its oscillations, but diminishes in magnitude as the time lag increases. We are able to see that as the system exits chaos, many of the frequencies that dominate the oscillatory response during chaos significantly diminish until a periodic behavior reemerges, as seen in the tail end of the bifurcation diagram in Figure 4.8.

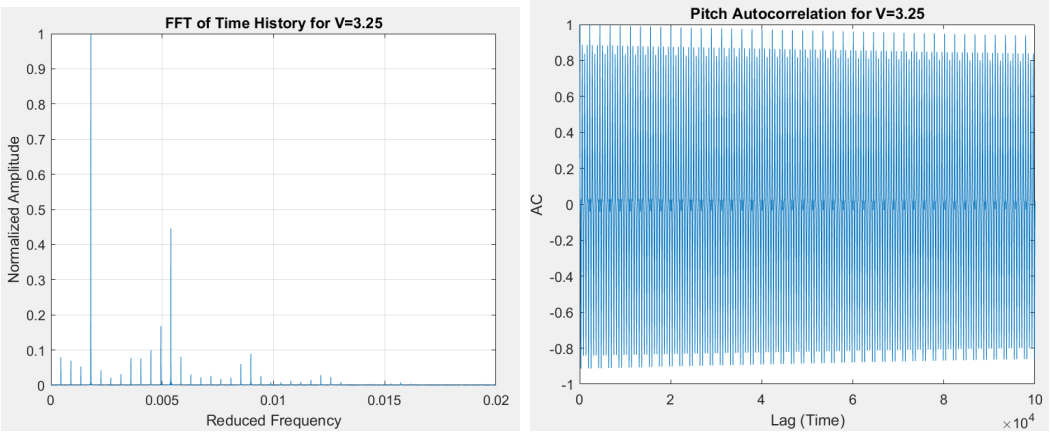

(a) (b)

Figure 4.32: (a) There is a strong presence of subharmonics, seen by the multiple peaks at several frequencies below the dominant frequency. There are also a large number of small peaks that are spread across the spectrum of frequencies. These small peaks and subharmonics have a strong effect on how this system oscillates at $V = 3.25$. (b) The autocorrelation plot suggests that there may be an underlying periodic phenomena that is being overpowered by subharmonics. There are clear patterns autocorrelation plot, however there is also a slight decay in these oscillations with increasing time lag.

Region D

The final portion of interest in the bifurcation diagram is in Region D. The system's response becomes a stable limit cycle whose amplitude grows with increasing velocity. The stability of the system's response can be seen by examining its time his-

tory at particular velocity. Here, we chose to examine the largest velocity for which we performed numerical integration, $V = 4.2$. Its phase plot, shown in Figure 4.33, shows a pattern of continuously repeating trajectories that loop inside itself twice before completing a larger orbit in the phase portrait. Its FFT, given in Figure 4.34a, shows a few distinct peaks at only the frequencies that govern the system's oscillatory response, suggesting a stable solution. Numerically, the stability of this response can be determined by using the LLE plot, given in Figure 4.34b. We find that the LLE quickly becomes negative and exhibits limiting behavior that trends towards a negative valued Lyapunov exponent. This a strong sign of a stable response, since it implies that two nearby initial conditions will collapse into the same orbit over a large range of time.

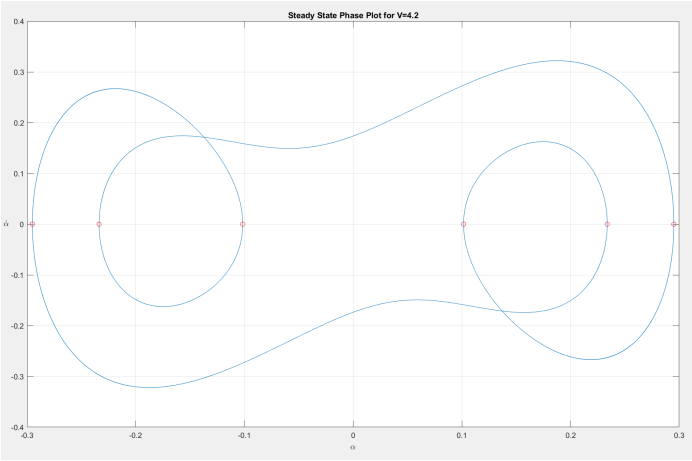

Figure 4.33: This is a stable limit cycle containing two smaller loops that are enclosed within.

By studying this last region in the bifurcation diagram, we have fully examined and understood the manner in which this highly nonlinear system responds. We have gained good insight into the physical behavior of an airfoil with this type of nonlinear stiffness. This deep dive into the bifurcation diagram allows us to proceed into our next set of nonlinearities that we studied: the best fit cubic models.

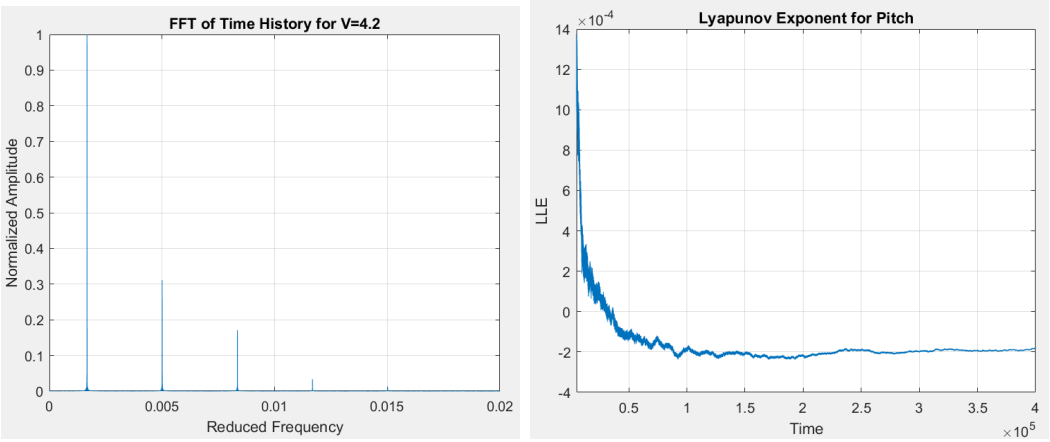

(a) (b)

Figure 4.34: (a) There are only a discrete number of frequencies with narrow peak, suggesting periodicity in the response. (b) The negative Lyapunov exponent indicates that the system response is very stable.

4.7.2 Best Fit Cubic Models

One of the main goals of this thesis is to study the application of the nonlinear models with real data on free play. According to Chen et al. [8], the Federal Aviation Administration and the United States military require that all moving control surfaces cannot have free play that exceeds ± 0.017 degrees. However, this is a requirement that is nearly impossible to meet in all aircraft. They found that an F-16 fighter jet was operating with over six times the allowable free play amount and never experienced any instabilities in the form of limit cycle oscillations. These aircraft are much more closely maintained than aircraft used in general aviation. With that in mind, we can only speculate how much worse this problem is for lesser maintained aircraft. This motivated us to examine the use of best fit cubic nonlinear stiffness models for a variety of free play amounts much larger than ± 0.017 degrees. The cubic models were best fit between $-3^\circ \leq \alpha \leq 3^\circ$, a range that we established using trial and error, as explained in Section 3.4.

In this thesis, we used an idealized piecewise model of free play that is mathematically defined in Equation 3.54. The nonlinear stiffness is given by the use of a

Heaviside function in the piecewise model, where $M(\theta) = (\theta + \delta) - (\theta + \delta)\, H\,(t + \delta) + (\theta - \delta)\, H\,(t - \delta)$. The variable δ is used to define the free play amount that we measure from the neutral position of the control surface, with $\alpha = 0$. Then, we used `polyfit`, a built-in `MATLAB` function, to best fit the cubic model free play, given in Equation 3.55, with the piecewise model of free play. As an example, we show in Figure 4.35 how this function looks when this procedure is carried out for a free play value of $\delta = 1°$.

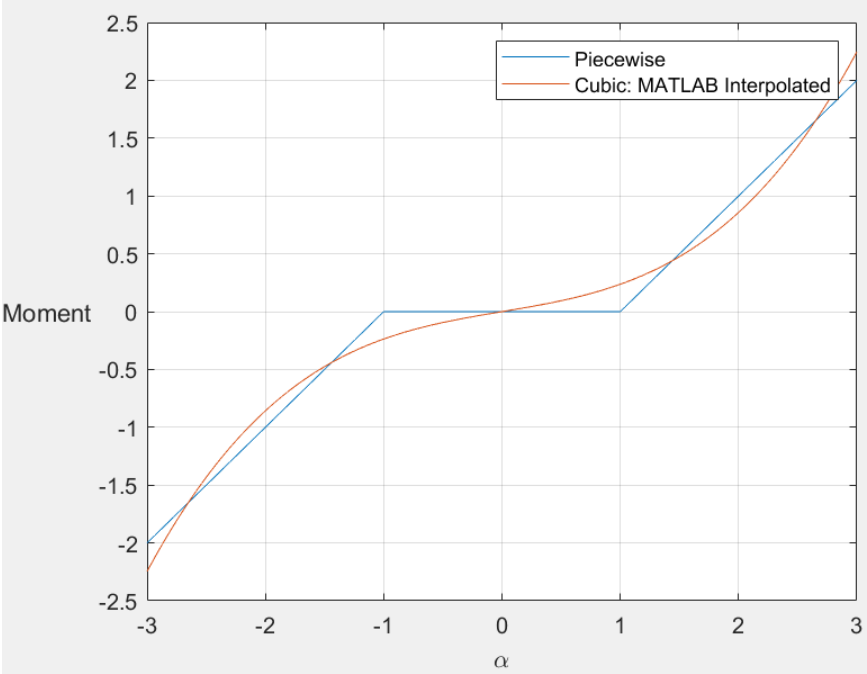

Figure 4.35: A best fit cubic approximation of the piecewise model with free play of $\pm 1°$ is given here. The cubic model gives a good fit in the center of the flat spot and along the two linear portions that branch away.

In Figure 4.35, we see that the cubic function has difficulty mapping closely to the sharp corner of the piecewise function. In this case, the best fit values of the constants in Equation 3.55 determined by `MATLAB` were $C_1 = 0.17284$ and $C_3 = 0.06401$. We repeated this type of approach for ten different values of free play to study ten different cubic models for our nonlinear aeroelastic system. These values of free play are given in Table 4.3, along with the values of C_1 and C_3 that were

determined using MATLAB for the respective values of free play.

Free Play	C_1	C_3
0.034°	0.96812	0.00275
0.05°	0.95313	0.00404
0.1°	0.90636	0.00808
0.2°	0.81342	0.01605
0.3°	0.72186	0.02382
0.4°	0.63235	0.03126
0.5°	0.54555	0.03828
0.6°	0.46208	0.04479
0.75°	0.34442	0.05340
1°	0.17284	0.06401

Table 4.3: Ten different values of free play were adopted. Each new set of values for C_1 and C_3 give us a new nonlinear model to work with.

We selected values for free play that began at $\delta = 0.034°$. This value was chosen because it is twice the amount of free play that is allowed in the aviation industry and, according to Chen et al. [8], such a free play magnitude is commonplace with most aircraft. Mathematically, we found that for smaller values of free play, the cubic approximation became nearly linear and any results that were obtained were almost identical with those of the linear system. Therefore, our first nonlinear cubic model was best fitted to with free play value of 0.034°. We chose the nine other somewhat evenly free play spaced values up to $\delta = 1°$. While it is unlikely to observe an amount of free play as extreme as $\pm 1°$ in real life, we decided to still examine such a system for theoretical purposes.

For these ten different nonlinear systems, we conducted the same numerical analyses that we discussed in the previous section. We generated ten different bifurcation diagrams and recorded the values for nonlinear flutter velocity in each case. From these plots, we were able to create a first of its kind 3-D bifurcation diagram plot, shown in Figure 4.36. This graph plots the evolution of the system's response structure for increasing amounts of free play.

There are several qualitative aspects of the response structure that immedi-

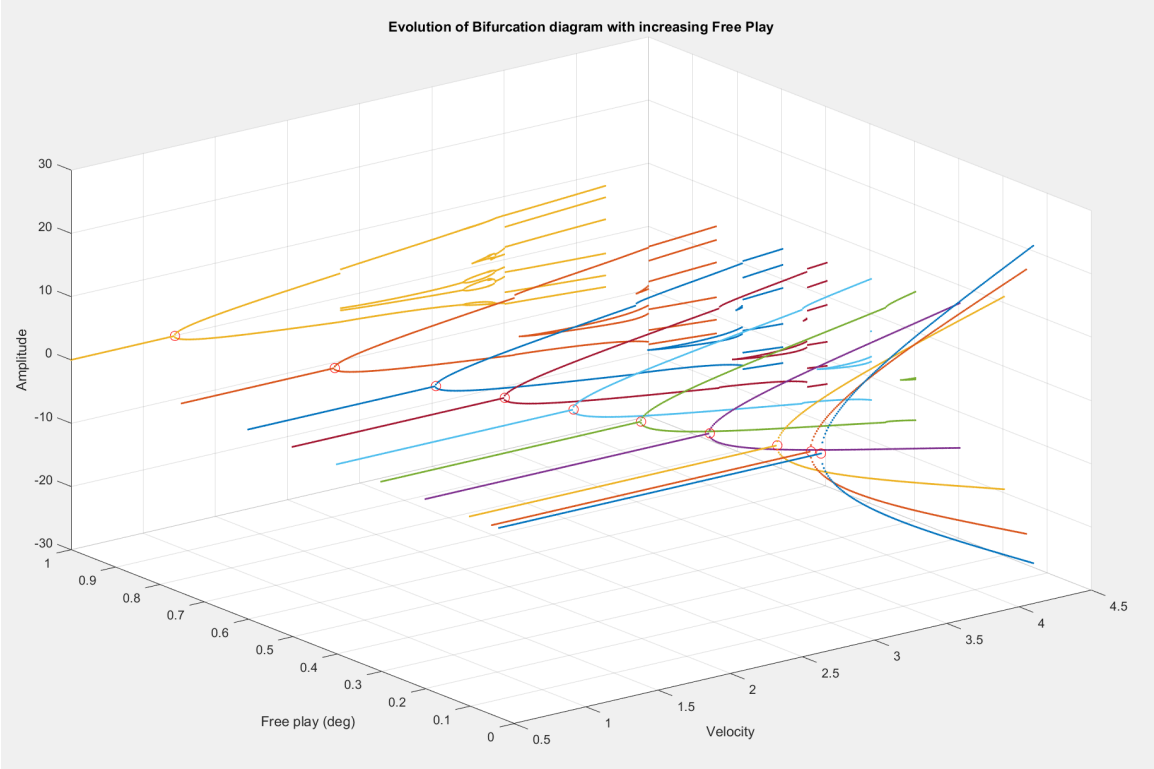

Figure 4.36: The complete evolution of the system's response structure can be seen in this 3-D graph. The red circles on the graph are the locations in the 3-D space where the flutter occurs.

ately jump out from the 3-D plot in Figure 4.36. First, we see that the nonlinear flutter velocity is a function of free play. If we look at the graph from the top view, we are able to see an apparent linear relationship between the free play amount and the nonlinear flutter velocity. This is shown in Figure 4.37. This type of relationship is likely a property of the cubic nonlinearity. We cannot conclude if this linear relationship would still be present for larger values of free play. From the front view of Figure 4.36, we are able to see that the system's amplitude response decays rapidly fast for increasing values of free play. This is shown in Figure 4.38. We notice that the system response continues to exist well past the linear flutter velocity for all types of cubic nonlinearity, regardless of its strength.

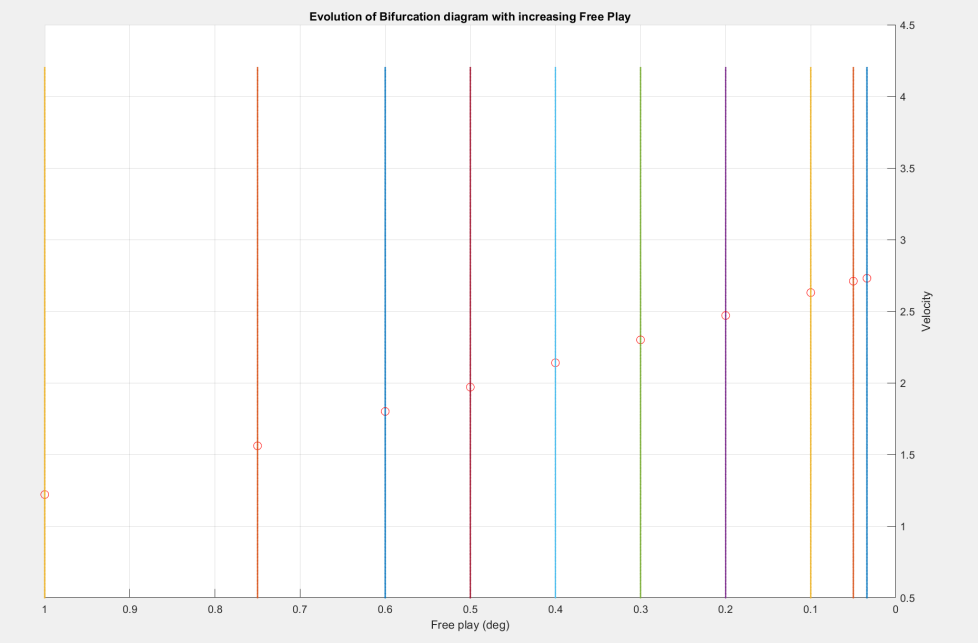

Figure 4.37: The red circles indicate the location of when flutter is encountered. An apparent linear relationship appears from this top view of the 3-D plot in Figure 4.36. The bottom axis should be read from right to left.

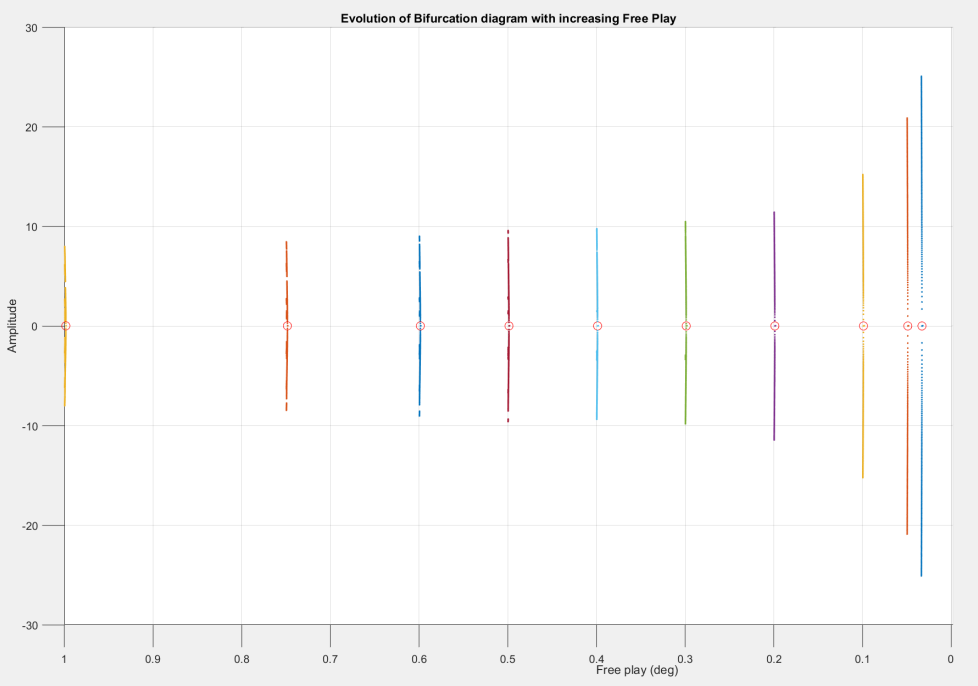

Figure 4.38: Reading the bottom axis from right to left, this graph shows the rapid decay in the peak amplitude response for increasing amount of free play.

From the 3-D graph in Figure 4.36, we also see that the more interesting dynamical behavior, such as jump phenomena, period doubling, and the appearance of new bifurcation branches, are only seen when the nonlinearity becomes stronger for larger amounts of free play. What should be noted is that chaos is *not* seen anywhere in any of the bifurcation diagrams. In comparison to the previous section where the cubic nonlinearity was significantly stronger, the response structure of the best fit cubic nonlinearities is mild. This leads us to the conclusion that there are certain specific conditions that are necessary for the cubic nonlinearity for the system to produce chaos. This type of behavior associated with the cubic nonlinearity can be best understood by noticing the similarity of this nonlinear system with the Duffing oscillator, where there is a cubic component to the stiffness. For the right combination of cubic stiffness and forcing function, the Duffing oscillator can exhibit chaos. For other conditions, different instabilities can be found, as well as the system response settling to zero. More can be read about the Duffing oscillator in references [116, 106]. For our system, chaos and other unique types of nonlinear instabilities are not always guaranteed for all types of cubic nonlinearities.

4.8 Results: Piecewise Free Play Models

For this thesis, we conducted minimal examinations of piecewise nonlinear models to gain a preliminary understanding of how the behavior of an aeroelastic system with this type of nonlinearity model compares with that of a system with a cubic nonlinearity. We tested a piecewise nonlinear model with free play of $\delta = 0.3°$ at four different velocities, $V = 1$, $V = 1.9$, $V = 2.75$, and $V = 2.8$. These results were then compared with best fit cubic model data for the same amount of free play. We used the *unmodified* `ode45` function, for its fast computation speed, to obtain the results given in Figure 4.39.

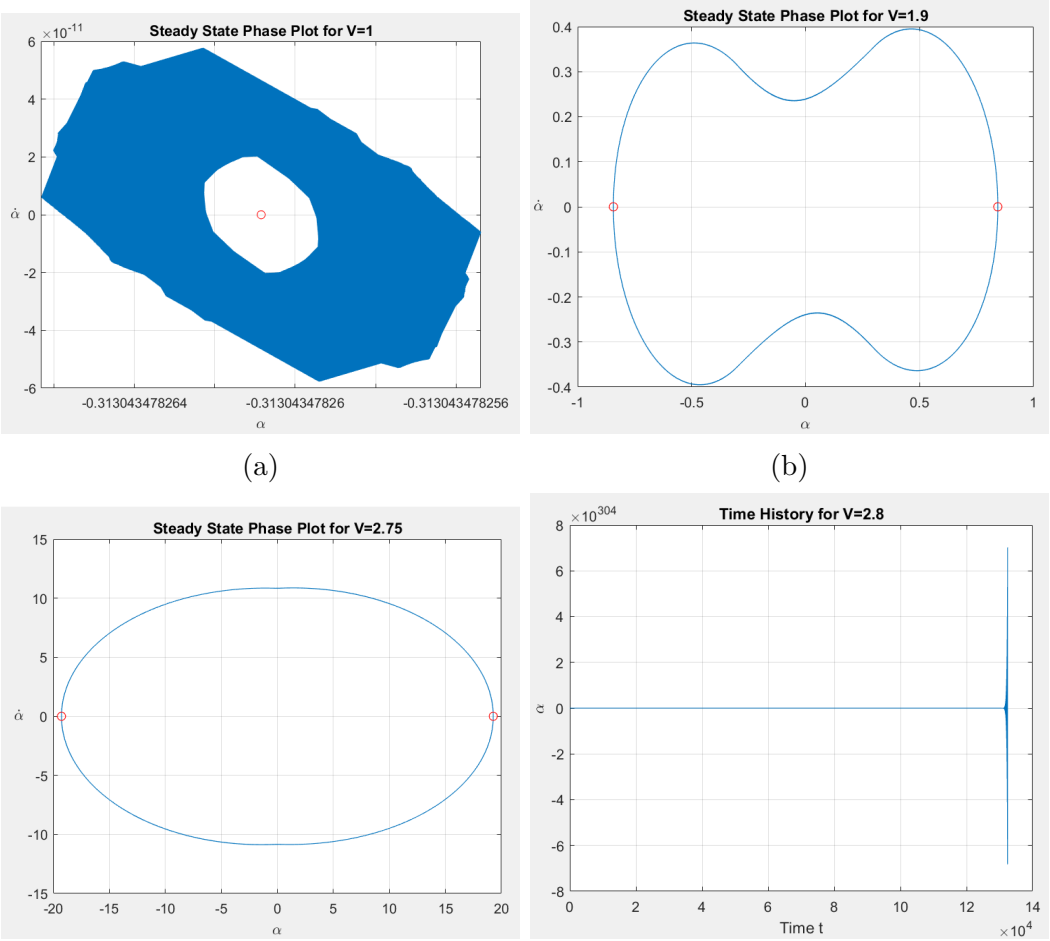

(a) (b)

(c) (d)

Figure 4.39: (a) This phase portrait shows that the system settles to zero displacement at $V = 1$. (b) For $V = 1.9$, the system has bifurcated into multiple solutions with two fixed points. This is an indication of aeroelastic instability. (c) A large amplitude limit cycle is seen to occur at $V = 2.75$. (d) The system diverges to infinite amplitude response at $V = 2.8$. The time history plot reaches the maximum value that `MATLAB` can compute.

At $V = 1$, the system settles to zero displacement. The phase portrait, shown in Figure 4.39a, gives the plot of the converged system with the residual roundoff noise on the order of 10^{-11}, as seen previously in Sections 4.4 and 4.7 with the other linear and nonlinear systems. At $V = 1.9$, this system is seen to have reached an aeroelastic instability. In its phase portrait in Figure 4.39b, a period-1 limit cycle is seen with two fixed points, indicating that the system is past its flutter velocity. In comparison to the best fit cubic nonlinearity, that system is seen to reach flutter at $V \approx 2.3$.

These piecewise nonlinearities cause the system to encounter flutter well before the cubic nonlinearity reaches flutter. This is important to note because it suggests that the cubic nonlinear approximation of free play possibly needs more refinement than how it is currently defined.

Continuing further, at $V = 2.75$, the piecewise nonlinearity gives us a large amplitude limit cycle response, as seen in the phase plot given in Figure 4.39c. Its amplitude range is from approximately $-20°$ to $+20°$. When compared with the cubic system at that same velocity, we find that the cubic system's response amplitude range is only approximately from $-4°$ to $+4°$. This large difference is the predicted response structure and can mean that one, if not both models, need to be improved to better reflect the true nonlinear stiffness of a control surface with free play.

Lastly, at $V = 2.8$, the system fails to converge to a steady state solution. It diverges with its amplitudes increasing towards infinite response, as seen in the time history given in Figure 4.39d. We speculate that this is likely due to how the piecewise function is mathematically defined. It is almost entirely a linear system with a flat spot in its center. Therefore, we speculate that the piecewise model will fail to converge for all velocities larger than the linear flutter velocity for any given free play amount. This can be seen as a drawback of the piecewise model. In comparison, we showed in the previous section that the cubic nonlinear system will produce a converged response for any type of cubic nonlinearity, well past the linear flutter velocity.

There were other drawbacks with the use of the piecewise model that we encountered. First, the system took a very long time to produce solutions. In Table 4.4, we show the times that were needed for the computation to take place. In some cases, a factor of 20 more time is required than for computation for the cubic nonlinear system, where we used modified versions of the `ode45` function that is not as fast as its unmodified version. We believe that this could be a sign that there is stiffness

present in the system over the entire range of velocities that we examined. In the future work, we could explore the possibility of using a stiff solver.

	Computation Time
$V = 1.00$	429.638 seconds
$V = 1.90$	831.392 seconds
$V = 2.75$	1249.160 seconds
$V = 2.80$	529.002 seconds

Table 4.4: The excessive computational time needed to produce a solution suggests that stiffness may be present in the system over the full range of velocities.

4.9 Probabilistic Modeling

The final major goal of this thesis was to develop an initial probabilistic framework to predict the likelihood of encountering aeroelastic instability or flutter when cubic nonlinear systems are present. We developed a model that would give a quantitative measure of the probability of flutter based on the aircraft's cruise velocity and the free play amount at any given time. Let's define X as the random variable for the aircraft cruise velocity and Y as the random variable for the free play amount. We chose X to be defined by a triangular distribution sake of simplicity. According to FAA AC-25.335-lA [118], the design cruise speed, V_C, of an aircraft should not exceed 80% of the aircraft's design dive speed, V_D. The FAA also states that the aeroelastic stability envelope must be at least 15% larger than the design dive speed [4, 5]. For the sake of demonstration, we therefore set the design dive speed in our model to be at 15% below the linear flutter velocity, $V_D = V_f/1.15$.

The triangular probability distribution function is [119],

$$F_X(x) = \begin{cases} \frac{(x-a)^2}{(b-a)(c-a)} & \text{for } a \leq x \leq c \\ 1 - \frac{(b-x)^2}{(b-a)(b-c)} & \text{for } c < x \leq b \\ 0 & \text{for } x < a,\ x > b, \end{cases} \tag{4.3}$$

where $c \in [a, b]$ and is the mode of the distribution. Choosing the constant values for $a,\ b,\ c$ required some understanding about the variabilities in cruise flight. According to the electronic aerospace repository SKYbrary [120], aircraft tend to fly at speeds below their designed cruise speed for a number of controlled and uncontrolled reasons, including saving fuel and external environmental factors. In some cases, it is not uncommon that an aircraft flies slight faster than its cruise speed if the conditions are correct. Keeping these sources of variabilities in mind, we chose $a = (0.7)(V_D)$, $b = (0.85)(V_D)$, and $c = (0.8)(V_D)$.

The second variable Y is the free play amount. We used a gamma distribution to model its probability because it has wide engineering reliability application. The gamma distribution also has the unique property of having its input variable being nonnegative. In our case, the input variable is the amount of free play, a value that cannot be negative. The distribution function for the gamma distribution is given by [117]

$$F_Y(y) = \int_0^Y \frac{\theta}{\Gamma(k)} (\theta y)^{k-1} e^{-\theta y} dy, \quad \text{for } y \geq 0, \tag{4.4}$$

where $k > 0$ is the shape parameter and $\theta > 0$ is the scale parameter. The mean value is $\mu_Y = k\theta$ [121]. By carefully selecting $k = 0.136$ and $\theta = 0.25$, we were able to set the mean, $\mu_Y = 0.034$, to bisect the distribution at the 80% probability mark. This created a Pareto type distribution which means that the probability of an aircraft having free play smaller than $0.034°$ is $P(Y \leq 0.034) = 80\%$. This also allows for higher and more extreme values of free play to see an extremely low, rare probability of occurrence. For example, with this model, the probability of an aircraft having free play larger than $1°$ is evaluated to be 0.0678%. In Figure 4.40, we provide both distribution functions plotted for 10^5 random random probability values.

The probabilistic modeling for free play still requires one more component that we have not considered until now. Free play is a function of time. It has been well documented that an operating aircraft will see free play that will worsen and accelerate

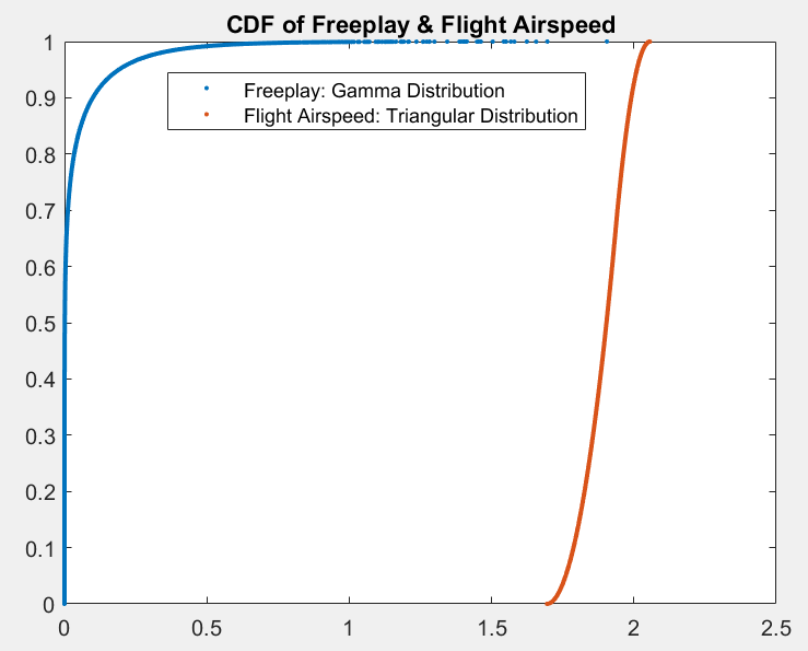

Figure 4.40: The gamma distribution is shown by the blue dots and the triangular distribution is given by the red dots.

with time [122]. This means that Y has to become a stochastic variable that is able to capture this accelerating wear phenomenon with increasing time, leading to larger free play. However, every aircraft has a maintenance planning document that determines the maintenance schedule for checking free play and lubricating or replacing parts. We found that American Airlines at one point had their Boeing 737 airplanes on a maintenance cycle of 5000 flight hours [123]. Assuming that the only time that free play is checked is during a maintenance schedule, and that all free play is reset to zero after a maintenance cycle, we can develop a clever, yet simple, stochastic model for free play. We defined the random process governing free play by

$$Y(t) = A \times \left(\frac{\exp\left(t/5000\right) - 1}{\exp(1) - 1} \right), \tag{4.5}$$

where A is a random amplification parameter with gamma probability distribution function, where $k = 0.136$ and $\theta = 0.25$. In Figure 4.41, we show 50 random realizations of this stochastic process. Note, Equation 4.5 is non-stationary.

At this point, we are ready to create our probabilistic model to quantify the

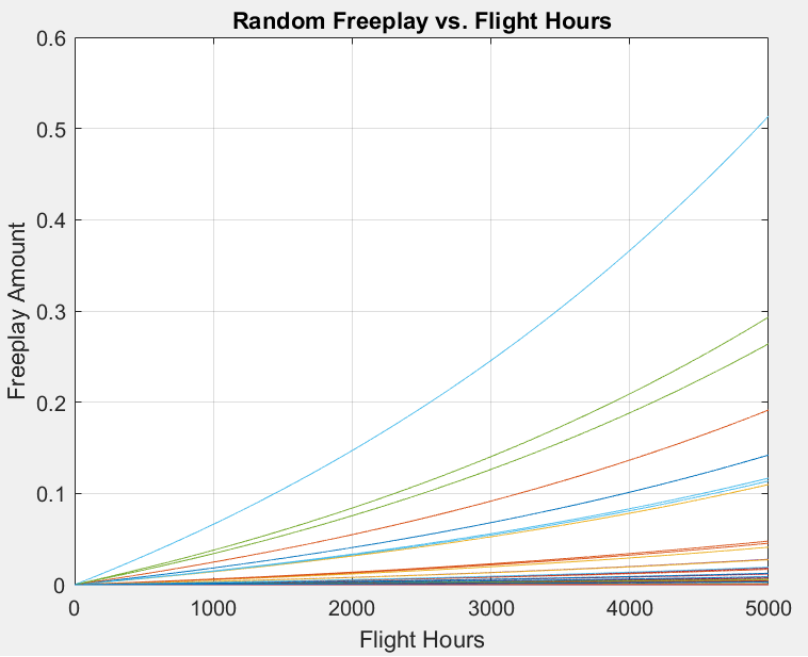

Figure 4.41: This graph show 50 random realizations of how free play can evolve with increasing flight hours. The different colors help differentiate the lines

probability of encountering flutter for an aircraft flying at a cruise airspeed of X with t flight hours logged since its previous maintenance cycle, and Y amount of free play. Assuming that the variables X and Y are statistically independent, we define the joint probability of this model as

$$P(X \leq x, Y(t) \leq y) = P(X \leq x)P(Y(t) \leq y). \tag{4.6}$$

Using Monte Carlo simulation with $10,000$ sample points for n random flight hours realizations, we were able to create n 2-D density plots that show this probability of flutter using a colormap index. Four such plots are shown in Figure 4.42. Furthermore, we created the 3-D probability density function plot (PDF) for our model, shown in Figure 4.43. It is interesting to note that with increasing time, the PDF evolves and the tail strength of the gamma function becomes more pronounced.

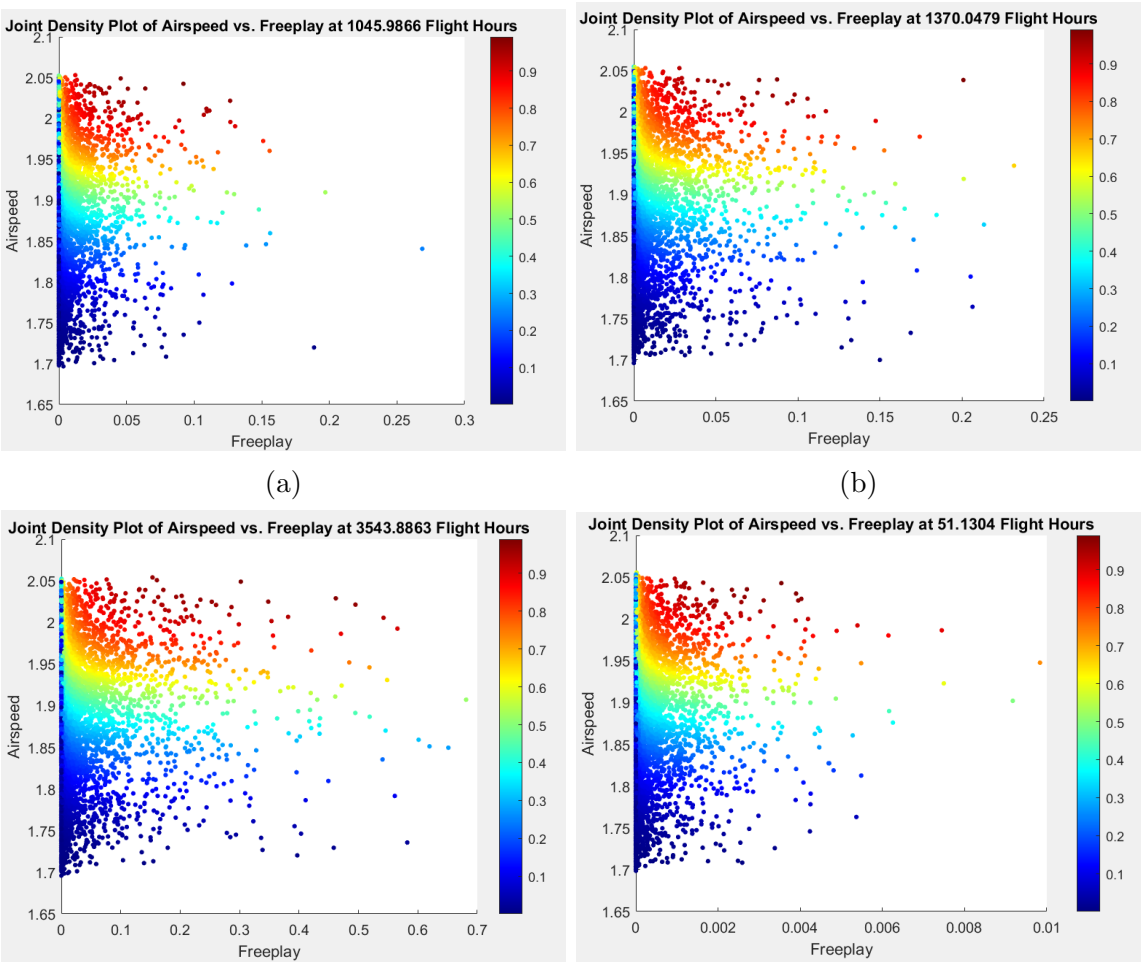

(a) (b)

(c) (d)

Figure 4.42: Four different Monte Carlo simulations are shown for randomly selected values of flight hour time.

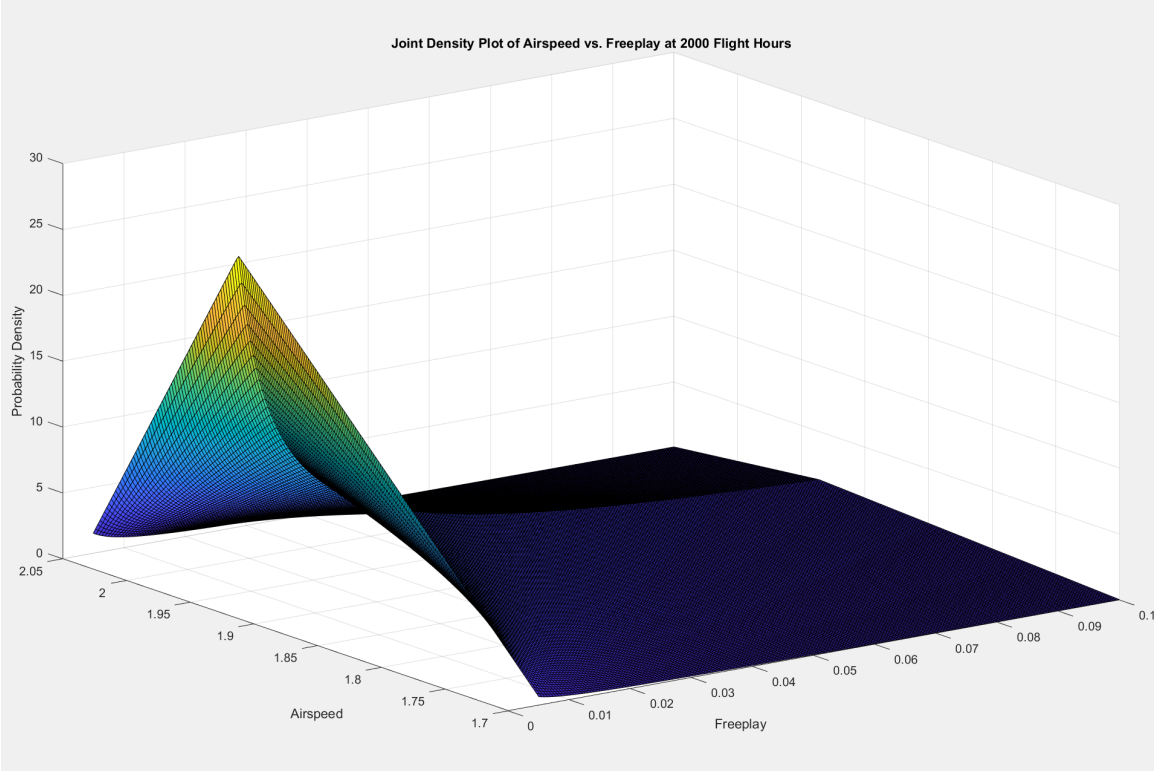

Figure 4.43: This graph shows how the two statistically independent variables map a PDF that maintains the characteristics of both variables. This PDF is plotted for 2000 flight hours.

Now, we can use the data from the cubic nonlinear systems to determine the probability of flutter. First, we must find a function that can accurate predict the nonlinear flutter velocity given an arbitrary free play amount. We used a best fit linear function to do this. Using the nonlinear flutter velocity data shown in the top view of the 3-D bifurcation diagram in Figure 4.37, we found that the linear function

$$V_{nf}(\delta) = 2.7829 - 1.5983\delta \tag{4.7}$$

was a highly accurate predictor of nonlinear flutter velocity, as shown in Figure 4.44. This nonlinear flutter predictor can be used to interpolate the nonlinear flutter velocity for any free play amount between $0° \leq \delta \leq 1°$. Beyond that, however, we cannot precisely use the linear function to predict the nonlinear flutter velocity because we do not have data to show if the nonlinear flutter velocity will remain linearly proportional to the free play amount. However, assuming that it does, we can use Equation

4.7 and use Y an input to obtain the value of the nonlinear flutter velocity associated with that value of free play. From there, we can find the probability of flutter as being

$$P(X > V_{nf}(Y(t)), Y(t) \leq y) = P(X > V_{nf}(Y(t)))P(Y(t) \leq y). \tag{4.8}$$

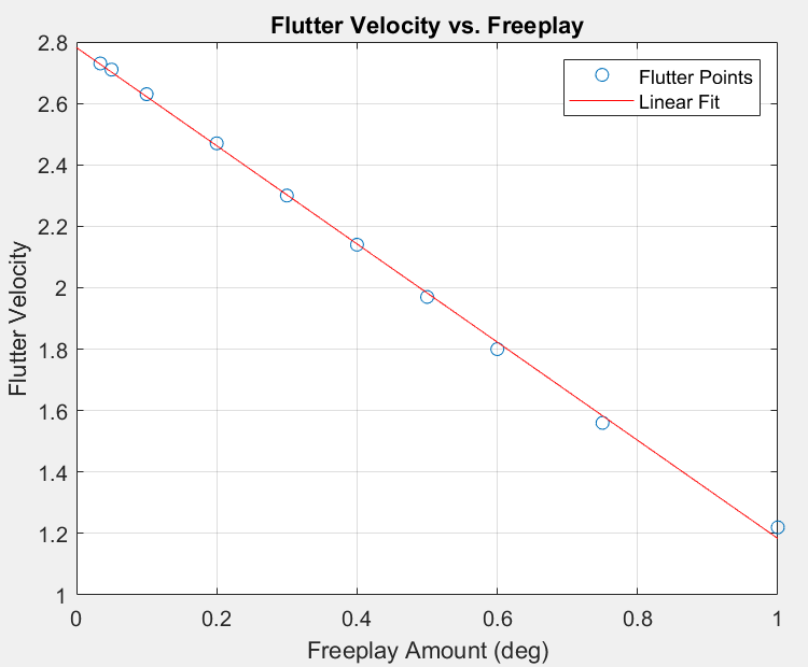

Figure 4.44: This graph shows the best fit linear model plotted with the nonlinear flutter velocity values that we obtained from Figure 4.37.

At this point, we have established an initial probabilistic framework for nonlinear aeroelastic systems. Following the same procedure that we outlined in this section, different nonlinear models and data can be used to create a more thorough and accurate quantitative model for determining probability of flutter. For future works, we plan to develop this probabilistic framework into a more sophisticated and comprehensive model that can take multiple inputs and produce multiple outputs.

Chapter 5

Conclusion and Future Works

We initiated this thesis with the motivation to examine how various models of free play and nonlinear stiffness affect an aeroelastic system's dynamical response. From our literature review, we found that there exist many different aeroelastic systems that can be formed by pairing numerous structural and aerodynamic models with various nonlinear stiffness models. These systems have been analyzed using a plethora of analytical and numerical tools, with the end goal of producing data to better understand how a nonlinear aeroelastic system with free play can potentially behave. The literature landscape was quite large, but contained many gaps and areas where more research was necessary in order to elucidate the many complexities in this field. One of the most immediate deficiency that we found was the lack of a probabilistic framework. The majority of the abundant and varied research that we found was deterministic. Thus, it became one of our goals to develop a probabilistic framework through our research to better understand how free play affects aeroelastic systems. Among other goals, we wished to contribute a new type of aeroelastic system that could be analyzed for studying free play. Finally, we wished to find connections between this problem and other existing and well-studied problems in the field of vibrations and nonlinear dynamics. Ultimately, this spurred our research and produced this thesis.

5.1 Accomplishments and Major Findings

Many new accomplishments were made in this thesis. First, we used a new combination of structural and aerodynamic models for studying free play. The unsteady aerodynamics theory of Peters et al. [104], using finite-state, induced flow theory, was paired with a two degree-of-freedom structural model. In this aeroelastic system, we added cubic and piecewise nonlinear stiffness. To our knowledge, this is a new nonlinear aeroelastic model that has not been studied in the field of free play. We were then able develop a state-space model that was compatible with systems that had both linear and nonlinear stiffness.

From the state-space models, we conducted time domain analyses by numerically integrating the aeroelastic system to produce time histories for a large range of velocities. Several different types of differential equation solvers were examined. In our numerical study, we looked into two main issues regarding the numerical stability of the solutions that we obtained. First, we looked into how manipulating error tolerances can lead to different sets of solutions, particularly for nonlinear systems that are highly sensitive near their flutter boundary. Our results confirmed that the choice of solver and their error tolerances were significant considerations that need to be understood and examined when dealing with nonlinear aeroelastic systems. Secondly, we looked at the possibility that the differential equations are numerically stiff, particularly for highly nonlinear systems. While inconclusive, our speculations were confirmed by our results that stiffness in the differential equations is another important consideration that must be understood and examined. From our research, we demonstrated the importance of correctly developing an accurate and efficient numerical methodology. This is an area that needs to be researched more in the field of free play. The trust in the data that is found across the literature relies greatly on the numerical framework that researchers have utilized.

Our next accomplishment in this research was being able to successfully iden-

tify complex nonlinear dynamics of the aeroelastic systems that we studied. While this is not new, we were able to find two very interesting connections between the field of free play and the field of nonlinear dynamics. First, we found that one of the highly nonlinear systems that we examined had many alternating regions of stability and regular solution flipping, as we described in Section 4.7.1. This type behavior is very similar to that of the Mathieu Equation, where the reason for changing stability regions is the time-dependent coefficients. More research is necessary to better understand this connection and how it can be used in the field of free play to explain certain unique phenomena. The second major connection we made was with the Duffing oscillator. In our cubic models, we found that some strongly nonlinear phenomena, such as chaos, only appeared for one cubic nonlinearity. Much like the Duffing oscillator, we believe that the aeroelastic systems will exhibit some unique nonlinear phenomena, such as chaos, only with a certain set of cubic nonlinearities. By better understanding the Duffing oscillator, we can potentially determine that set of cubic nonlinearities that produce such nonlinear behavior and aid with aeroelastic design.

We then examined a wide variety of cubic nonlinearities that were produced by curve fitting to piecewise models with varied amount of free play. Performing more time domain analyses allowed us to produce a novel 3-D plot containing the evolution of bifurcation curves with changing amount of free play. This 3-D plot was crucial in allowing us to gain strong qualitative understanding of various aeroelastic systems with cubic nonlinearities that differed from each other by small amounts. From this, we were also able to map a relationship between free play and nonlinear flutter velocity.

Next, we briefly examined the use of piecewise nonlinearities within our aeroelastic system. One of the unique features about our piecewise model was that we used the Heaviside function to represent this nonlinearity in one equation, allowing

us to easily incorporate it into our state-space model without altering it. We gained some interesting qualitative insight that we discussed in Section 4.8. One of the main limitations that prevented us from continuing further study of this nonlinearity was difficulties in the numerical integration of these systems. More research is necessary to better tackle this issue.

Finally, we developed a novel probabilistic framework that allowed us to quantify the probability of a nonlinear aeroelastic system encountering aeroelastic instability or flutter. We used a random variable that gave the probability of an aircraft flying at a some cruise velocity X and a second stochastic variable that gave the probability of a system having free play Y with t flight hours logged. Both of these variables were used to create a joint probability function that was tested using Monte Carlo simulation. Lastly, we used the data from the cubic nonlinear systems to develop relationships between free play amount and its nonlinear flutter velocity. This information was used to finally develop a scheme for quantifying the probability of flutter for some set of realizations. One of the major goals of this thesis was to have a framework in place that others can use and improve. We believe that we accomplished this goal with our probabilistic model. There is tremendous flexibility and room for broad applications.

5.2 Possible Improvements

The research that we performed in this thesis offers opportunities for improvement. Some of the numerical tools that we used for analyzing nonlinear dynamics can be further refined and improved. Two such cases are with producing better largest Lyapunov exponent (LLE) plots and with Pioncaré sections. For the LLE plots, we can improve the overall results by using smaller time steps for comparing and rescaling the infinitesimally separated systems. For the Pioncaré sections, we can use better

interpolation tools to better determine the exact times when a point should be plotted on the plots of the Pioncaré sections. Our current methodology is sufficient but refinements can always be made.

Another major area where improvements can be made is in the `MATLAB` code that we wrote. This would require expertise in programming, which we do not claim to possess. Our code is effective but its efficiency can always be further improved. This includes having a better numerical framework for the piecewise nonlinear systems.

Finally, our results are limited by the accuracy and speed of the hardware that was used. For this thesis, we produced all results using a personal laptop with an Intel(R) Core(TM) i5-8250U CPU operating at 1.60GHz. Access to better hardware can potentially allow more to be examined and allow for more refinements in our data and plots.

5.3 Future Works and Suggestions

We laid the groundwork for numerous avenues of further research. This project requires an understanding of many different fields from academic topics of engineering, computer science, mathematics, and physics to legal and industry topics such regulatory compliance, industry standards, and finance. In the future, we wish to further examine three main avenues of this research. First, we wish to further develop this research in the many areas of probability and statistical theories. This includes looking at potential stochastic forcing of the aeroelastic systems, extreme value theory, and sensitivity and perturbation analysis of initial conditions and constants.

The second avenue that we wish to further examine is in the field of aerodynamics. Studying a new unsteady aerodynamics theory has sparked our interest into this field. The study of free play has been historically apprehensive about exploring different aerodynamics theories for aeroelastic systems due to the high level of com-

plexities involved. However, we feel that this is a welcoming and exciting undertaking for the future.

The third and final avenue of research is in improving the structural models to be more realistic to real-life conditions. This means that not only must we consider nonlinear stiffness, but we must also consider structural stiffness in our models. This added level of complexity is the topic of many other engineering application that deal with structural dynamics.

One of our suggestions for researchers in this field is that there is a need for having access to real-life data from actual aircraft that may experience behavior associated with free play. The lack of available data makes it difficult for many to truly test the accuracy of their models and refine them as needed. While this data may be proprietary, our final recommendation is for more engineers in the industry to collaborate with academics who do research on this topic.

Bibliography

[1] David C. Asjes, Amit Diwadkar, Umesh Vaidya, and Atul Kelkar. "Development and System Analysis of a Two-Dimensional Rotational Freeplay Nonlinearity Model". In: *Journal of Aircraft* 53.3 (2016), pp. 860–865. ISSN: 0021-8669 1533-3868. DOI: 10.2514/1.C033275.

[2] Niles R. Hoffman and Irvin N. Spielberg. *Subsonic Flutter Tests of an unswept All-Movable Horizontal Tail*. Report WADC-TR-54-53. Wright Air Development Center, 1954.

[3] David C. Asjes. "Nonlinear analysis of a two- and three-degree-of-freedom aeroelastic system with rotational stiffness free-play". Thesis. 2015. URL: http://lib.dr.iastate.edu/etd/14317.

[4] Federal Aviation Administration. *Means of Compliance with Title 14 CFR Part 23 § 23.629 Flutter (AC 23.629-1B)*. Legal Rule or Regulation. 2004.

[5] Federal Aviation Administration. *Aeroelastic Stability Substantiation of Transport Category Airplanes (AC 25.629-1B)*. Legal Rule or Regulation. 2014.

[6] Robert Rosenbaum and A. A. Vollmecke. *Simplified flutter prevention criteria for personal type aircraft*. Airframe and Equipment Engineering Report 45. Federal Aviation Administration, 1955.

[7] P. C. Chen and D. H. Lee. "Flight-Loads Effects on Horizontal Tail Free-Play-Induced Limit Cycle Oscillation". In: *Journal of Aircraft* 45.2 (2008), pp. 478–485. ISSN: 0021-8669. DOI: 10.2514/1.29611.

[8] P. C. Chen, Erich Ritz, and Ned Lindsley. "Nonlinear Flutter Analysis for the Scaled F-35 with Horizontal-Tail Free Play". In: *Journal of Aircraft* 51.3 (2014), pp. 883–889. ISSN: 0021-8669 1533-3868. DOI: 10.2514/1.C032501.

[9] Theodore Theodorsen and I. E. Garrick. *Mechanism of flutter: A Theoretical and Experimental Investigation of the Flutter Problem*. Report 685. Langley Memorial Aeronautical Laboratory, 1940.

[10] Theodore Theodorsen and I. E. Garrick. *Flutter calculations in three degrees of freedom*. Report 741. Langley Memorial Aeronautical Laboratory, 1942.

[11] E. Breitbach. *Effects of Structural Non-Linearities on Aircraft Vibration and Flutter*. AGARD Report 665. Paper presented at the 45th Structures and Materials Panel Meeting, Voss, Norway. Advisory Group for Aerospace Research & Development, 1978.

[12] Donald S. Woolston, Harry L. Runyan, and Thomas A. Byrdsong. *Some effects of system nonlinearities in the problem of aircraft flutter*. Technical Note 3539. Langley Memorial Aeronautical Laboratory, 1955.

[13] S. F. Shen. "An Approximate Analysis of Nonlinear Flutter Problems". In: *Journal of the Aerospace Sciences* 26.1 (1959), pp. 25–32.

[14] Brian Danowsky, Peter M. Thompson, and Sunil Kukreja. "Nonlinear Analysis of Aeroservoelastic Models with Free Play Using Describing Functions". In: *Journal of Aircraft* 50.2 (2013), pp. 329–336. ISSN: 0021-8669 1533-3868. DOI: 10.2514/1.C031370.

[15] Abdessattar Abdelkefi and Muhammad R. Hajj. "Performance enhancement of wing-based piezoaeroelastic energy harvesting through freeplay nonlinearity". In: *Theoretical and Applied Mechanics Letters* 3.4 (2013). ISSN: 20950349. DOI: 10.1063/2.1304101.

[16] Andrea Mannarino. "Nonlinear Aeroservoelasticity: Reduced Order Modeling and Active Control". Doctoral dissertation. 2016. URL: http://hdl.handle.net/10589/117844.

[17] Himanshu Shukla and Mayuresh Patil. "Control of Limit Cycle Oscillation Amplitudes in Nonlinear Aeroelastic Systems using Nonlinear Normal Modes". In: *AIAA Atmospheric Flight Mechanics Conference*. 2016. DOI: 10.2514/6.2016-2004.

[18] Earl H. Dowell. *A Modern Course in Aeroelasticity*. Solid Mechanics and Its Applications. 2015. ISBN: 978-3-319-09452-6. DOI: 978-3-319-09453-3.

[19] Dewey H. Hodges and G. Alvin Pierce. *Introduction to Structural Dynamics and Aeroelasticity*. New York, NY: Cambridge University Press, 2002.

[20] P. Guruswamy and T. Y. Yang. "Aeroelastic time response analysis of thin airfoils by transonic code LTRAN2". In: *Computers and Fluids* 9.4 (1981), pp. 409–425.

[21] Nancy Hall, ed. *Stabilators*. NASA Glenn Research Center. Web Page. Apr. 2018. URL: https://www.grc.nasa.gov/www/k-12/airplane/stablator.html.

[22] Feixin Chen, Jike Liu, and Yanmao Chen. "Flutter analysis of an airfoil with nonlinear damping using equivalent linearization". In: *Chinese Journal of Aeronautics* 27.1 (2014), pp. 59–64. ISSN: 10009361. DOI: 10.1016/j.cja.2013.07.020.

[23] T. Dossogne, J. P. Noël, L. Masset, G. Kerschen, and B. Peeters. "Understanding and Modeling Nonlinear Behaviors in Aerospace Structures using Sine-Sweep Testing". In: *Journal AerospaceLab* 14 (2018), pp. 1–15. DOI: 10.12762/2018.AL14-12.

[24] Shun He, Zhichun Yang, and Yingsong Gu. "Limit cycle oscillation behavior of transonic control surface buzz considering free-play nonlinearity". In: *Journal of Fluids and Structures* 61 (2016), pp. 431–449. ISSN: 08899746. DOI: 10.1016/j.jfluidstructs.2015.11.014.

[25] Peng Li, Yiren Yang, and Li Lu. "Nonlinear flutter behavior of a plate with motion constraints in subsonic flow". In: *Meccanica* 49.12 (2014), pp. 2797–2815. ISSN: 0025-6455 1572-9648. DOI: 10.1007/s11012-014-0041-8.

[26] Q. X. Liu, X. S. He, J. K. Liu, Y. M. Chen, and L. C. Huang. "Solving Fractional Dynamical System with Freeplay by Combining Memory-Free Approach and Precise Integration Method". In: *Mathematical Problems in Engineering* 2016 (2016), pp. 1–7. ISSN: 1024-123X 1563-5147. DOI: 10.1155/2016/9430528.

[27] D. Poirel and S. J. Price. "Response probability structure of a structurally nonlinear fluttering airfoil in turbulent flow". In: *Probabilistic Engineering Mechanics* 18.2 (2003), pp. 185–202. ISSN: 02668920. DOI: 10.1016/s0266-8920(03)00013-4.

[28] Hu-lun Guo and Yu-shu Chen. "Dynamic analysis of two-degree-of-freedom airfoil with freeplay and cubic nonlinearities in supersonic flow". In: *Applied Mathematics and Mechanics* 33.1 (2012), pp. 1–14. ISSN: 0253-4827 1573-2754. DOI: 10.1007/s10483-012-1529-x.

[29] B. H. K. Lee, S. J. Price, and Y. S. Wong. "Nonlinear aeroelastic analysis of airfoils: bifurcations and chaos". In: *Progress in Aerospace Sciences* 35 (1999), pp. 205–334.

[30] K. W. Chung, C. L. Chan, and B. H. K. Lee. "Bifurcation analysis of a two-degree-of-freedom aeroelastic system with freeplay structural nonlinearity by a perturbation-incremental method". In: *Journal of Sound and Vibration* 299.3 (2007), pp. 520–539. ISSN: 0022460X. DOI: 10.1016/j.jsv.2006.06.059.

[31] Zhao De-Min and Zhang Qi-Chang. "Bifurcation and chaos analysis for aeroelastic airfoil with freeplay structural nonlinearity in pitch". In: *Chinese Physics B* 19.3 (2010). ISSN: 1674-1056. DOI: 10.1088/1674-1056/19/3/030518.

[32] Christopher W. Emory and Mayuresh J. Patil. "Predicting Limit Cycle Oscillation in an Aeroelastic System Using Nonlinear Normal Modes". In: *Journal of Aircraft* 50.1 (2013), pp. 73–81. ISSN: 0021-8669 1533-3868. DOI: 10.2514/1.C031668.

[33] Li Yi and Yang Zhichun. "Uncertainty Quantification in Flutter Analysis for an Airfoil with Preloaded Freeplay". In: *Journal of Aircraft* 47.4 (2010), pp. 1454–1457. ISSN: 0021-8669 1533-3868. DOI: 10.2514/1.C031011.

[34] Honghua Dai, Xiaokui Yue, Dan Xie, and Satya N. Atluri. "Chaos and chaotic transients in an aeroelastic system". In: *Journal of Sound and Vibration* 333.26 (2014), pp. 7267–7285. ISSN: 0022460X. DOI: 10.1016/j.jsv.2014.08.034.

[35] Honghua Dai, Xiaokui Yue, Jianping Yuan, Dan Xie, and S. N. Atluri. "A comparison of classical Runge-Kutta and Henon's methods for capturing chaos and chaotic transients in an aeroelastic system with freeplay nonlinearity". In: *Nonlinear Dynamics* 81.1-2 (2015), pp. 169–188. ISSN: 0924-090X 1573-269X. DOI: 10.1007/s11071-015-1980-x.

[36] Mark D. Connor, Lawrence N. Virgin, and Earl H. Dowell. "Accurate Numerical Integration of State-Space Models for Aeroelastic Systems with Free Play". In: *AIAA Journal* 34.10 (1996), pp. 2202–2205.

[37] Saeid Sazesh and Shahrokh Shams. "Nonlinear aeroelastic analysis of an airfoil with control surface free-play using stochastic approach". In: *Journal of Fluids and Structures* 72 (2017), pp. 114–126. ISSN: 08899746. DOI: 10.1016/j.jfluidstructs.2017.05.005.

[38] Daniel A. Pereira, Rui M. G. Vasconcellos, Muhammad R. Hajj, and Flávio D. Marques. "Effects of combined hardening and free-play nonlinearities on the response of a typical aeroelastic section". In: *Aerospace Science and Technology* 50 (2016), pp. 44–54. ISSN: 12709638. DOI: 10.1016/j.ast.2015.12.022.

[39] D. Dessi and F. Mastroddi. "Limit-cycle stability reversal via singular perturbation and wing-flap flutter". In: *Journal of Fluids and Structures* 19.6 (2004), pp. 765–783. ISSN: 08899746. DOI: 10.1016/j.jfluidstructs.2004.04.010.

[40] Grigorios Dimitriadis. *Introduction to Nonlinear Aeroelasticity*. John Wiley & Sons Ltd, 2017. ISBN: 9781118613474. DOI: 10.1002/9781118756478.

[41] James T. Gordon, Edward E. Meyer, and Robert L. Minogue. "Nonlinear Stability Analysis of Control Surface Flutter with Freeplay Effects". In: *Journal of Aircraft* 45.6 (2008), pp. 1904–1916. ISSN: 0021-8669 1533-3868. DOI: 10.2514/1.31901.

[42] Daochun Li, Shijun Guo, and Jinwu Xiang. "Aeroelastic dynamic response and control of an airfoil section with control surface nonlinearities". In: *Journal of Sound and Vibration* 329.22 (2010), pp. 4756–4771. ISSN: 0022460X. DOI: 10.1016/j.jsv.2010.06.006.

[43] Edouard Verstraelen, Grigorios Dimitriadis, Gustavo Dal Ben Rossetto, and Earl H. Dowell. "Two-domain and three-domain limit cycles in a typical aeroelastic system with freeplay in pitch". In: *Journal of Fluids and Structures* 69 (2017), pp. 89–107. ISSN: 08899746. DOI: 10.1016/j.jfluidstructs.2016.11.019.

[44] Y. M. Chen and J. K. Liu. "Nonlinear aeroelastic analysis of an airfoil-store system with a freeplay by precise integration method". In: *Journal of Fluids and Structures* 46 (2014), pp. 149–164. ISSN: 08899746. DOI: 10.1016/j.jfluidstructs.2014.01.003.

[45] Denis B. Kholodar. "Aircraft Control Surface and Store Freeplay-Induced Vibrations in Aeroelastic Stability Envelope". In: *Journal of Aircraft* 53.5 (2016), pp. 1538–1548. ISSN: 0021-8669 1533-3868. DOI: 10.2514/1.C033772.

[46] Madhusudan A. Padmanabhan, Earl H. Dowell, Jeffrey P. Thomas, and Crystal L. Pasiliao. "Store-Induced Limit-Cycle Oscillations Due to Nonlinear Wing-Store Attachment". In: *Journal of Aircraft* 53.3 (2016), pp. 778–789. ISSN: 0021-8669 1533-3868. DOI: 10.2514/1.C033577.

[47] Deman Tang and Earl H. Dowell. "Experimental and theoretical study of gust response for a wing–store model with freeplay". In: *Journal of Sound and Vibration* 295.3-5 (2006), pp. 659–684. ISSN: 0022460X. DOI: 10.1016/j.jsv.2006.01.024.

[48] Waleed J. Al-Mashhadani, Earl H. Dowell, Hatem R. Wasmi, and Ali A. Al-Asadi. "Aeroelastic response and limit cycle oscillations for wing-flap-tab section with freeplay in tab". In: *Journal of Fluids and Structures* 68 (2017), pp. 403–422. ISSN: 08899746. DOI: 10.1016/j.jfluidstructs.2016.11.017.

[49] Lillian Gipson, ed. *Parts of an Airplane, Grades 5-8*. NASA Aeronautics Research Mission Directorate. Online Multimedia. Museum in a Box. Aug. 2017. URL: https://www.nasa.gov/sites/default/files/atoms/files/parts_of_an_airplane_5-8.pdf.

[50] S. H. Kim and In Lee. "Aeroelastic analysis of a flexible airfoil with a freeplay non-linearity". In: *Journal of Sound and Vibration* 193.4 (1996), pp. 823–846.

[51] Dong Hefeng, Wang Chenxi, Li Shaobin, and Song Xi Zhen. "Numerical Research on Segmented Flexible Airfoils Considering Fluid-structure Interaction". In: *Procedia Engineering* 99 (2015), pp. 57–66. ISSN: 18777058. DOI: 10.1016/j.proeng.2014.12.508.

[52] Rauno Cavallaro, Luciano Demasi, Rocco Bombardieri, and Andrea Iannelli. "PrandtlPlane Joined Wing: Body Freedom Flutter, Limit Cycle Oscillation and Freeplay Studies". In: *56th AIAA/ASCE/AHS/ASC Structures, Structural Dynamics, and Materials Conference*. 2015. DOI: 10.2514/6.2015-1184.

[53] Rui Huang, Haiyan Hu, and Yonghui Zhao. "Nonlinear aeroservoelastic analysis of a controlled multiple-actuated-wing model with free-play". In: *Journal of Fluids and Structures* 42 (2013), pp. 245–269. ISSN: 08899746. DOI: 10.1016/j.jfluidstructs.2013.06.007.

[54] Kan Ni, Patrick Hu, Hongwu Zhao, and Earl Dowell. "Flutter and LCO of an All-movable Horizontal Tail with Freeplay". In: *53rd AIAA/ASME/ASCE/AHS/ASC Structures, Structural Dynamics and Materials Conference¡BR¿20th AIAA/ASME/AHS Adaptive Structures Conference, 14th AIAA*. 2012. DOI: 10.2514/6.2012-1979.

[55] Robert Carrese, Nishit Joseph, Pier Marzocca, and Oleg Levinski. "Aeroelastic Response of the AGARD 445.6 Wing with Freeplay Nonlinearity". In: *58th AIAA/ASCE/AHS/ASC Structures, Structural Dynamics, and Materials Conference*. 2017. DOI: 10.2514/6.2017-0416.

[56] Bret Stanford and Philip Beran. "Minimum-mass panels under probabilistic aeroelastic flutter constraints". In: *Finite Elements in Analysis and Design* 70-71 (2013), pp. 15–26. ISSN: 0168874X. DOI: 10.1016/j.finel.2013.03.001.

[57] Jason C. Kiiskila, Matthew R. Duncan, and Dale M. Pitt. "Investigation of the Dynamic Characterization of Aircraft Control Surface Free Play". In: *24th International Modal Analysis Conference*. 2006, pp. 22–30.

[58] D. Li, S. Guo, and J. Xiang. "Study of the conditions that cause chaotic motion in a two-dimensional airfoil with structural nonlinearities in subsonic flow". In: *Journal of Fluids and Structures* 33 (2012), pp. 109–126. ISSN: 08899746. DOI: 10.1016/j.jfluidstructs.2012.04.010.

[59] R. Vasconcellos, A. Abdelkefi, F. D. Marques, and M. R. Hajj. "Representation and analysis of control surface freeplay nonlinearity". In: *Journal of Fluids and Structures* 31 (2012), pp. 79–91. ISSN: 08899746. DOI: 10.1016/j.jfluidstructs.2012.02.003.

[60] Deman Tang and Earl H. Dowell. "Aeroelastic Response Induced by Free Play, Part 1: Theory". In: *AIAA Journal* 49.11 (2011), pp. 2532–2542. ISSN: 0001-1452 1533-385X. DOI: 10.2514/1.J051055.

[61] Deman Tang and Earl H. Dowell. "Aeroelastic Response Induced by Free Play, Part 2: Theoretical/Experimental Correlation Analysis". In: *AIAA Journal* 49.11 (2011), pp. 2543–2554. ISSN: 0001-1452 1533-385X. DOI: 10.2514/1.J051056.

[62] R. Vasconcellos, A. Abdelkefi, M. R. Hajj, and F. D. Marques. "Grazing bifurcation in aeroelastic systems with freeplay nonlinearity". In: *Communications in Nonlinear Science and Numerical Simulation* 19.5 (2014), pp. 1611–1625. ISSN: 10075704. DOI: 10.1016/j.cnsns.2013.09.022.

[63] Rui M. G. Vasconcellos, Abdessattar Abdelkefi, Muhammad R. Hajj, Daniel P. Almeida, and Flávio D. Marques. "Airfoil control surface discontinuous nonlinearity experimental assessment and numerical model validation". In: *Journal of Vibration and Control* 22.6 (2016), pp. 1633–1644. ISSN: 1077-5463 1741-2986. DOI: 10.1177/1077546314543911.

[64] K. W. Chung, Y. B. He, and B. H. K. Lee. "Bifurcation analysis of a two-degree-of-freedom aeroelastic system with hysteresis structural nonlinearity by a perturbation-incremental method". In: *Journal of Sound and Vibration* 320.1-2 (2009), pp. 163–183. ISSN: 0022460X. DOI: 10.1016/j.jsv.2008.07.019.

[65] Theodore Theodorsen. *General Theory of Aerodynamic Instability and the Mechanism of Flutter*. Report 496. National Advisory Committee for Aeronautics, 1934.

[66] Ulgen Gulcat. *Fundamentals of Modern Unsteady Aerodynamics*. 2016. ISBN: 978-981-10-0016-4. DOI: 10.1007/978-981-10-0018-8. URL: https://www.springer.com/gp/book/9789811000164.

[67] William Paul Walker. "Optimization of Harmonically Deforming Thin Airfoils and Membrane Wings for Optimum Thurst and Efficiency". Thesis. 2012.

[68] Y. C. Fung. *An Introduction to the Theory of Aeroelasticity*. New York, NY: Dover Publications, Inc., 1969. ISBN: 0486469360.

[69] B. H. K. Lee, L. Gong, and Y. S. Wong. "Analysis and Computation of Nonlinear Dynamic Response of a Two-Degree-of-Freedom System and Its Application in Aeroelasticity". In: *Journal of Fluids and Structures* 11.3 (1997), pp. 225–246. ISSN: 08899746. DOI: 10.1006/jfls.1996.0075.

[70] Jan Wright and Jonathan Cooper. *Introduction to Aircraft Aeroelasticity and Loads*. 2007. ISBN: 978-1-56347-935-9. DOI: 10.2514/4.479359.

[71] Oddvar O. Bendiksen. "Review of unsteady transonic aerodynamics: Theory and applications". In: *Progress in Aerospace Sciences* 47.2 (2011), pp. 135–167. ISSN: 03760421. DOI: 10.1016/j.paerosci.2010.07.001.

[72] N. C. Lambourne. *Control-Surface Buzz*. Reports and Memoranda 3364. Ministry of Aviation, 1964.

[73] F. Eastep, G. Andersen, and P. Beran. "Control surface effectiveness in the transonic regime". In: *7th AIAA/USAF/NASA/ISSMO Symposium on Multidisciplinary Analysis and Optimization*. 1998. DOI: 10.2514/6.1998-4932.

[74] A.C.L.M. van Rooij. "Aeroelastic Limit-Cycle Oscillations resulting from Aerodynamic Non-Linearities". Doctoral dissertation. 2017. DOI: 10.4233/uuid:cc2f32f8-6c6f-4675-a47c-37b70ed4e30c.

[75] Laith K. Abbas, Q. Chen, K. O'Donnell, D. Valentine, and P. Marzocca. "Numerical studies of a non-linear aeroelastic system with plunging and pitching freeplays in supersonic/hypersonic regimes". In: *Aerospace Science and Technology* 11.5 (2007), pp. 405–418. ISSN: 12709638. DOI: 10.1016/j.ast.2007.02.007.

[76] Kenneth A. Kousen and Oddvar O. Bendiksen. "Limit Cycle Phenomena in Computational Transonic Aeroelasticity". In: *Journal of Aircraft* 31.6 (1994), pp. 1257–1263.

[77] Denis B. Kholodar, Earl H. Dowell, Jeffrey P. Thomas, and Kenneth C. Hall. "Limit Cycle Oscillation of a Typical Airfoil in Transonic Flow". In: *Journal of Aircraft* 41.5 (2004), pp. 1067–1072. ISSN: 0021-8669 1533-3868. DOI: 10.2514/1.618.

[78] J. Y. Kim, K. S. Kim, I. Lee, and Y. K. Park. "Transonic Aeroelastic Analysis of All-Movable Wing with Free Play and Viscous Effects". In: *Journal of Aircraft* 45.5 (2008), pp. 1820–1824. ISSN: 0021-8669 1533-3868. DOI: 10.2514/1.37435.

[79] Young-Keun Park, Jae-Han Yoo, and In Lee. "Nonlinear Aeroelastic Analysis of Control With Freeplay in Transonic Region". In: *AIAA Journal* 45.5 (2007), pp. 1142–1145. ISSN: 0001-1452 1533-385X. DOI: 10.2514/1.14068.

[80] Steven H. Strogatz. *Nonlinear Dynamics and Chaos*. Reading, MA: Addison-Wesley Publishing Company, 1994. DOI: 10.1063/1.4823332.

[81] Sebastiano Fichera and Sergio Ricci. "High order harmonic balance applied to an aeroelastic T-tail model with a control surface freeplay". In: *54th AIAA/ASME/ASCE/AHS/ASC Structures, Structural Dynamics, and Materials Conference*. 2013. DOI: 10.2514/6.2013-1704.

[82] Liping Liu and Earl Dowell. "Harmonic Balance Approach for an Airfoil with a Freeplay Control Surface". In: *AIAA Journal* 43.4 (2005), pp. 802–815.

[83] Raouf A. Ibrahim and Ronald F. Gibson. *Nonlinear Stochastic Flutter of a Cantilever Wing with Joint Relaxation and Random Loading*. Report. Wayne State University, 2008.

[84] Cui Peng and Jinglong Han. "Numerical investigation of the effects of structural geometric and material nonlinearities on limit-cycle oscillation of a cropped delta wing". In: *Journal of Fluids and Structures* 27.4 (2011), pp. 611–622. ISSN: 08899746. DOI: 10.1016/j.jfluidstructs.2011.03.015.

[85] Dai Yuting and Yang Chao. "Methods and advances in the study of aeroelasticity with uncertainties". In: *Chinese Journal of Aeronautics* 27.3 (2014), pp. 461–474. ISSN: 10009361. DOI: 10.1016/j.cja.2014.04.016.

[86] Dale M. Pitt, Darin P. Haudrich, Michael J. Thomas, and Kenneth E. Griffin. "Probabilistic Aeroelastic Analysis and Its Implications on Flutter Margin Requirements". In: *49th AIAA/ASME/ASCE/AHS/ASC Structures, Structural Dynamics, and Materials Conference*. 2008. DOI: 10.2514/6.2008-2198.

[87] M. T. Thanusha and Sunetra Sarkar. "Uncertainty Quantification of Subcritical Nonlinear Aeroelastic System Using Integrated Interpolation Method and Polynomial Chaos Expansion". In: *Procedia Engineering* 144 (2016), pp. 982–989. ISSN: 18777058. DOI: 10.1016/j.proeng.2016.05.128.

[88] Marc P. Mignolet and Ping C. Chen. "Aeroelastic Analyses with Uncertainty in Structural Properties". In: *Computational Uncertainty in Military Vehicle Design, Meeting Proceedings RTO-MP-AVT-147*. Neuilly-sur-Seine, France, 2007. Chap. Paper 2, pp. 1–18.

[89] Mahdi Fatehi, Majid Moghaddam, and Mohammad Rahim. "Robust flutter analysis and control of a wing". In: *Aircraft Engineering and Aerospace Technology* 84.6 (2012), pp. 423–438. DOI: 10.1108/00022661211272981.

[90] Xing-zhi Xu, Ya-kui Gao, and Wei-guo Zhang. "Iterative Learning Control of a Nonlinear Aeroelastic System despite Gust Load". In: *International Journal of Aerospace Engineering* 2015 (2015), pp. 1–13. ISSN: 1687-5966 1687-5974. DOI: 10.1155/2015/237804.

[91] Calogero Orlando and Andrea Alaimo. "A robust active control system for shimmy damping in the presence of free play and uncertainties". In: *Mechanical Systems and Signal Processing* 84 (2017), pp. 551–569. ISSN: 08883270. DOI: 10.1016/j.ymssp.2016.07.038.

[92] Demin Zhao, Qichang Zhang, and Ying Tan. "Random flutter of a 2-DOF nonlinear airfoil in pitch and plunge with freeplay in pitch". In: *Nonlinear Dynamics* 58.4 (2009), pp. 643–654. ISSN: 0924-090X 1573-269X. DOI: 10.1007/s11071-009-9507-y.

[93] Arion Pons and Stefanie Gutschmidt. "Multiparameter Spectral Analysis for Aeroelastic Instability Problems". In: *Journal of Applied Mechanics* 85.6 (2018). ISSN: 0021-8936. DOI: 10.1115/1.4039671.

[94] Saied Irani, Saeid Sazesh, and Vahid Reza Molazadeh. "Flutter analysis of a nonlinear airfoil using stochastic approach". In: *Nonlinear Dynamics* 84.3 (2016), pp. 1735–1746. ISSN: 0924-090X 1573-269X. DOI: 10.1007/s11071-016-2601-z.

[95] Todd O'Neil. "Nonlinear aeroelastic response - Analyses and experiments". In: *34th Aerospace Sciences Meeting and Exhibit*. 1996.

[96] C. C. Marsden and S. J. Price. "The aeroelastic response of a wing section with a structural freeplay nonlinearity: An experimental investigation". In: *Journal of Fluids and Structures* 21.3 (2005), pp. 257–276. ISSN: 08899746. DOI: 10.1016/j.jfluidstructs.2005.05.015.

[97] Mark D. Connor, Deman Tang, Earl Dowell, and Lawrence N. Virgin. "Nonlinear behavior of a typical airfoil section with control surface freeplay: A numerical and experimental study". In: *Journal of Fluids and Structures* 11 (1997), pp. 89–109.

[98] A. Abdelkefi, R. Vasconcellos, F. D. Marques, and M. R. Hajj. "Modeling and identification of freeplay nonlinearity". In: *Journal of Sound and Vibration* 331.8 (2012), pp. 1898–1907. ISSN: 0022460X. DOI: 10.1016/j.jsv.2011.12.021.

[99] Deman Tang and Earl H. Dowell. "Experimental Aeroelastic Response for a Freeplay Control Surface in Buffeting Flow". In: *AIAA Journal* 51.12 (2013), pp. 2852–2861. ISSN: 0001-1452 1533-385X. DOI: 10.2514/1.J052495.

[100] Hiroyuki Morino and Shigeru Obayashi. "Nonlinear Aeroelastic Analysis of Control Surface with Freeplay Using Computational-Fluid-Dynamics-Based Reduced-Order Models". In: *Journal of Aircraft* 52.2 (2015), pp. 569–583. ISSN: 0021-8669 1533-3868. DOI: 10.2514/1.C032775.

[101] J. L. Casado Corpas and J. López Díez. "Flutter margin with non-linearities: Real-time prediction of flutter onset speed". In: *Proceedings of the Institution of Mechanical Engineers, Part G: Journal of Aerospace Engineering* 222.6 (2008), pp. 921–929. ISSN: 0954-4100. DOI: 10.1243/09544100jaero251.

[102] Young-Keun Park, Jae-Han Yoo, In Lee, and Dae-Yeal Lee. "Effects of Angle-of-Attack on the Aeroelastic Characteristics of a Wing with Freeplay". In: *Journal of Spacecraft and Rockets* 43.6 (2006), pp. 1419–1422. ISSN: 0022-4650 1533-6794. DOI: 10.2514/1.21368.

[103] David A. Peters. "Two-dimensional incompressible unsteady airfoil theory—An overview". In: *Journal of Fluids and Structures* 24.3 (2008), pp. 295–312. ISSN: 08899746. DOI: 10.1016/j.jfluidstructs.2007.09.001.

[104] David A. Peters, Swaminathan Karunamoorthy, and Wen-Ming Cao. "Finite state induced flow models. I - Two-dimensional thin airfoil". In: *Journal of Aircraft* 32.2 (1995), pp. 313–322. ISSN: 0021-8669 1533-3868. DOI: 10.2514/3.46718.

[105] William Sears. "Some Aspects of Non-Stationary Airfoil Theory and Its Practical Application". In: *Journal of the Aeronautical Sciences* 8.3 (1941), pp. 104–108.

[106] Haym Benaroya, Mark Nagurka, and Seon Han. *Mechanical Vibration: Analysis, Uncertainties, and Control*. 4th Edition. Mechanical Engineering. Boca Raton, FL: CRC Press, 2017. ISBN: 9781498752947.

[107] M. Greenberg. *Advanced Engineering Mathematics*. 2nd ed. Upper Saddle River, NJ: Prentice Hall, 1998. ISBN: 978-0133214314.

[108] L. F. Shampine and M. W. Reichelt. "The MATLAB ODE Suite". In: *SIAM Journal on Scientific Computing* 18 (1997), pp. 1–22.

[109] S. Sekar and M. Nalini. "Numerical Solution of the Linear and Nonlinear Stiff Problems Using Adomian Decomposition Method". In: *IOSR Journal of Mathematics* 11 (5 2015), pp. 14–20.

[110] G. D. Byrne and Skip Thompson. "Error Control Matters". In: 2013.

[111] Grigorios Dimitriadis. "Complete bifurcation behaviour of aeroelastic systems with freeplay". In: *52nd AIAA/ASME/ASCE/AHS/ASC Structures, Structural Dynamics and Materials Conference*. 2011. DOI: 10.2514/6.2011-2142.

[112] L.F. Shampine, I. Gladwell, and S. Thompson. *Solving ODEs with MATLAB*. Cambridge, New York: Cambridge University Press, 2003. ISBN: 978-0-511-07707-4.

[113] Federal Aviation Administration. *Factor of safety (AC 25.303)*. Legal Rule or Regulation. 2002.

[114] Francis Moon. *Chaos and Fractal Dyanmics*. New York, NY: John Wiley and Sons, Inc., 1992. ISBN: 0-471-54571-6.

[115] J. C. Sprott. *Chaos and Time-Series Analysis*. Oxford, UK: Oxford University Press, 2003. ISBN: 978-0-19-850840-3.

[116] D. W. Jordan and P. Smith. *Nonlinear Ordinary Differential Equations*. 4th Edition. New York: Oxford University Press, 2007. ISBN: 978-0-19-920824-1.

[117] Haym Benaroya, Seon Han, and Mark Nagurka. *Probabilistic Models for Dynamical Systems*. 2nd Edition. CRC Press, 2013. ISBN: 9781439849897.

[118] Federal Aviation Administration. *Design Dive Speed (AC 25.335-lA)*. Legal Rule or Regulation. 2002.

[119] Eric W. Weisstein. *Triangular Distribution*. From MathWorld–A Wolfram Web Resource. URL: http://mathworld.wolfram.com/TriangularDistribution.html. (accessed: 03.11.2020).

[120] *High Altitude Flight Operations*. URL: https://www.skybrary.aero/index.php/High_Altitude_Flight_Operations#Variation_in_Cruise_Speed. (accessed: 03.11.2020).

[121] Eric W. Weisstein. *Gamma Distribution*. From MathWorld–A Wolfram Web Resource. URL: http://mathworld.wolfram.com/GammaDistribution.html. (accessed: 03.11.2020).

[122] S. A. Safi and R. D. Archor. "Interactions between wear processes and limit cycle oscillations of a control surface with free-play non-linearity". In: *Proceedings of the Institute of Mechanical Engineers, Part G: Journal of Aerospace Engineering* 216.3 (2002), pp. 143–153. DOI: 10.1243/095441002760553685.

[123] Federal Aviation Administration. *Airworthiness Directives; Boeing Model 737 Airplanes*. Legal Rule or Regulation. 2006.